UNIVERSITY COLLEGE LONDON

Faculty of Mathematics and Physical Sciences

Department of Physics and Astronomy

DEVELOPMENT OF ASTROCHEMICAL MODELS BASED ON LABORATORY DATA

Thesis submitted for the Degree of Doctor of Philosophy
of the University of London

by
Angela Occhiogrosso

Supervisors:	Examiners:
Prof. Serena Viti	Prof. Martin R. S. McCoustra
Prof. Wendy A. Brown	Prof. Tom J. Millar

November 14, 2013

To someone special, Paul Apaullo (p.p.) Woods

I, Angela Occhiogrosso, confirm that the work presented in this thesis is my own. Where information has been derived from other sources, I confirm that this has been indicated in the thesis.

Abstract

The more we discover about the molecular composition of the interstellar medium (ISM) the more we realise how difficult it is to reproduce the mechanisms behind this complex chemistry.

To date, over 175 different molecular species have been detected in the ISM. Many of them are formed in the gas phase, but there is a growing number of species that form more efficiently on grain surfaces during the collapse of star-forming cores.

An important issue in mimicking the interstellar medium chemistry is that there are few observational clues about the synthesis of complex organic molecules on grains; experimental work coupled with chemical modelling is therefore essential in order to understand the chemical complexity of the ISM.

UCL_CHEM is a computer model that takes into account the gas-grain interactions occurring during this collapse, with the aim of reproducing the observed abundances of molecules in various astronomical environments.

The work in this thesis deals with the coupling of UCL_CHEM with the most recent experimental results on the formation in the solid state of various complex organic molecules including methyl formate (see Chapter 3) and ethylene oxide and acetaldehyde (whose chemistry is extensively discussed in Chapters 4 and 5), all which have been the subject of recent astronomical interest.

Moreover, important revisions of some reactions occurring in the gas phase have also been made. Despite everything seeming straightforward concerning the interstellar chemistry in the gas phase, there is still a great deal to unearth in this regard. Oxygen, for instance, is an important player in the ISM because it is the most abundant element after hydrogen and helium. Although its chemistry seems well understood, we propose a

revised scheme for its reactions with small unsaturated hydrocarbons (see Chapter 6) and we show how the new reaction network affects the molecular abundances of these linear carbon chains. In Chapter 6, we also emphasise the relevance in treating structural isomers as two different species when they show peculiar chemical behaviours.

Another key issue in reproducing the interstellar molecular variety concerns the freeze-out of species onto dust grain surfaces. In particular, we know little about the constituents of the icy mantles. In Chapter 7, we analyse the case of sulfur-bearing species because the most dominant ice component is still debated.

Acknowledgements

Dear reader,

a couple of warnings before continuing with your reading:

1. This section will certainly contain mistakes due to my poor knowledge of the English Grammar.
2. This section might be the longest of this thesis.

Said that, let me start by saying *Thanks* to Serena, my supervisor, for giving me the opportunity to obtain this PhD (well, hopefully I will). During the past three years I have been learning how to be independent and confident in my work. Her passion and expertise in the field of Astronomy were really contagious to such an extent that now I am a perfect *astrochemical mixture*!

I want also to acknowledge all my collaborators, that improved my work with their suggestions and stimulated new ideas.

I will certainly miss my *LASSIE* friends (N.B. I am not talking about *dogs*); we had such a good time together, we supported to each other during the most boring after-dinner training, we shared various experiences and emotions (Gosh, just crossed to my mind my first talk), and we visited beautiful places (with the exception of Cuijk, though)... so, please guys, do not forget your *guide*!!!!

Finally, a big thank to UCL, and by *UCL* I mean all the people I met there and those I had to say *Goodbye*. The most multicultural and fascinating environment I have ever lived in. My offices have been my houses so I am feeling particularly close to my *office-mates* of G18 and OB22. OB22 looks like a prison, where I have been caught during my last year, but people, who I shared the office with, created a very friendly and enjoyable atmosphere (yes, I am including Nick)!

Moving to my private life, first of all, I am very greatful to Nadia, my encouragment and one of my best friends! Without her my adventure here at UCL would have never been possible. She pushed me in applying to my current position and she wrote such nice references for me. She helped me in several professional and private situations and she had amazing ideas about a scientific project that is now published. We also had so much fun together: I will never forget our first/last Conference together in Tallin!

Thanks a lot to Silvia and Luke for supporting me and organising some *fun-time* in order to distract my brain during my writing-up. Oh, Silvia, your hugs made me feel so good!

Thanks to Emma, the best listener and adviser: I really missed our conversation after you had moved from G18!

Let me thank teacher Hannah, for her lessons in posh English and also all the other people within my group: Helen, Rebeca, Thomas, Antonios, George, Farah.

A special thought to Fabrizio, my Italian friend in London, I appreciated your patience during our exausting trips!

Even though at the moment they are kilometers far away from here, I want to thank Cris and Georgie. They meant a lot to me... I started to enjoy my life in London after I moved with them. They gave me the *attentions* and the help I really needed at that time. My best londoner friends, for sure!

Infine grazie di infinito cuore ai miei genitori, per tutti i chilometri ed i sacrifici fatti per starmi dietro, a mia sorella ed Angelo che, nonostante i nostri diversi stili di vita e punti di vista, non mi hanno mai negato il loro affetto e supporto; a loro che mi hanno regalato la gioia piu' grande di diventare zia e che presto la duplicheranno!

Ai miei fratelli adottivi, Gicomo e Francesca ed al mio caro amico Lorenzo... I loro nomi compaiono nei ringraziamenti di tutte le mie tesi e cio' e' gia' sufficiente a spiegare quanto io li abbia sentiti e li senta a tutt'ora cosi' vicini e parte fondamentale della mia vita.

In questa lista di amici *di vecchia data*, non puo' manacare Evelyn, con la quale ho condiviso parte del mio cammino universitario. A lei che, nel silenzio, mi ha seguita passo dopo passo e non si e' fatta mai sfuggire gli eventi piu' decisivi del mio percorso di vita.

Finally, thanks to someone who makes me feel happy and relaxed; who has been an helpful colleague (carefully correcting my thesis and giving me good suggestions to improve my work) as well as my confidant during the worse time of my life; who shares troubles and fun-time with me... thanks to someone special, Paul.

Considerate la vostra semenza:
fatti non foste a viver come bruti,
ma per seguir virtute e canoscenza.

Dante, Divina Commedia, Inferno, XXVI, 118-120

Contents

List of Figures

List of Tables

Chapter 1

Introduction

The chemistry of the interstellar medium (also called Astrochemistry) is a fascinating mystery that astronomers together with chemists attempt to reveal day by day.

In the past, the space between the stars in our Galaxy, the so-called Interstellar Medium (ISM), was thought to be empty. Nowadays it is unanimously accepted that interstellar matter consists of about 99% gas and 1% dust grains by mass. The interstellar medium gas is in turn composed of hydrogen (~89%), helium (~9%) and heavier elements (~2%) (*e.g. Tielens 2005).*

Moreover, the broad heterogeneity of temperatures ranging from 10 K to a few thousand Kelvin together with an extraordinary variety of number densities extending over 8 orders of magnitude (10^1–10^9 cm^{-3}) clearly demonstrates that interstellar chemistry is expected to be remarkably diverse.

Sections 1.1 and 1.2 describe the physics and the chemistry of the interstellar medium and star-forming regions, respectively.

1.1 The physics of interstellar medium regions

Gaseous species are found to be in a variety of phases: as coronal gas and as ionised and neutral (atomic and molecular) species (Duley & Williams 1984 and references therein). It is possible to distinguish the different ISM regions based on the different nature of these gaseous components. Table 1.1 summarises the diverse ISM environments and their main physical parameters.

Table 1.1. Interstellar medium components and their physical parameters. Adapted from Wooden et al. (2004).

	Temperature [K]	Density [cm^{-3}]
Hot ionised medium	10^6	10^{-3}
Warm ionised medium	10^4	$\geq$10
Warm neutral medium	10^3–10^4	0.1
Atomic cold neutral medium	10^2	10–10^2
Molecular cold neutral medium	5–50	10^3–10^5

As described in Wooden et al. (2004), in the Hot Ionised Medium (HIM) phase the gas is heated through shocks driven by stellar winds from supernova explosions; it is often called *hot coronal gas* due to the fact that its temperature is comparable to the million degree gas found in the Sun's corona. This component can be observed in X-ray emission. In the Warm Ionised Medium (WIM), densities are higher than in the HIM; on the other hand, temperatures are lower. The WIM is mainly composed of HII regions, containing atomic hydrogen that is almost fully ionised; HII regions result from the formation of a massive star. The HIM together with the WIM component constitute the Intercloud Gas. The Warm Neutral Medium is characterised by low density (0.1 cm^{-3}) and temperatures that rise up to 10^4 K. The Atomic Cold Neutral Medium is also atomic, with the only exception being molecular hydrogen. Densities are still low, in the 10–100 cm^{-3} range, and temperatures rise up to ~100 K. Finally, the Molecular Cold Neutral Medium represents the densest component of the ISM because it contains embedded cores in which new stars form. We will mostly focus on these dense clouds in order to explain the first steps in the process of a star formation.

The existence of ISM dense clouds is pivotal for the birth of a star. Dense clouds actually contain the basic ingredients to form both massive and low-mass stars. In particular, the theory of star formation states that a diffuse or quiescent molecular cloud (a region with physical parameters between diffuse and dense clouds) collapses under its own gravity (the so-called *free fall* collapse, *e.g.* Rawlings et al. 1992). The cores inside molecular clouds have masses of typically 10^4 $M_\odot$ and they are denser than the outer regions of the molecular clouds. In this scenario, once atoms, radicals or molecules collide with dust, they are accreted on the surface of dust grains and form an icy mantle up to 0.1 μm thick (Millar & Williams 1993; Kaiser 2002). At this stage, temperatures are as low as 10 K and all species (except H, H_2 and He) efficiently stick on the grain surface; this means that more-or-less every collision of a gas phase species with a cold surface leads to an adsorption and hence growth of the ice layer.

1.2 ISM chemistry in the gas phase

This diversity of ISM components (gas and ice species, energetic particles and photons, described later in this Chapter) promotes a series of reactions that can be categorised depending on their general effects: bond formation processes, which link atoms into complex species; bond-destruction processes, which break large molecules into smaller fragments; bond-rearrangement reactions, which transfer part of one reactant to the other. In general, a distinction can be made among the different types of reactions based on the different way species can interact:

1. Neutral-neutral reactions, involving van der Waals attractive forces;
2. Ion-molecule reactions, occurring when there is a strong polarisation-induced interaction potential that overcomes any activation energy involved;
3. Proton transfers from one species (donor) to another one (acceptor) that has a proton affinity larger compared to that of the donor;
4. Charge exchange reactions, arising when there is an energy level in the product ion that is resonant with the recombination energy of the incoming ion;
5. Radiative recombination reactions, involving the capture of an electron by an ion to form a neutral in an excited electronic state that can radiate. As a result, the emission of a photon results in the attachment of the electron;
6. Collisional association/dissociation or associative detachment, resulting in the ejection of a photon when a neutral species collides with an electron;
7. Radiative association.

All the above types of reactions are examples of gas phase bi-molecular reactions; three-body reactions are also thought to exist between two species whose interaction is stabilised by collision with a third body, although they need higher densities to occur. Apart from neutral-neutral interactions, all the reactions listed play a role in maintaining the ionisation balance. In dark clouds, where temperatures are low and UV radiation cannot penetrate, ion-neutral reactions seem to be the most important mechanism (Herbst & Klemperer 1973). These types of reactions involve the induction of a temporary dipole, which increases the reaction cross-section. A crucial ionisation process is governed by H_2 that is protonated to ${H_3}^+$, an extremely reactive species, acting as proton donor.

The set of information that is crucial to ascertain if a reaction is feasible includes (i) the rate constants that are linked to the speed of a reaction, and (ii) the dynamics in terms of energy barriers, intermediates (temporary molecular entities that react further to form the reaction products), products and degrees of freedom. Since the kinetic energy of interstellar species ranges from 0.8 kJ mol^{-1} (96.2 K, diffuse cloud) to 0.08 kJ mol^{-1} (9.62 K, dense cloud) on average, gas phase reactions under thermodynamical equilibrium conditions in interstellar clouds should be exoergic or only slightly endoergic, exhibiting little or no entrance barrier, and involving exit barriers which are lower in energy than the separate reactants (Kaiser 2002). Due to the low density of the interstellar cloud media, only two-body collisions are relevant. In order to describe them, the classical Arrhenius equation can be used where the rate constant k depends on the temperature T as can be inferred from the following formula:

$$k(T) = Ae^{-E_a/RT}, \tag{1.1}$$

where A represents the pre-exponential factor, R the gas constant, and E_a the classical activation energy. Equation 1.1 can be modified according to different types of reactions (see Chapter 2 for details). In addition to these gas phase reactions, there are several reactions arising on the grain surface. As mentioned above, some of them involve energetic particles, but there is also a series of reactions where both reactants are part of the icy mantle; Section 1.3 is dedicated to the explanation of this grain chemistry in more detail.

1.3 Role of the dust grains and the mechanisms of formation of icy mantle species

1.3.1 Evidence of ISM dust and its composition

Dust represents only 1% of the mass of the ISM (Savage & Mathis 1979) but, despite constituting such a small amount, its presence is testified by several indicators (Williams 2005). For instance, the depletion[1] of the abundance of gaseous atoms relative to hydrogen

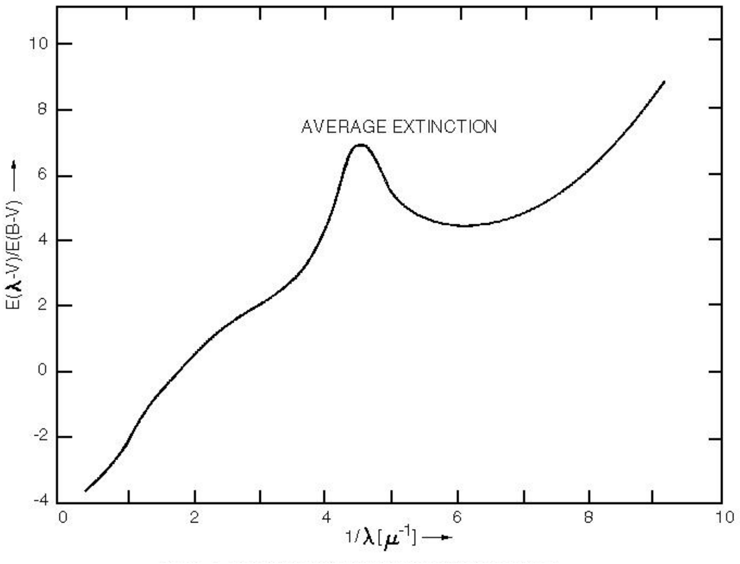

Figure 1.1. The dependence of interstellar extinction on wavelength taken from Bless & Savage (1972).

compared to their cosmic abundance has been attributed to gas elements being locked on solid particles. Another indication of the existence of dust is extinction; the term *extinction* indicates the presence of some matter that, during the passage of light through a certain distance of the ISM, tends to obscure a star (or other sources of radiation). Astronomers measure this quantity (Δm) by comparing two stars of similar spectral type (but at different distances) and by measuring their apparent intensities (I_1 and I_2, respectively) on a logarithmic scale in units of magnitudes (see Equation 1.2) and obtain Δm as follows:

$$\Delta m = 2.5 log_{10}(\frac{I_1}{I_2}). \tag{1.2}$$

The extinction curve has a particular shape (shown in Fig 1.1, taken from Bless & Savage 1972) and scientists strive to reproduce the observed wavelength dependence with theoretical dust grain distribution models (Weingartner & Draine 2001). However, extinction can be estimated at any wavelength from the far UV (100 nm) to the IR (10 μm). In the visible region the extinction is proportional to $1/\lambda$ as shown in Figure 1.1. Moreover, observations show that visible light is linearly polarised and the amount of polarisation

---

[1] The term *depletion*, that has been properly used in this Section, will be employed as a synonym of *freeze-out* (indicating the formation of icy mantles around the dust grain) throughout the thesis.

is estimated to be proportional to the amount of extinction: grains betray their presence by scattering the light and the contingent effect creates a diffuse light, which permeates the Galaxy, the so-called *albedo* or reflectivity. The presence of dust is also clear in spectra: dust grains emit radiation not only in a continuum spectrum but also in spectral features. Specifically, a broad emission or absorption feature centered at 9.7 μm is usually attributed to the Si–O stretch mode, where the broadening is due to the interactions of the Si–O structure with the environment. In dark regions, instead, where grain mantles exist, the strong absorption of light from the background stars is caused by the O–H stretch mode in amorphous H_2O-ice at 3.1 μm.

The composition of dust remains a matter of debate. The major dust components seem to be carbonaceous material (graphite, amorphous hydrocarbons) and silicates (pyroxenes or olivines) (Mathis 1990; Draine 2003). Carbon has been detected in different forms while most of the silicate grains are amorphous (Burke & Brown 2010).

Dust plays a pivotal role in interstellar medium chemistry (*e.g. Savage & Mathis 1979; Williams & Taylor 1996)* and, in particular, it is essential in regulating the temperature of pre-stellar cores, which is kept constant within the 10–20 K range (see review by Tafalla 2005).

1.3.2 Icy mantle chemistry and its composition

The presence of ice on top of interstellar dust was initially theorised by Eddington (1937) although it was only detected for the first time by Gillett & Forrest (1973), who identified H_2O-ice via its mid-infrared absorption against a background source. Looking at dark cloud sources, Öberg et al. (2011) summarised the formation of ices in three steps: (i) the hydrogenation of atoms in a C-rich environment, where water ice is the major component followed by CH_4, NH_3, CO_2 ices; (ii) the production and the freezing of CO onto the grain, that leads to the formation of methanol; (iii) finally, the sublimation of ices occurring as the grains are heated by thermal processes.

The grain surface chemistry is therefore mainly governed by the following three parameters (Herbst & van Dishoeck 2009): i) the accretion rate of the gas species onto the grains; ii) the surface migration rate and iii) the desorption rate. In standard Galactic conditions, the timescale at which gas phase species freeze onto grains is 10^5–10^6 years. This time is shorter than the lifetime of most clouds, which is between 10^5–10^7 years (Herbst & Millar 2008). Hence, during the first stage of star formation a certain amount of all species (ex-

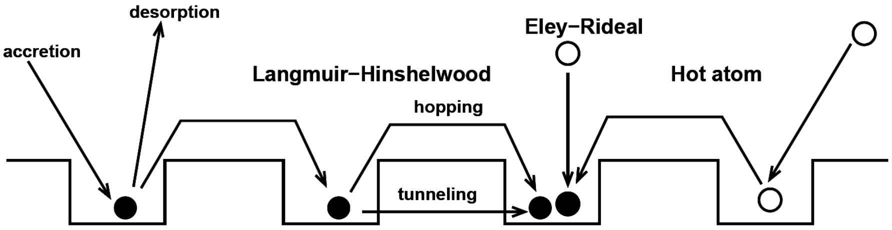

Figure 1.2. Three mechanims for surface reactions: Langmuir-Hinshelwood, Eley-Rideal and hot atom mechanisms. Closed circles are thermalised species and open circles represent non-thermalised species. Image credit to Ioppolo (2010).

cept molecular hydrogen) is depleted onto dust surfaces. The primary process in which the gaseous molecules in the ISM interact with the surface is therefore collision. The so-called *sticking probability* is a measure of how often atoms and molecules will attach to the dust surface; this parameter is related to the collision energy, the surface temperature and the nature of the grains (Leitch-Devlin & Williams 1985). After collision, molecule accretion onto dust particles occurs via weak van der Waals forces, known as physisorption, or via chemical valence forces, known as chemisorption. There are three major mechanisms to describe the grain surface reactions (Herbst & van Dishoeck 2009 and references therein): the Langmuir-Hinshelwood; the Eley-Rideal and the hot atom processes (see Figure 1.2). In the Langmuir-Hinshelwood mechanism, both reactants are already on the grain surface; the diffusion of species occurs by tunnelling or thermal hopping over the energy barrier between the two binding sites. Essentially, once adsorbed, molecules can react by sticking together, with the grain receiving the excess energy. In the Eley-Rideal mechanism, a gas phase species lands on top of an adsorbate and interacts with it. The hot atom mechanism involves an adsorbate and a gas species as for the case of the Eley-Rideal mechanism, but here the gaseous species moves on the grain surface before thermalization, so it is able to collide with the adsorbate.

The role of icy mantles as reaction catalysts was proved for the first time by Hollenbach & Salpeter (1970). In fact, acting as third body, interstellar grains reduce the activation energy of chemical reactions; the excess energy can result in the dissociation of molecules, producing reactive atomic species. As a consequence, gas phase interactions proceed more rapidly. Alternatively, the energy gained can escape into the surface, allowing recombination and simple addition reactions (without dissociation) to proceed significantly. Finally, since the temperature of an icy mantle is low (10 K), most atoms and molecules deposit on the surface and closely coexist for a long time; this gives reactions long enough to occur. The formation of molecular hydrogen clearly illustrates this catalytic effect (Kaiser 2002; Latimer et al. 2008). Since the H–H bond has a binding energy of 4.5 eV, the H_2 molecule (which is formed on the grain surface) is vibrationally excited and hence can desorb from the grain into the gas phase. In the gas phase, this pathway would not be viable as the newly-formed hydrogen molecule is highly rovibrationally excited and would not be able to loose its internal energy via a three-body reaction due to the low density in the medium. Any internally excited H_2 which is formed in the gas phase will dissociate back to the reactants. Moreover, this reaction is also spin forbidden.

Information concerning the composition of icy mantles comes from the continuum infrared emission from stars behind molecular clouds or stars embedded within the cloud. Surface-bound species absorb infrared radiation from these continua, producing spectra with a range of features. These infrared spectra were first recorded at high-resolution by the Infrared Space Observatory (ISO, Gibb et al. 2004) and correlated to laboratory investigations in order to collect data concerning the ice content (Sandford & Allamandola 1990; Allamandola et al. 1988).

The most abundant ice molecule is water, which contributes 70% (Whittet & Bowey 2003) to the ice composition, although there are other inorganic compounds, such as CO, CO_2, NH_3. Some organic molecules have also been detected and, among them, one of the major constituents is methanol (Dartois et al. 1999). Moreover, grains can be charged by ions that stick to them. Ions in the gas will have either enhanced or inhibited collision rates with icy mantles depending on whether the grain is charged negatively or positively. The grain electric charge can be altered by photoelectric emission, with electrons emitted from matter as a consequence of its absorption of energy from electromagnetic radiation. This effect provides for the heating of the surrounding gas (except in the case of low-density clouds, where this process is not dominant, Abbas et al. 2006).

Most of the molecules in the ISM are unsaturated and absorption onto the grain surface results in the immediate hydrogenation of these species. As mentioned before, local thermal heating of dust by a radiation field can increase the rate constant for surface reactions. It follows that surface chemistry increases the molecular diversity in the ISM, further enhanced by the presence of UV radiation. Photolysis of molecules on the grains encourages radicals to be produced that undergo more surface reactions (Garrod et al. 2008a). Penetration of the radiation is controlled by the thickness and the composition of the icy mantle and these two factors may protect larger molecules from photo-destruction; this also allows organic synthesis to occur. As a result, grains are considered a reservoir for many complex organic molecules (Herbst & van Dishoeck 2009).

1.4 Complex organic molecules in the ISM

Organic molecules are composed of C and H atoms and the term *organic* refers to the fact that they represent the constituents of the origins of life, although there is no agreed definition of what organic means. A few heavier elements (such as O, N, S) usually appear in their structural formula (Ehrenfreund & Charnley 2000). By interstellar standards, molecules containing six or more molecules are viewed as complex organic molecules (COMs). More than 175 molecules have been detected in the ISM or in circumstellar environments (see Table 1.2).

The distribution of these organic molecules in the interstellar medium (ISM) varies depending on the physical parameters of the regions and this explains the pivotal role of molecules as probes of the physical conditions and the lifetimes of their environments (Herbst & van Dishoeck 2009). The sources include: circumstellar envelopes around evolved stars, cold interstellar cores, hot cores and corinos, lukewarm corinos, outflows, etc.

Most of the COMs have been identified from their rotational emission spectra in hot cores, molecular regions that are spatially associated with high-mass star formation. With the term hot core (and their low-mass analogs, hot corinos) we define the gas surrounding a protostar, where temperatures are within the 100–300 K range and densities can be as high as 10^8 cm^{-3} (Irvine et al. 1987).

The molecular inventory of hot cores is, therefore, dominated by a copious variety of species: saturated (richer in hydrogen) molecules (CH_4, H_2O, CH_3OH, CH_3OCH_3, C_2H_5OH) which are enriched by a factor of 10^3–10^5 compared to quiescent molecular clouds (Charnley 1995; van Dishoeck & Helmich 1996), complex epoxides (the smallest of which is ethylene oxide, C_2H_4O), aldehydes (for instance acetaldehyde, CH_3CHO), ketones (such as propanone, CH_3COCH_3), and acids (such as formic acid, HCOOH, or acetic acid, CH_3COOH; Ehrenfreund & Charnley 2000). Recently, amino acids have also been searched for and Guélin et al. (2008) calculated an upper limit for the glycine column density of 10^{15} cm^{-2} towards the Orion Hot Core. Moreover, these compact objects are characterised by a

Table 1.2. List of detected interstellar medium molecules categorised along with the number of their atoms.

2	**3**	**4**	**5**	**6**	**7**	**8**	**9**
H_2	H_2O	NH_3	SiH_4	CH_3OH	CH_3CHO	$HCOOCH_3$	CH_3CH_2OH
OH	H_2S	H_3O^+	CH_4	NH_2CHO	CH_3NH_2	CH_2OHCHO	$(CH_3)_2O$
SO	SO_2	H_2CO	CHOOH	CH_3CN	CH_3CCH	CH_3C_2CN	CH_3CH_2CN
SO^+	$HN_2{}^+$	H_2CS	HCCCN	CH_3NC	CH_2CHCN	C_7H	$H(CC)_3CN$
SiO	HNO	HNCO	CH_2NH	CH_3SH	HC_4CN	H_2C_6	$CH_3(CC)_2H$
SiS	SiH_2	HNCS	NH_2CN	C_5H	C_6H	HC_6H	C_8H
NO	NH_2	CCCN	H_2CCO	HC_2CHO	c-CH_2OCH_2	CH_3CO_2H	
NS	$H_3{}^+$	$HCO_2{}^+$	CH_2	CH_2CH_2	CH_2CHOH_2	H_2C_3HCN	**10**
HCl	NNO	CCCH	c-C_3H_2	H_2CCCC		CH_2CHCOH	CH_3COCH_3
NaCl	HCO	c-CCCH	CH_2CN	HC_3NH			$CH_3(CC)_2CN$
AlCl	OCS	CCCS	SiC_4	HC_4H			$HOCH_2CH_2OH$
AlF	CCH	HCCH	H_2CCC	C_5S			CH_2CH_2CHO
PN	HCS^+	$HCNH^+$	HCCNC	C_4H_2			
SiN	c-SiCC	HCCN	HNCCC	HC_4N			**11**
NH	CCO	H_2CN	H_3CO	c-H_2C_3O			$H(CC)_4CN$
SH	CCS	c-SiC_3					CH_3C_6H
HF	C_3	CH_3					
CN	MgNC	CH_2D^+					**12**
CO	NaCN	AlNC					c-C_6H_6
CS	CH_2						
C_2	MgCN						**13**
SiC	HOC^+						$H(CC)_5CN$
CP	HCN						
CO^+	HNC						
CH^+	CO_2						
CH	SiCN						
N_2	AlCN						
	SiNC						
	KCN						

Adapted from `http://www.astro.uni-koeln.de/cdms/molecules`.

few unsaturated species (with a few hydrogen atoms), e.g. cyanoacetylene (HCCCN) and vinyl cyanide (C_2H_3CN). The first species was found toward G10.47+0.03 (Ohishi & Kaifu 1998), while the second one was found toward the Galactic Centre SgrB2(N) (Nummelin et al. 1999).

Absorption spectra arising from molecules in the solid phase are broad and cannot be assigned with as much certainty as narrow gas phase features (Whittet & Bowey 2003). Compared with their gas phase analogues, molecules detected on grain mantles show a weaker absorption (Gibb et al. 2000). The most abundant mantle component is water ice, with a fractional abundance (with respect to the total number of hydrogen nuclei) of 10^{-4}.

Finally, a number of broad emissions in the infrared, arising from re-emission in regions with strong UV or visible radiation, have been assigned to vibrational bands from a class of species known as polycyclic aromatic hydrocarbons (PAHs, Allamandola et al. 1989).

PAHs are planar molecules consisting of carbon rings and hydrogen, rings similar to benzene. PAHs are also much larger than the gas phase species detected by high-resolution spectroscopy (their size ranges up to and beyond 30 carbon but they can also coagulate in order to form clusters, Kimura et al. 2007). Moreover, there is some weak evidence that the well-known but unassigned series of diffuse (broad) interstellar bands seen in the visible as starlight passes through diffuse interstellar matter may be caused by PAHs (Cox & Spaans 2006). Other examples of very complex molecules are fullerenes C_{60} and C_{70}, recently discovered in planetary nebulae (Cami et al. 2010; García-Hernández et al. 2011). It seems that the late stages of the evolution of solar-type stars favour the production of fullerenes. These molecules are very resistant to UV radiation and therefore have long survival times in interstellar space. It is likely that fullerenes, originally formed in planetary nebulae, subsequently populate the interstellar medium and the clouds from which stars and planets form (Cami et al. 2010).

1.5 Overview: Surface experiments

Laboratory experiments provide important information on how molecules form on grain surfaces. A wide range of laboratory investigations has been carried out in order to probe the formation of simple molecules as well as more complex species. The present section summarises (with a few examples) the state of the art in surface experiments of astrochemical relevance.

Most of the experiments in this overview employ a substrate representing the dust surface and an Ultra-High Vacuum (UHV) setup, that reaches a pressure of 10^{-10}–10^{-11} mbar and temperatures down to 12–15 K, combined with a Quadrupole Mass Spectrometer (QMS) for the detection of species. This is the case with the Temperature Programmed Desorption (TPD) experiments, largely used to determine the nature of desorbing species from their masses and the kinetic parameters that govern their desorption.

Infrared (IR) Spectroscopy is another technique applied in studies of astrochemical relevance; it works in two different modes: in reflection mode (Collings & McCoustra 2005; Mautner et al. 2006) or in transmission mode, as in the experiments of Sandford & Allamandola (1993) and Gálvez et al. (2007). Ices are accreted layer by layer and monitored. The surface is irradiated with IR light which is in turn absorbed by the ice at certain frequencies typical of the vibrational modes of the species studied. The information resulting from this procedure concerns the nature of the molecule produced and the amount depleted onto the icy mantles.

1.5.1 Ice mantle chemistry of molecular hydrogen

The first dedicated experimental study involving astrophysical surfaces looked at the formation of molecular hydrogen. In particular, using a QMS, Pirronello et al. (1997) detected HD produced by two different atomic beams of H and D atoms. From TPD studies on olivine, they concluded that the HD formation efficiency decreases as the substrate temperature is increased. Since the recombination of H–H (or H–D) was considered a suitable pathway to produce H_2, this route was subsequently tested on other types of surfaces such as carbon (Vidali et al. 2005) or non-porous amorphous solid water (ASW, Amiaud et al. 2007). All these studies highlighted the fact that molecular hydrogen formation occurs predominantly during the warm-up phase; however, Hornekær et al. (2003) stressed the efficiency of hydrogen recombination at temperatures as low as 8 K. A similar effect was attributed to the different surfaces used to accrete hydrogen: HD formed on porous water ice is accommodated within the pores and subsequently thermally desorbed. On non-porous ice, HD cannot be thermalised in this way, and HD desorbs due to non-thermal desorption effects. It was concluded that HD is formed at low temperatures via the Langmuir-Hinshelwood or hot atom mechanisms. At higher grain temperatures, H atoms are chemisorbed in order to remain on the surface for a time long enough for reaction to occur. This effect was experimentally and theoretically studied on a graphite surface (Baouche et al. 2005).

More recently, Islam et al. (2007) and Latimer et al. (2008) studied the recombination of H and D atoms on a cold graphite surface via laser spectroscopic experiments. The relative populations of the ro-vibrational states have been evaluated and the average rotational temperatures of the nascent HD determined. By estimating the vibrational distribution for HD production in the solid state, the authors confirmed the fact that formation of H_2 on cosmic dust grain analogues needs a considerable amount of internal excitation energy. Therefore a Langmuir–Hinshelwood pathway (which involves more vibrational energy than any other known mechanism of formation for icy mantle species) should be allowed in order to better reproduce the H_2 chemistry.

1.5.2 The physical properties of water ice

The catalytic properties of water ice are closely related to its morphology, which depends in turn on the deposition conditions (Collings et al. 2003; Gálvez et al. 2007; Allamandola et al. 1988). H_2O deposited below 130–140 K forms an amorphous ice film, commonly referred to as amorphous solid water (ASW), which is also the dominant phase in astrophysical environments (Smoluchowski 1978; Klinger 1983; Smoluchowski 1983; Kouchi et al. 1994). At higher temperatures, the changes in porosity and surface area of the ice suggest the transition from ASW to the crystalline state (ASW-CI Smith et al. 1997). At very low temperatures (≤ 38 K), water ice shows high porosity as well as a high density (around 1.1 g cm^{-3}), that both decrease in the 38–68 K range (Jenniskens & Blake 1994). Water ice pores are able to trap volatile species that can escape from the surface during the transition from ASW to ASW-CI, giving rise to the so-called *volcano effect*. This phenomenon is evident thanks to a sharp feature measured during TPD experiments. These spectra also present another peak at around 100 K, indicating the co-desorption of the remnant ice species with water as experimentally observed by Collings et al. (2004).

Since water is very commonly the dominant ice component, several investigations were performed in order to study its chemistry in the solid state. Three main mechanisms have been probed:

1. the sequential hydrogenation of an O atom:

   $O + H \rightarrow OH$

   $OH + H \rightarrow H_2O$,

2. the reaction of OH absorbed on grain surfaces:

   $OH + H_2 \rightarrow H_2O + H$,

3. the sequential hydrogenation of O_2:

   $O + O \rightarrow O_2$

   $O_2 + H \rightarrow HO_2$

   $HO_2 + H \rightarrow H_2O_2$

   $H_2O_2 + H \rightarrow H_2O + OH$.

The first two routes were followed by Dulieu et al. (2007) and products were detected by mass spectrometry. The authors were unable to clarify whether water was formed at low temperatures or during the warm-up phase. The third reaction network was proposed by Tielens & Hagen (1982) and experimentally confirmed by Miyauchi et al. (2008).

1.5.3 The formation of CO-bearing species on grain surfaces

The growth of more complex organic molecules is due to the accretion of simple carbon-bearing species on the grain surfaces. One of the species that has been the target of several laboratory studies is CO_2; for instance, Ioppolo et al. (2009) observed that CO and CO_2 are formed easily after energetic processing of ice mixtures containing C- and O-bearing molecules and carbon grains covered by water ice. Subsequent hydrogenation of CO ices produces formaldehyde and also methanol (Watanabe et al. 2005). Hence, more and more complex species can form via bombardment of simple ices (Dulieu et al. 2010) up to benzene and other polycyclic aromatic hydrocarbons (Thrower et al. 2012). The thermal and non-thermal desorption of the latter species have been extensively investigated by Thrower et al. (2008, 2009). They demonstrated how a broad distribution of binding energies can lead to a significant lengthening of the timescale for desorption of species from the substrate; moreover, they stressed that PAHs can be responsible for the injection of energetic molecules into the gas phase and for inducing chemical change within interstellar ices. UV induced ice chemistry has also been the focus of recent studies by Öberg et al. (2011) and Fayolle et al. (2011).

1.5.4 Ice processing

During the accretion stage as well as once the core collapse terminates (when the gas and magnetic pressure balance the gravitational force), several heating effects can take place and they involve excitation of the surface molecules (Herbst 1995).

Direct cosmic-ray processes involve the dissociation or ionisation of species due to direct collision with cosmic-ray particles (CR). Photo-processes induced by cosmic rays are characterised by the dissociation or ionisation of species due to ultraviolet (UV) photons emitted following H_2 excitation. Finally, photo-process where the dissociation or ionisation of neutral species is caused by UV photons with a standard interstellar UV field can also arise. The different energetic and consequences of the UV and CR impact are described below.

Beside these non-thermal phenomena, an increase in temperature further promotes the sublimation of species from the icy mantles: during the initial collapse, as the pre-stellar

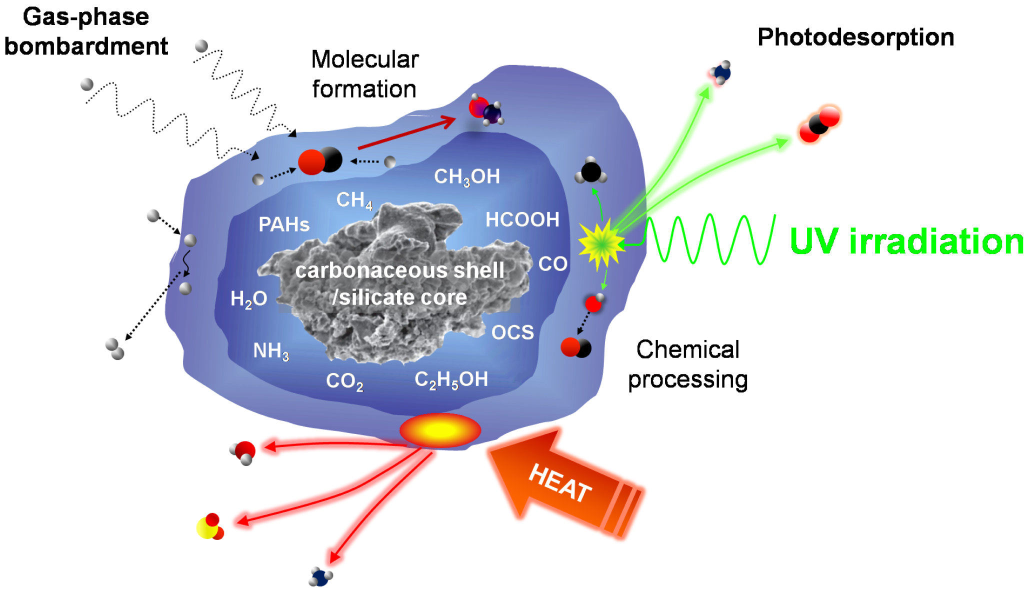

Figure 1.3. The main routes of interstellar ice processing and the major components of interstellar ices. Image credit to Burke & Brown (2010).

core becomes denser, it also becomes opaque; IR radiation is trapped, and the temperature and pressure in the center begin to increase; shock waves therefore propagate outward from the protostar.

Figure 1.3 summarises the main routes of interstellar ice processing (either thermal or non-thermal) that take place in astrophysical environments. The main ice constituents are also highlighted.

1.5.5 The non-thermal desorption of ice

Cosmic-rays (CR) are energetic particles consisting of 97–98% protons and 2–3% helium nuclei, also called α particles, in the low energy range of 1–10 MeV and higher energies up to 1 PeV. The chemical evolution of interstellar ices by bombardment with UV photons or CR particles is relatively well understood thanks to different laboratory studies (Pirronello 1991; Strazzulla & Palumbo 1998; Palumbo et al. 1999; Hudson & Moore 1999; Gerakines et al. 2000). A photon can be absorbed by a single molecule in the ice causing the rupture of a single bond. If an hydrogen atom is released in this photodissociation, it will be internally excited and it might react with a neighbouring species. Compared to UV photons, CR particles penetrate the grain easily and deposit up to 1 MeV inside the icy mantle. Since chemical bonds are up to 10 eV strong, this energy exceeds the stability of the molecule and can be transferred to other target atoms (Kaiser 2002). As a result, a cascade of energetic particles is generated and it terminates with an insertion or addition reaction to double or triple bonds or with hydrogen abstraction. Due to this CR-induced cascade of energetic particles, even if their flux in dense clouds is two orders of magnitude lower than the internal ultraviolet flux, CRs have a greater impact on ISM chemistry. Moreover, unlike UV photons that interact in single quantum processes, CRs do not follow any optical selection rules. Consequently, UV photon and CR processing of ices are expected to synthesise different molecules. Due to these non-thermal phenomena as well as an increase in the gas temperature, species start to desorb from the grain surfaces, inducing a new chemistry in the gas phase.

In conclusion, despite the number of laboratory data obtainable, experiments cannot reproduce the exact ISM conditions because of specific constraints linked to their shorter timescales, the smaller number of species and the complications in recreating low-T conditions. Laboratory data need therefore to be inserted into chemical simulations in order to be of ISM relevance.

1.6 Overview: Databases

Astrochemical databases contain all the existing kinetic data useful for the chemical modelling of interstellar chemistry. Three well-known databases of gas phase chemistry currently exist in Astrochemistry for the ISM. One of the largest established is the UDfA database, previously called the UMIST database[1], created by Prof. Tom Millar (Queen's University of Belfast, NI), first released in 1991 (Millar et al. 1991) and followed by several updated versions in 1995, 1999, 2006. Its fifth version, refined by McElroy et al. (2013), contains up to 6173 gas phase reactions involving 467 species: among them, 47 are new and 1171 are anions. In the last update, state-specific deuterated rate coefficients, deuterium exchange reactions and a list of surface binding energies for many neutral species have also been provided together with the different reaction channels for all the molecules. The second database is the Ohio State University (OSU) database[2], initially developed by Prasad & Huntress (1980) and, since then, kept up to date by Herbst and co-workers.

These two databases differ through using:

1. different approaches to estimate the rate coefficients for the reactions that have not been experimentally studied;

2. different choices of experimental rate coefficients from uncritical compilations;
3. different approximations regarding the temperature dependence of ion-polar neutral reactions.

Much of the data collected by these two databases are based on theoretical calculations rather than laboratory studies. Due to the progress in the experimental techniques and the richness of the data of astrophysical relevance available from the experiments, Valentine Wakelam from the Laboratoire d'Astrophysique de Bordeaux (France), has recently developed a critical Kinetic Database for Astrochemistry[3] (KIDA), that includes the most recent laboratory results in the gas phase useful for modelling various astrochemical environments and planetary atmospheres. In KIDA, each rate of reaction is defined by a number between 0 and 3 that quantifies the reliability of the value chosen for that selected reaction. The network contains nine classes of chemical processes that can be uni-molecular, bi-molecular or three-body interactions. KIDA has been tested against other public databases by using a code named Nahoon, which simulates the abundances of species within a dark cloud. The molecular abundances obtained employing KIDA's reaction network are similar to the ones from the OSU database. This is not surprising as KIDA is based on the OSU compilation.

In the context of the databases, it is worth mentioning The National Institute of Standard Technology (NIST)[4] database as an alternative source of information about chemical reactions of astronomical interest. NIST contains all the experimental and theoretical rates derived for a specific gas phase reaction. Most of the data are relevant for combustion chemistry because of the high range of temperatures in which they have been estimated but some of the coefficients are calculated down to 200 K, which corresponds to the temperatures typical of a hot core source. Moreover, based on energetic considerations, coefficients may be extrapolated down to 10 K or generally assumed constant at low temperature compared to those at 200 K. Finally, David E. Woon (currently a Research Scientist at the Department of Chemistry at the University of Illinois Urbana-Champaign) is maintaining a website called *The Astrochymist*[5], a rich bibliography of astromolecules divided by regions: (i) Interstellar & Circumstellar, (ii) Cometary, (iii) Planetary and (iv) Planetoids. It is a comprehensive catalogue of species that have been detected so far, with their sources and lines and their corresponding references. This website cannot be classified as a proper database although it contains fundamental information (such as the most recent scientific publications in the field).

In general, databases only contain the interstellar medium chemistry occurring in the gas phase. Recently, the OSU database has been extended to include some simple grain surface reactions and the hydrogenations that occur during the freeze-out.

In conclusion, despite the recent progress in the compilation of databases based on empirical data rather than on theoretical assumptions, grain surface chemistry is still very poorly reproduced. The inclusion of a complete set of gas-grain interactions based on laboratory data will certainly represent a next step in database development.

1.7 Overview: Astrochemical Models

1.7.1 Gas phase models

The first models date back to Herbst & Klemperer (1973): simulations were steady-state in nature and based only on the gaseous ISM chemistry. These types of models are also known as depth-dependent models since the abundances of molecules do not change with time but are only functions of depth into a specific astronomical region. Some examples are the simulations of the translucent outer envelopes developed by van Dishoeck et al. (1998) or the ones by Hollenbach & Tielens (1997) that reproduced the chemistry of the dense ultraviolet photon-dominated regions near young stars.

Besides these steady-state models, time-dependent and pseudo-time dependent models have also been developed. In the first case, the abundances of the species are computed as a function of time at a specific depth (A_v) inside the cloud. Based on this approach Millar et al. (1991, 1997) focused on the chemistry of a static dark prestellar core, while collapsing envelopes were simulated by Bergin & Langer (1997). Charnley et al. (1992) implemented the best-known (at the time) hot core model to predict the chemistry occurring at higher temperatures near massive young stars. In particular, they distinguished the different chemical behaviours between the Orion Hot Core and its compact regions.

In pseudo-time dependent models the density is kept constant with time. These kinds of simulations reveal the importance of coupling the chemistry of star-forming regions with multidimensional hydrodynamical codes. For example, Tarafdar et al. (1985) included in their models an hydrodynamic collapse. At the same time, Millar & Nejad (1985) inserted

---

[1] `http://www.udfa.net`

[2] `http://www.physics.ohio.state.edu/~eric/research.html`

[3] `http://kida.obs.u-bordeaux1.fr`

[4] `http://webbook.nist.gov/chemistry`

[5] `http://www.astrochymist.org`

the variation of the chemistry along with the elemental abundances, the gas density as well as the nature of isotopic fractionation. These pseudo-time dependent calculations were reviewed by Millar et al. (1987), who found some constraints due to the insertion of a small number of unmeasured reactions involving oxygen atoms. Herbst & Leung (1989) extended their previous models (Millar et al. 1987) to account for complex neutral organic molecules and molecular ions, showing that gas phase reactions can produce large abundances of very complex species (although only at times well before steady state is reached) thanks to the rapid chemistry triggered by the high temperatures in which a copious amount of COMs are therefore produced (Caselli et al. 1993; Millar et al. 1997).

1.7.2 Gas-grain models

In the past forty years models have been improving along with the development of new more sensitive telescopes. It was found that gas phase chemistry alone cannot account for the variety and richness of molecules observed (mainly in star-forming regions), hence, gas-grain models are needed.

The first gas-grain chemical models were the ones by Allen & Robinson (1977), that extended the work by Pickles & Williams (1977) to include the diffusion and desorption of species with rates estimated in laboratories studies. The first realistic gas-grain model of a quiescent dark cloud was suggested by Tielens & Hagen (1982). The authors reproduced the formation of the dominant solid species, H_2O-ice, through a sequence of hydrogenations of O atoms freezing onto the grain surfaces. After the production of these polar ice mantles (water-rich), they allowed the depletion of CO to form an apolar ice layer (water-poor) that led to the build up of more complex molecules.

Gas-grain models can adopt different procedures in treating the chemistry and physics towards various interstellar medium environments. First of all, it is important to stress that the accurate coupling of gas phase and grain surface processes in the chemical models is difficult due to the diverse nature of the chemistry in each phase. The models currently available are mainly based on different approaches in the way they evaluate the rates for the reactions that they include. We can therefore distinguish the following methods:

1. The *rate equation system* is a deterministic treatment assuming averaged concentrations or number densities as well as a large volume of gas. Reaction rates are derived from the concentrations of the reactants (when molecules form) or from the

amount of the product (in the case of destruction mechanisms) and from constant parameters (like rate coefficients and partial reaction orders). UCL_CHEM (Viti & Williams 1999), the chemical model employed in the present thesis, is based on this approach. Another example where this method has been applied to the study of the deuterium fractionation is the work by Roberts & Millar (2000). The simplicity of this approach has been questioned by Garrod (2008b) when it is applied to grain surface reactions. The grain chemistry occurs indeed on finite surfaces and rates can therefore be overestimated. Caselli et al. (1998) tried to rectify the rate equation approach by modifying the rate coefficients for the processes occurring on the grain surfaces; however, since changes were empirical, the authors found a convergence with exact techniques only at low temperatures where hydrogen is the only species diffusing on the grain surface. Garrod (2008b) further amended the functional form of the production rate itself instead of making changes only in its rate coefficients. As a result, he improved the accuracy of the rate equation method in large chemistry networks that cannot be modelled with exact techniques.

2. *Macroscopic stochastic-methods.* This category can be in turn divided into the master equation approach and Monte Carlo simulations. The first one consists of a series of first-order differential equations describing the time evolution of the probability of a system to occupy each one of a discrete set of states. The second one is based on a class of computational algorithms that rely on repeated random sampling to compute their results.

Besides these two main categories, Stantcheva et al. (2002) coupled the deterministic method with the stochastic, developing the so-called *hybrid schemes* valid only for the case of a small reaction network. Furthermore, Barzel & Biham (2007) implemented the *method of moments* (where with the term *moment* we refer to a quantitative measure of a shape for a set of points, such as the population distribution of a transitional state) involving the calculation of second moments of population from a master equation standpoint. Although reaction rates obtained by employing this method are quite accurate, the population can contain some uncertainties and this treatment has not been tested against networks that account for activation energies.

A revised approach of the Monte Carlo method has been implemented by Chang et al. (2007). This is an example of microscopic methods that look at the penetration of species into layered ices; it also accounts for the accretion, the hopping and the desorption of molecules. Cuppen et al. (2009) extended this treatment using the so-called *random-walk* Monte Carlo approach in order to simulate microscopic grain surface chemistry over long timescales. At the same time, Vasyunin et al. (2009) implemented a new macroscopic Monte Carlo method that follows both solid and gas phase chemistry for up to 10^6 years. Their results do not significantly differ from those obtained by rate equations if it is assumed that H diffuses on the surface only by classical hopping from site to site. On the other hand, if H atoms tunnel rapidly, the new approach strongly diverges from the rate equation method.

A recent multilayer mantle treatment has been implemented by Taquet et al. (2012). With the aim of simulating the synthesis of COMs on the grain surfaces, the authors focused on the first stage, namely the icy mantle formation during the dense and cold pre-collapse phase and they looked in detail at the porous structure of ices. Based on laboratory results, they concluded that UV photons only penetrate a limited number of monolayers depending on the absorption cross section of icy molecules; therefore modelling the photolytic processes in ices requires a distinction between their surface and their bulk. The first attempt in this direction was made by Hasegawa & Herbst (1993) that considered the formation of an inert mantle due to the accretion of particles onto it. They observed that the differences between their three-phase model and the commonly adopted two-phase model are small for stable species but they become non-negligible for reactive species at large timescales.

A last important point that needs to be discussed is the presence of ions in the chemical reaction network. Unlike positive species that have always been included in the astrochemical models, so far, interactions between negatively-charged gas phase species and dust grain surfaces have been largely neglected. Anions, in fact, have been detected towards different pre-stellar cores as well as the envelopes of some low-mass protostars (Sakai et al. 2007; Gupta 2009; Cordiner et al. 2011). The major formation mechanism of negative ions is thought to be radiative attachment of an electron to the parent neutral. Alternatively, for the case of weakly-bound neutral reactants, dissociative attachment can be considered. On the contrary, there are four different mechanisms that drive a negative ion to be destroyed: i) associative detachment, ii) ion-molecule reactions, iii) mutual neutralisation interactions with positive ions, and, finally, iv) photodetachment. Millar et al. (2007) suggested the synthesis of hydrocarbon anions toward various interstellar and circumstellar environments, but only recently, Cordiner & Charnley (2012) included a more complete reaction network for anions and investigated their abundances in dense environments.

1.7.3 Modelling of star-forming regions

In general, the aim of models is to reproduce the observed abundances of species towards different ISM environments and, in this attempt, make predictions of their loss and formation reaction pathways. In the present thesis I will mostly focus on the star-forming region chemistry.

The first stages in the formation of a star can be divided into three phases and the result is a compact object named *protostar*. During the initial cold phase, a fairly diffuse medium in an atomic form (apart from molecular hydrogen) undergoes a gravitational (isothermal) collapse; atoms accrete around the grain surfaces because temperatures are as low as 10 K and new species can be formed thanks to the catalytic action of the grain. The following warm-up phase involves the inner envelope of the protostar that begins to be heated up; the sublimation of the icy mantles continues until the final temperatures are reached (usually 100–300 K): at this stage, the final hot-core phase starts. Each phase (cold, warm or hot) is characterised by a very specific chemistry that produces different types of mantle species categorised as zeroth-generation, first-generation and second-generation organic molecules and defined as follows (the present distinction is based on Herbst & van Dishoeck 2009):

1. Zeroth-generation species include large molecules formed on the grain surface during the first cold step. An example is methanol, produced via subsequent hydrogenations of CO.

2. First-generation species form when the cold core is becoming a Young Stellar Object (YSO). Methanol and other molecules produced during the cold core step can now photodissociate giving rise to many radicals such as CH_3O or HCO that diffuse on the surface and interact with each other allowing the synthesis of larger molecules.

3. Second-generation species appear during the icy mantle sublimation at the high temperatures of hot cores/corinos. Only gas phase reactions can occur and particularly they consist of ion-molecule or neutral-neutral reactions.

Different physical parameters are needed in order to simulate the variety of events occurring during the three steps of the protostar formation process and models can account for more than one stage.

Cold phase models are usually pseudo-time-dependent codes (see Section 1.7.1) where time-independent physical conditions are assumed (although there are examples of models where density and temperature are varied with the core size or the collapse timescale, *e.g.* Aikawa et al. 2012). Initial abundances of atoms (apart from molecular hydrogen) are set and molecular hydrogen is formed during the diffuse stage (Wakelam et al. 2006). A surface chemistry can be included during the cold stage. The first model under this category was that by Brown et al. (1988). Studying the case of the Orion Hot Core, the authors only consider the freeze-out of species on the grain surfaces without following their chemical evolution. It is important to notice that the presence of grain chemistry at this stage implies the inclusion of non-thermal desorption effects because all species are depleted almost totally from the gas at times exceeding 10^6 years, if the gas density is $\leq 10^4$ cm^{-3} (Roberts & Millar 2000).

Unfortunately, non-thermal desorption mechanisms are poorly understood. Roberts et al. (2007) investigated three different mechanisms: desorption resulting from H_2 formation on grains, direct cosmic-ray heating and cosmic-ray induced photodesorption. Direct UV photodesorption has only recently been included by Hassel et al. (2008) based on laboratory data from the experiments by Öberg et al. (2007).

Concerning the warm-up phase models, the first study to treat a non-instantaneous icy mantle sublimation was Viti & Williams (1999). They considered an increase in temperature due to a nearby star and they assumed the timescale (determined from this nearby star) to be likely comparable to the lifetime of the hot cores. In consequence, the evaporation of different species occurred at different ages, leading to chemical differentiation in time and space within the hot core. After a few years, their model was extended to include experimental results from TPD experiments (Collings et al. 2004; Viti et al. 2004). In this study, the timescale was empirical and based on the mass-luminosity relationship for the case of massive stars as in Molinari et al. (2000, 2002). As the surface temperature increases from 10 K to ~20 K, some of the more volatile species such as CO, CH_4 and N_2 start to desorb. The heavier molecules remaining on the grain surface begin to diffuse faster. The authors did not include any surface chemistry after the cold phase. A surface chemistry during the warm-up of ices was inserted later by Garrod et al. (2007): they incorporate the formation of complex organic molecules during both the cold and the warm-up phases. In order to create reactive species, Garrod et al. (2007) introduced a chemistry triggered by the cosmic-ray induced UV photons: a small number of radical-radical reactions were therefore considered. Later, Garrod et al. (2008a) extended their model to include several surface reactions involving a great number of radicals. The latter species were also divided into two categories and classified as primary radicals, when produced by photodissociation reactions occurring during the cold era, or secondary radicals, if made from interactions where a primary radical is actually one of the reactants.

Finally, after the ice sublimation, high-temperature chemistry can take place in the gas phase. The gas phase component is now enriched with the new molecules that formed on the grain surface. Moreover, due to the higher temperatures (compared with those characterising the cold phase) many endothermic or exothermic processes with barriers can also take place.

In general, the outputs from the simulations are the fractional abundances of the species within a selected astronomical object. The reliability of these theoretical results is usually tested by comparison with those from observations available for the particular region studied.

The work presented here concentrates on predicting the chemistry for important COMs in star-forming regions.

1.7.4 This thesis

In the present thesis, we model a more complex gas-grain chemistry under physical conditions relevant for the interstellar medium, by coupling our existing chemical model (see Chapter 2) with the most recent laboratory data on the formation of important COMs. The aim is to reproduce the ISM chemistry more accurately. Specifically, in Chapter 3 we focus on the formation of methyl formate on icy mantle analogues and its production towards different astronomical regions; Chapter 4 describes the formation of ethylene oxide on icy mantle analogues of Highly Ordered Pyrolytic Graphite (HOPG); moreover, we explain the way we include, in our chemical model, the chemistry experimentally observed for this species. Chapter 5 represents an extension of Chapter 4 to include the production of one of the isomers of ethylene oxide, acetaldehyde. In this study we also employ another chemical code, the MONACO model, to look at the formation of both molecules in dense cores and to compare the new results with those obtained from our previous study. We also investigate the effects of a revised reaction scheme for the reaction between oxygen and ethylene in the gas phase on the abundances of the species included in our code (Chapter 6). We finally speculate on the depletion of S-bearing species on grain surfaces, by inserting new theoretical and experimental data regarding their chemistry in a solid state; our preliminary results are reported in Chapter 7. The main tool used in our research is UCL_CHEM, an example of a gas-grain chemical model further described in Chapter 2.

Chapter 2

The UCL_CHEM code

Several chemical models have been developed in order to reproduce the processes occurring in the Interstellar Medium. A complete chemical modelling of a cloud in the ISM should consider the following parameters:

1. Observational contraints, such as column densities (the amount of material in an imaginary cylinder of unit cross-section between a reference system and an astronomical object) for the species inside a cloud; observations inform us about the chemical composition of that specific astronomical region.
2. The physical conditions within the cloud, such as temperature, number density and extinction.
3. The transport processes, such as diffusion, collisions and shocks.
4. The photochemistry, that is an estimation of the radiation field around the stars during their formation or due to pre-existing stars.
5. The chemical reaction rates and their temperature dependence.
6. The network of chemical reactions, involving the processes described in Chapter 1 and other processes, such as isotope-exchange and isomerism.

The outputs of these models are usually a series of relative concentrations for the cloud which are then compared with the observations. Information about the age of the cloud and its evolution may be obtained from these models.

UCL_CHEM is an example of a gas-grain chemical model. It was first developed by Viti & Williams (1999) and subsequently extended by Viti et al. (2004) and Viti et al. (2011). This code estimates the fractional abundances (with respect to the total number of hydrogen nuclei) of gas and surface species in every environment where molecules are present. It is in fact very modular such that it can be used to describe a large variety of astronomical regions, from star-forming regions to molecular gas in external galaxies. For the purpose of the present thesis, the 2004 version of UCL_CHEM has been adapted to model mainly dark clouds, low and high-mass star-forming regions and, in the next two sections, we describe how we use it for our studies.

2.1 Physical model and initial conditions

The model performs a two-step simulation.

Phase I starts from a fairly diffuse medium in atomic form (apart from H_2) and undergoes a free-fall collapse until densities typical of the gas that will form the hot cores or the hot corinos are reached (10^7 cm^{-3} and 10^8 cm^{-3}, respectively). During this time, atoms and molecules are depleted onto the grain surfaces and they hydrogenate when possible. The depletion efficiency is determined by the fraction of the gas phase material that is frozen onto the grains. This approach allows a derivation of the ice composition by a time-dependent computation of the chemical evolution of the gas-dust interaction process. The initial elemental abundances of the main species (such as H, He, C, O, N, S, Si and Mg) are the main inputs for the chemistry. We usually assume that, at the beginning, only carbon is ionised and half of the hydrogen is in its molecular form. The other elements are all neutral and atomic. Elemental abundances at the start of Phase I are adapted from Sofia & Meyer (2001) and they are reported in Table 2.1.

Other input parameters affecting the model chemistry are summarised in Table 2.2. They include the temperature chosen for the isothermal collapse (`temp`), the cosmic ray ionisation rate (ζ, see Section 2.2), the radius of the cloud (`size`) that, along with the density, determines the visual extinction of the core. The initial density (`dens`) and the density of the molecular cloud at the end of Phase I (`df`) can also be set (we usually consider an ab initio approach with density values typical of a diffuse medium); we can opt to stop Phase I based on a specific final time (`tfin`) or whenever the final density is reached. Freeze-out reactions are included in the reaction network in order to allow the

Table 2.1. Initial fractional abundances (compared to the total number of hydrogen nuclei) of selected species taken from Sofia & Meyer (2001).

Element	Fractional abundance
He	0.075
N	8.52×10^{-5}
O	4.45×10^{-4}
C	1.79×10^{-4}
Si	1.43×10^{-6}
S	1.48×10^{-6}
Mg	5.12×10^{-6}

Table 2.2. The main input parameters in UCL_CHEM.

Physical parameters		Phase
`temp`	temperature of the isothermal collapse	I
ζ	cosmic-ray ionisation rate	I–II
`size`	the core radius	I–II
`dens`	initial densities	I
`df`	final density	I
`tfin`	final collapse time	I
`fr`	freeze-out efficiency	I
`maxt`	final gas temperature	II

formation of mantle species. The depletion efficiency (`fr`) can be modified by adjusting the freeze-out fraction of CO.

Phase II is the warming-up phase and it follows the chemical evolution of the remnant core when the hot core itself is formed. Before running phase II, we can choose a final gas temperature (`maxt`) for the astronomical object studied. Phase II simulates the effect of the presence of an infrared source in the centre of the core or in its vicinity by subjecting the core to an increase in the gas and dust temperatures. We derived the temperature of the gas (that is assumed to be the same as the dust temperature) as a function of the luminosity (and therefore the age) of the protostar, using the observational luminosity profile of Molinari et al. (2000). The duration in which the grains are warmed from very low temperatures (~10 K) to values above the water ice desorption temperature (~100 K) is determined by the time taken for a pre-stellar core to evolve towards the main sequence. This contraction time was evaluated by Bernasconi & Maeder (1996) based on the observed molecular line width in nearby dark clouds. As stated by Viti et al. (2004), the temperature reaches its maximum of about 200–300 K at different times depending on the mass of the new-born star. Using the contraction times provided by Bernasconi & Maeder (1996), the authors evaluated the temperature as a function of the mass of the star. For example, considering a star with a mass of 25 $M_\odot$ the temperature profile follows the trend below:

$$T_d = 10 + (1.706 \times 10^{-4} \times t^{1.289}) \qquad \mathrm{K} \tag{2.1}$$

where T_d is the temperature profile of gas and dust in the core surrounding the stellar object, t is the evolutionary age in year of the collapsing core, 1.706×10^{-4} and 1.289 are two constants derived from the boundary conditions (t=0 and t=10^5 years). Awad et al. (2010) developed the code to include the spatial distribution of a collapsing cloud with the aim of estimating the size of typical hot corinos (i.e. adding a spatial component to the model).

The treatment of evaporation can be either time-dependent (where large numbers of mantle species desorb in various temperature bands according to the experimental results of Collings et al. 2004) or instantaneous (in that all species will desorb from the grain surfaces at the first time-step). In the first case, species are divided in 5 categories (CO-like, H_2O-like, intermediate, reactive and refractory) according to their particular desorption behaviour: from the pure species, from a monomolecular layer on water ice, from the volcano effect (when the ASW ice converts to crystalline) and from co-desorption with water. More details on this thermal pseudo-time-dependent desorption can be found in Viti et al. (2004).

Non-thermal desorption of species is also taken into account and is based on the study by Roberts et al. (2007). Three desorption mechanisms are included in UCL_CHEM and they result from H_2 formation on grains, direct cosmic-ray heating and cosmic-ray photodesorption. According to the experimental work by Creighan et al. (2006), part of the ~4.5 eV released in the exothermic surface formation of molecular hydrogen is transferred to the grain surface; it follows a local heating which may thermally desorb weakly-bound mantle species (Duley & Williams 1993). The other two desorption effects result from the impact of cosmic-ray particles that can evaporate icy mantle species either directly or after excitation of the absorbing gas that in turn emits a UV photon. On the other hand, we do not account for direct UV photodesorption.

Finally, the outputs obtainable from the code consist of the fractional abundances of all the species (in both gas phase and on the grain surface) as a function of time. Fractional

Table 2.3. Types of gas phase reactions included in UCL_CHEM and their mathematical treatments.

Type of reaction	Rate constant
Two-body reactions	$k(T) = \alpha(T/300\ \mathrm{K})^{\beta} e^{-\gamma/T}$ [$\mathrm{cm^3\ s^{-1}}$]
Direct cosmic-ray reactions	$k(T) = \alpha\zeta$ [$\mathrm{s^{-1}}$]
Photoprocesses induced by cosmic-rays	$k(T) = \alpha(T/300\ \mathrm{K})^{\beta}\gamma/(1.0\text{-}\omega)\zeta$ [$\mathrm{s^{-1}}$]
Photoprocesses	$k(T) = \alpha e^{-\gamma Av}$ [$\mathrm{s^{-1}}$]
Electronic recombination and attachment	$k(T) = \alpha(T/300\ \mathrm{K})^{\beta} e^{-\gamma/T}$ [$\mathrm{cm^3\ s^{-1}}$]

abundances of molecules are calculated as a ratio of the total number of hydrogen nuclei ($n(\mathrm{H}) + 2n(\mathrm{H_2})$), where n stands for number density [$\mathrm{cm^{-3}}$].

2.2 The chemistry of UCL_CHEM

In order to describe the chemical behaviours characterising Phase I and Phase II, the code includes two networks: one for the reactions occurring in the gas phase and one reproducing the ice chemistry.

The gas phase network is generally based on the UMIST database (Millar et al. 2000a), although some changes have been made to the rate coefficients as discussed during the course of this thesis. UCL_CHEM adopts a rate equation approach (see Section 1.6 for more details). Table 2.3 contains the types of reactions included in the gas phase network and their corresponding rate constants.

Bimolecular reactions, where an exothermic proton transfer occurs between an ion and a neutral species and electronic recombination, in which the recombination of a positive ion and an electron results in the dissociation of the molecule, can be both described by a Kooij formula. This formula is a modified version of Arrhenius' equation, where T is the gas temperature, α is the cosmic-ray ionisation rate, β contains the dipole effect and γ represents the probability per cosmic-ray ionisation that the photoreaction takes place. Regarding β, this coefficient includes the enhancement of ion-neutral rate coefficients for cases in which the neutral has a large, permanent electric dipole moment. This effect results in a rate coefficient that has a $T^{-\frac{1}{2}}$ dependence at low temperature (10–50 K), as observed by Herbst & Leung (1986). The reaction rate constants for both direct and indirect ionisation due to cosmic-ray impact depend on the H_2 cosmic-ray ionisation rate, referred also as ζ_0. We assume that every cosmic-ray ionisation of H_2 will eventually produce a molecule of H_3^+ and so the abundance of this ion is often used as a tracer of the cosmic-ray ionisation rate, ζ. The inferred values of ζ are of the order of 10^{-17} s^{-1}, which is now routinely called the *standard* ISM cosmic-ray ionisation rate, or ζ_0. For cosmic-ray-induced photoreactions another parameter has to be taken into account: the albedo due to the presence of the dust grain in the far ultraviolet (typically ω=0.6 at 150 nm, Woodall et al. 2007). For interstellar photoreactions, we need to take into account the continuum attenuation of the UV radiation from the dust, while UV photons are penetrating the cloud. A_v represents therefore the visual extinction which acts to dilute the radiation field as one moves into the medium reducing the effects of photoreactions. In contrast, α is the unshielded interstellar ultraviolet radiation field.

As mentioned above, grain surface reactions are also included. First of all, we allow the freeze-out of gas phase species onto the dust surface. This leads to hydrogenation reactions. These processes are controlled by a free parameter named `fr` (or depletion efficiency) that determines the fraction of the gas phase material that is frozen onto the grains. We generally assume a greater depletion of species occurring in denser interstellar regions. The mathematical treatment of the freeze-out is based on the equation developed by Rawlings et al. (1992), which describes the rate of depletion of a gas phase species in terms of the local conditions and the grain properties:

$$\frac{dn(i)}{dt} = 4.57 \times 10^4 d_g a^2 T^{0.5} C S_i m_i^{-0.5} n(i) \qquad \mathrm{cm^{-3}s^{-1}} \tag{2.2}$$

where d_g is the ratio of the number density of the grains to that of hydrogen nuclei, a is the grain radius in cm, S_i is the sticking probability (that can be 0 or 1), m_i is the molecular mass of species i in amu and C is a factor included to account for electrostatic effects and has slightly higher values for positive ions since grains carry a small negative charge.

The expansion of the grain surface reaction network to include the most recent experimental studies on surface chemistry forms the topic of the present thesis and, specifically, we start by looking at the formation of an important COM, methyl formate, on icy mantle analogues (Chapter 3).

Chapter 3

Methyl formate towards different astrochemical environments

The work presented in this Chapter is based on the paper by Occhiogrosso et al. (2011) in collaboration with S. Viti, P. Modica and M. E. Palumbo.

Methyl formate ($HCOOCH_3$) is the simplest example of an ester. It is derived from formic acid (HCOOH), where a methyl group is attached to the carboxyl group. It is an important complex organic molecule that was first detected by Brown et al. (1975) towards Sagittarius B2(N), the richest molecular source in the Galaxy, located in the Galactic Centre giant cloud Sagittarius B2. Methyl formate is considered to play a key role in understanding the origin of life because it leads to the synthesis of bio-polymers.

Methyl formate has two structural isomers, glycolaldehyde ($HCOCH_2OH$) and acetic acid (CH_3COOH), but it has been reported that this molecule is the most abundant among these isomers (Hollis & Churchwell 2001). Its column density in the Orion Hot Core was derived to be 9.4×10^{15} cm^{-2} by Ikeda et al. (2001) and this value was confirmed by Sakai et al. (2007). Methyl formate has also been detected in the G31.41+0.31 hot molecular core (HMC); its column density is observed to be 3.4×10^{18} cm^{-2} around this region. Cazaux et al. (2003) observed methyl formate in the hot core around the protostellar object IRAS 16293-2422 and they estimated a column density of 2.5×10^{16} cm^{-2} for this molecule. Hence, methyl formate seems to be ubiquitous in star-forming regions.

Table 3.1. Gas phase routes of methyl formate or protonated methyl formate formation investigated in previous studies. *R* represents a reactant, *P* is a product; α, β, γ are the rate parameters (see Table 2.3); α is in units of cm^3 s^{-1} for all the reactions apart from the direct photodissociation where α is in s^{-1}; T is the temperature (in K) at which rates have been calculated or measured.

Reference	R1	R2	P1	P2	α	β	γ	T[K]
1	$CH_3OH_2^+$	H_2CO	$CH_3OCOH_2^+$	H_2	3.0×10^{-10}	0	0	300
1	CH_3^+	HCOOH	$CH_3OCOH_2^+$		2.2×10^{-11}	0.0	0	100
2	$H_2COHOCH_2^+$	e^-	$HCOOCH_3$	H	1.5×10^{-9}	-0.5	0	10–300
2	CH_3^+	HCOOH	$CH_3OCOH_2^+$		1.0×10^{-11}	-1.5	0	10–300
3	$HCOOH_2^+$	CH_3OH	cis-$CH_3OCOH_2^+$	H_2O	2.0×10^{-9}	-0.5	2810	10–300
3	$HCOOH_2^+$	CH_3OH	trans-$CH_3OCOH_2^+$	H_2O	2.0×10^{-9}	-0.5	3310	10–300
3	$CH_3OH_2^+$	HCOOH	cis-$CH_3OCOH_2^+$	H_2O	1.8×10^{-10}	-0.5	1320	10–300
3	$CH_3OH_2^+$	HCOOH	trans-$CH_3OCOH_2^+$	H_2O	1.8×10^{-10}	-0.5	0	10–300
4	$CH_3OH_2^+$	HCOOH	trans-$CH_3OCOH_2^+$	H_2O	1.7×10^{-11}	0.0	0	300

[1] Horn et al. (2004)
[2] Garrod & Herbst (2006a)
[3] Laas et al. (2011)
[4] Cole et al. (2012)

Several studies have been carried out on methyl formate to understand its formation mechanisms, but it is still debated whether complex organic molecules form on icy dust mantles during the cold phase, on grains during the warm-up phase or in the gas phase. Despite a large activation energy barrier between protonated methanol and formaldehyde (Horn et al. 2004), Garrod & Herbst (2006a) found that the reaction between $CH_3OH_2^+$ and H_2CO is viable during the icy mantle sublimation phase. Moreover, very recently, Laas et al. (2011) have proposed two Fischer esterification pathways (the acid-catalysed reaction of a carboxylic acid with an alcohol to give an ester) that occur during the warm-up phase, involving protonated formic acid and methanol and protonated methanol and neutral formic acid, respectively. Both reactions have two channels that correlate to cis and trans forms of protonated methyl formate. They emphasised that methanol photodissociation branching ratios and warm-up timescales influence the relative ratios between these two geometries. Cole et al. (2012) only focused on trans-methyl formate; the rate constants for its production in the gas phase were experimentally determined using a flowing afterglow-selected ion flow tube apparatus at 300 K. The gas phase reactions leading to the formation of methyl formate or protonated methyl formate with their corresponding rate parameters are summarised in Table 3.1.

Recently, Vasyunin & Herbst (2013) theoretically examined the formation of complex organic molecules found in the cold cores L1689b and B1-b with gas temperatures of 10 K (Bacmann et al. 2012; Cernicharo et al. 2012). They proposed a scenario where methyl formate in the cold regions is synthesised via gas phase ion-molecule and neutral-neutral chemistry from simpler precursors such as formaldehyde and methanol. These precursors are formed on icy surfaces of interstellar grains, and then ejected into the gas via reactive desorption.

The possibility that more complex species are formed at low temperatures on surfaces has been investigated before (*e.g. Charnley 1997; Herbst & van Dishoeck 2009)* and in particular, methyl formate production on dust surfaces was first proposed by Herbst (2005): CO, C and O lead to the formation of the CH_3O and HCO radicals, both known as methyl formate precursors. Based on these reactants and using energetic electrons at 10 K, laboratory experiments were performed by Bennett & Kaiser (2007) in order to produce methyl formate and estimate the rate coefficients for this reaction. Different experiments involving methyl formate were also performed by Gerakines et al. (1996) and Öberg et al. (2009), who formed this molecule after ultraviolet (UV) photolysis of pure methanol and $CO:CH_3OH$ ice mixtures.

Recently, a laboratory study by Modica & Palumbo (2010) has suggested a new solid state route of formation for this molecule. By using infrared spectroscopy in the 4400–400 cm^{-1} range for *in situ* monitoring of the sample during the experiments, they simulated a cosmic ion irradiation of a binary mixture containing CH_3OH and CO ice: methyl formate was subsequently released into the gas phase after sublimation of these icy samples.

In the present work, we include the Modica & Palumbo (2010) experiments in our chemical model UCL_CHEM (Viti et al. 2004 , also see Chapter 2), by extrapolating from the experiments a new rate coefficient for the formation of methyl formate on grains. Our purpose is to investigate whether surface reactions during the cold phase *alone* can account for the observed abundances of methyl formate in massive star-forming regions and around low-mass stars. In Section 3.1, we describe the experimental procedure; physical and chemical details of the chemical model are listed in Section 3.2. In Section 3.3, we qualitatively model four different sources, and present our findings. Section 3.4 contains a brief comparison between our results and those from observations; conclusions are summarised in Section 3.5.

3.1 Formation of methyl formate on icy mantle analogues

Experiments have been performed in the Laboratory of Experimental Astrophysics in Catania (Italy) by Dr. Paola Modica and Prof. Maria Elisabetta Palumbo. Solid samples were prepared and irradiated in a stainless steel vacuum chamber where pressure is generally kept below 10^{-7} mbar. The gas mixture to be investigated was injected into the chamber through a needle valve where it froze onto the substrate (Si or KBr) placed in thermal contact with the tail section of a cryostat (10–300 K). After deposition, the samples were bombarded by 200 keV H^+ ions. Ions are obtained from an ion implanter interfaced with the vacuum chamber. The beam used produces current densities in the range from 0.1 to a few μA cm^{-2} in order to avoid macroscopic heating of the target. Infrared transmittance spectra of the samples were obtained before and after each step of irradiation by a Fourier Transform Infrared (FTIR) spectrometer (4400–400 cm^{-1}= 2.27–25 μm). More details on the experimental procedure can be found in Palumbo et al. (2004) and in Modica & Palumbo (2010).

Pure CH_3OH and a CO:CH_3OH mixture were irradiated at 16 K with the H^+ ions. In both cases, after irradiation, the IR spectra showed several absorption bands which testified to the formation of new molecules not present in the original sample. Among these, two bands due to CH_4 appeared at 3010 and 1304 cm^{-1} (Palumbo et al. 1999); CO_2 bands appeared at 2344 and 660 cm^{-1} ($^{12}CO_2$) and at 2278 cm^{-1} ($^{13}CO_2$); H_2CO was detected at 1720 cm^{-1} (Hudson & Moore 1999); $C_2H_4(OH)_2$ (ethylene glycol) was observed at 1090 cm^{-1} (Hudson & Moore 1999). Moreover, a band was observed near 1160 cm^{-1} and was attributed to methyl formate ($HCOOCH_3$), and a band near 1067 cm^{-1} was assigned to glycolaldehyde ($HCOCH_2OH$; Modica & Palumbo 2010).

Figure 3.1 shows the ratio between the column density of methyl formate and methanol, $N(HCOOCH_3)/N(CH_3OH)$, as a function of ion fluence [ions cm^{-2}], measured after each step of irradiation. The experimental data have been fitted with an exponential curve

$$N(\mathrm{HCOOCH_3})/N(\mathrm{CH_3OH}) = A(1 - \mathrm{e}^{-\sigma \Phi}), \tag{3.1}$$

where A is the asymptotic value, σ is the cross section in cm^2 and Φ is the ion fluence in units of ions cm^{-2}. The fitting procedure gives A= 0.0042 and σ= 8.6×10^{-15} cm^2.

To apply the laboratory results to the interstellar medium (ISM) conditions we assume a standard ionisation rate (ζ = 3×10^{-17} s^{-1}) and derive the flux $F_{\rm ISM}$ = 0.5 ions cm^{-2}

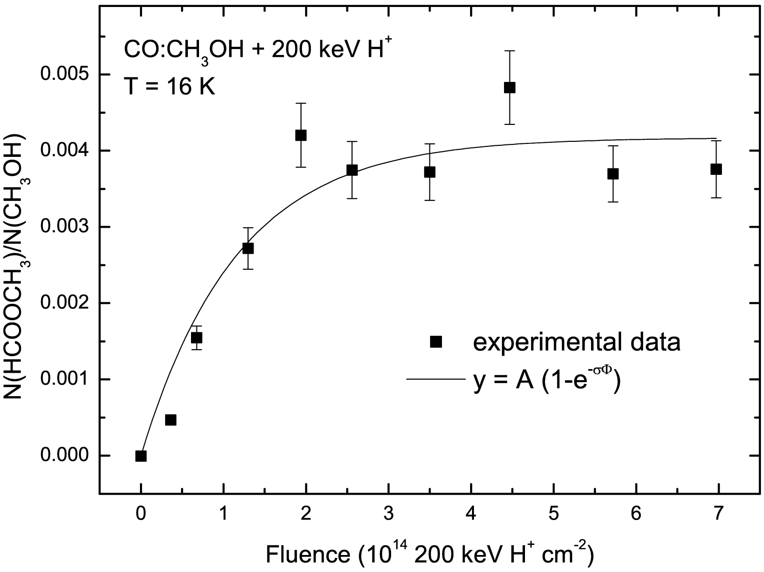

Figure 3.1. The ratio between the column density of methyl formate and methanol, N($HCOOCH_3$)/N(CH_3OH), as a function of ion fluence after irradiation of a CO:CH_3OH mixture at 16 K.

s^{-1} of cosmic ions in the approximation of effective monoenergetic 1 MeV protons (see Mennella et al. 2003). $F_{\rm ISM}$ must be regarded as an effective quantity. It represents the equivalent flux of 1 MeV protons, which gives rise to the ionisation rate produced by the cosmic-ray spectrum if 1 MeV protons were the only source for ionisation. Furthermore, we assume that the cross section scales with the stopping power (S, energy loss per unit path-length) of impinging ions. According to the SRIM code (developed by Ziegler and coworkers in 2008[1]), in the case of protons impinging on a CO:CH_3OH mixture, S (200 keV protons) = 2.9×S (1 MeV protons). We define $\sigma_{\rm ISM}$ = A × σ/2.9 cm^2, where the product A × σ is the initial slope of Equation 3.1. The formation rate of methyl formate is given by

$$R[{\rm s}^{-1}] = \sigma_{\rm ISM}[{\rm cm}^2] \times F_{\rm ISM} \quad [{\rm ions/cm^2 s}]. \tag{3.2}$$

Using $F_{\rm ISM}$ and $\sigma_{\rm ISM}$ as estimated in Equation 3.2, we obtain the formation of methyl formate R = 6.2 × 10^{-18} s^{-1}.

---

[1] `http://www.srim.org`

Table 3.2. Gas phase and solid state routes of methyl formate destruction and formation. For the gas phase reactions involving methyl formate, the parameters α, β and γ are taken from the KIDA database. The last row lists the new experimental path of methyl formate formation on grain surface as investigated by Modica & Palumbo (2010).

R1	R2	P1	P2	P3	α	β	γ
$HCOOCH_3$	H_3^+	H_2	$H_5C_2O_2^+$		4.05×10^{-9}	-0.5	0
$HCOOCH_3$	He^+	He	CH_3	HCO_2^+	3.54×10^{-9}	-0.5	0
$HCOOCH_3$	H_3O^+	H_2O	$H_5C_2O_2^+$		1.81×10^{-9}	-0.5	0
$HCOOCH_3$	HCO^+	CO	$H_5C_2O_2^+$		1.55×10^{-9}	-0.5	0
$HCOOCH_3$	C^+	$COOCH_4^+$	C		2.17×10^{-9}	-0.5	0
$HCOOCH_3$	H^+	$COOCH_4^+$	H		6.90×10^{-9}	-0.5	0
$H_5C_2O_2^+$	e^-	$HCOOCH_3$	H		1.50×10^{-7}	-0.5	0
mCH_3OH	mCO	$mHCOOCH_3$			6.20×10^{-18}	0.0	0

3.2 Chemical modelling

The chemical model is UCL_CHEM, described in more detail in Chapter 2. Summarising, UCL_CHEM is a time and depth dependent gas-grain chemical model which estimates the fractional abundances (with respect to the total number of hydrogen nuclei) of gas and surface species in every environment where molecules are present. For our purpose it is adapted to model low and high-mass star forming regions (both characterised by high temperatures) as well as an example of a cold core.

Before going into the details of the different models for the various astronomical regions, we show how we updated the model to include the new reactions where methyl formate is involved.

3.2.1 A gas phase reaction network for methyl formate formation and loss pathways

Most of the gas phase reactions that occur in the ISM are collected from the UMIST database (Millar et al. 2000a). Due to the failure of gas phase chemistry to reproduce abundances of particular molecules, in the present work a gas-grain reaction network is also taken into account and we focused on methyl formate formation on the grain surface in particular.

Table 3.2 shows the updated gas phase reaction rate coefficients as listed in the most recent KIDA database (Wakelam et al. 2012) as well as the solid state path of formation of methyl formate, taking into account the new experimental rate coefficient for this reaction (see Subsection 3.2.2). Methyl formate is both one of the reactants (R) and one of the products (P); α, β, and γ are the parameters for the rate coefficient. The first six reactions are bimolecular, ion-neutral reactions where an exothermic charge transfer occurs between an ion and a neutral species. The last one is an electronic recombination, in which the recombination of a positive ion and an electron results in the dissociation of the molecule. In both cases, a Kooij formula (a modified version of the Arrhenius equation) is adopted to evaluate the reaction rate (see Equation 3.3):

$$k(T) = \alpha(\frac{T}{300})^{\beta} e^{-\frac{\gamma}{T}}, \tag{3.3}$$

where T is the gas temperature, α is the cosmic-ray ionisation rate, β contains the dipole effect and γ represents the reaction barrier, which for the updated methyl formate reactions is always zero. β includes the enhancement of ion-neutral rate coefficients for cases in which the neutral has a large, permanent electric dipole moment. This effect is evident at low temperatures (10–50 K), where the rate coefficient has a $T^{-\frac{1}{2}}$ dependence as noted by Herbst & Leung (1986).

3.2.2 Methyl formate formation on grain surfaces: the reaction between carbon monoxide and methanol

In the last row of Table 3.2, the surface pathway for the formation of methyl formate is summarised: carbon monoxide is one of the most abundant species in the ISM, which undergoes successive hydrogenations in the presence of a large amount of hydrogen (Fuchs et al. 2009; Watanabe et al. 2007) to form methanol. Hence, CO reacts with CH_3OH, that, after cosmic ion irradiation, produces methyl formate (see Modica & Palumbo 2010). The m before the molecular formula stands for *mantle*, and means the species are in the solid phase.

In our code two-body grain surface reactions are considered to be bimolecular reactions occurring as they would in the gas phase, meaning that the parameter α needs to be in units of volume [cm^3 s^{-1}]. Since from experiments α is in units of time, we introduce in our code a different procedure for evaluating the rate coefficient for the formation of solid methyl formate. In particular, we consider an excess of CO-ice compared to the amount of iced methanol (as in the case of a first-order kinetic) and we scale the rate coefficient value

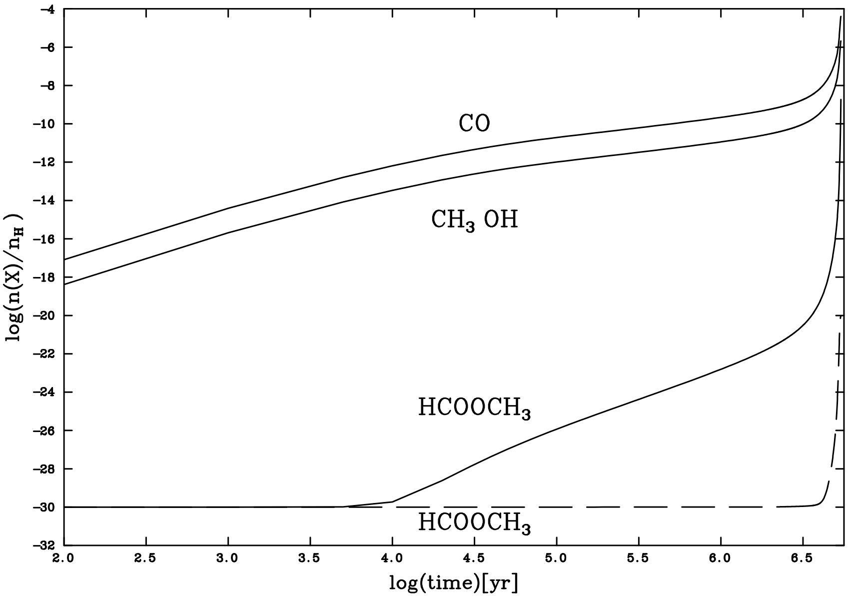

Figure 3.2. Fractional abundances (with respect to the total number of hydrogen nuclei) of selected icy mantle species as a function of time.

for the mantle CO concentration (note that when we use the term *concentration* we refer to the number density of a selected species). The rate constant will therefore depend only on the abundance of methanol on the grain surface. As the amount of mantle CO varies with time, we estimate a different value for the rate of the reaction at each time.

3.3 Methyl formate in various astronomical environments

In order to highlight the effects of the changes that we made in the methyl formate chemistry, we ran a simple model, before and after our updates, that includes a cold as well as a warm-up phase where the non-thermal desorption of species is neglected and the thermal desorption in the warm-up phase is instantaneous.

Figure 3.2 shows the fractional abundances of selected species (from Table 3.2) as a function of time during Phase I. The solid lines represent the abundances of methanol, carbon monoxide and methyl formate when the new solid state route is included in the model. The dashed line is methyl formate obtained from the model computed with the

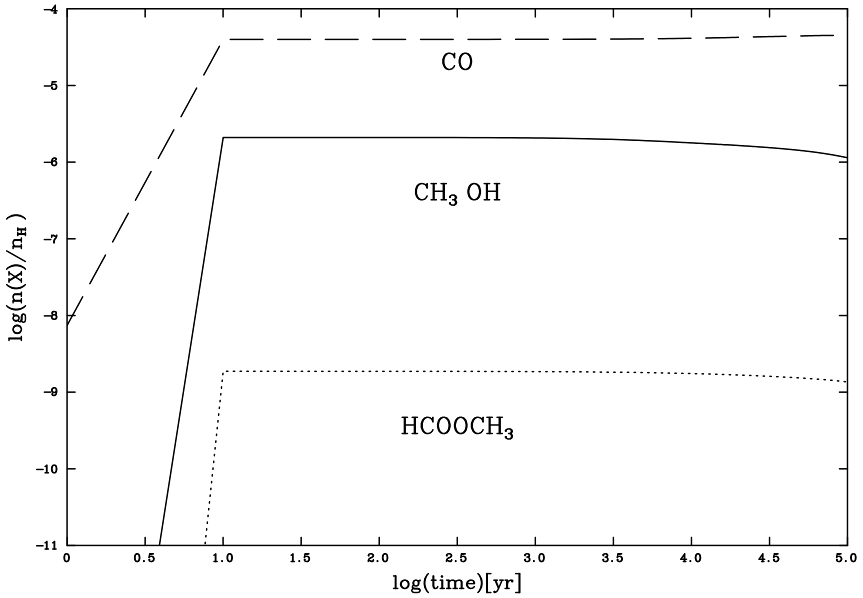

Figure 3.3. Fractional abundances (with respect to the total number of hydrogen nuclei) of selected species as a function of time in the gas phase during Phase II.

same chemistry as in the original code (Viti et al. 2004). In the latter case, the reactant trends are the same as those shown in the updated version of the code. While the reactants, CO and CH_3OH, reach a fractional abundance in the solid state of the order of 10^{-6} and 10^{-8} respectively, methyl formate is produced in a negligible quantity ($\leq 10^{-26}$) onto the grains. By considering the solid state path of methyl formate formation with the experimental rate coefficient of 6.2×10^{-18} s^{-1} (as described in Subsections 3.2.1 and 3.2.2), methyl formate significantly rises in its abundance (solid line). In order to compare our theoretical abundances with those from the observations, we also ran Phase II up to a temperature of 200 K.

Figure 3.3 shows a typical output from our model at the end of the warm-up phase. We only plot the fractional abundances of CO (dashed line), CH_3OH (solid line) and $HCOOCH_3$ (dotted line) in the gas phase obtained after our updates. All the species desorb from the grains at the same time since we set an instantaneous evaporation and their abundances remain fairly constant up to $\sim10^5$ years. As a result, we obtained a detectable abundance of gaseous methyl formate with a value of the order of 10^{-9}.

An alternative route for the synthesis of methyl formate in a hot core was previously investigated by Garrod & Herbst (2006a), that proposed both gas phase and grain surface processes to produce most species during the warm-up phase. They estimated that the gas phase/accretion path, involving protonated methanol and formaldehyde, is responsible for the formation of 25% of the total $HCOOCH_3$ present on the grain surface before sublimation. Indeed, during the warm-up phase, the surface reaction between CH_3O and HCO radicals is allowed and it is thought to be the dominant mechanism; when a significant amount of H_2CO begins to evaporate, the methyl formate formation on the grain surface is inhibited and formaldehyde is protonated to produce methyl formate in the gas phase. They found that these reactions are more efficient in hot corinos than in hot cores due to the different physical conditions; in particular they obtained a peak for the methyl formate fractional abundance of about 10^{-8} at 10^6 years. Considering the high amount of methyl formate produced as output from the the present study and the one from Garrod & Herbst (2006a), both mechanisms seem to be viable as possible explanation of its formation in the ISM.

In order to refine our preliminary results, we qualitatively modelled a few examples of astronomical sources where methyl formate has been detected. In particular, we use the same physical parameters of two high-mass star-forming regions, the Orion Hot Core and the G31.41+0.31; a low-mass source, NGC1333-IRAS2; and the cold gas near the region B1-b in Perseus, using our two-phase UCL_CHEM model. The physical and chemical parameters for each model are listed in Table 3.3, 3.4 and 3.5.

In this revised model for Phase II, we now assume a time-step sublimation instead of an instantaneous evaporation for molecules that sublimate from the grains into the gas phase during the warm-up stage of the star formation process. Specifically, we set methyl formate to co-desorb with water ice at 100 K, based on structural similarities to other molecules such as HCOOCH.

3.3.1 Methyl formate formation in high- and low-mass star-forming regions

Orion KL Hot Core

The Orion Molecular Cloud 1 (OMC1) is a dense clump at a distance of 480 pc that contains several distinct infrared-emitting regions. Among these the Kleinmann-Low (KL)

Table 3.3. Physical parameters of the model (described in Chapter 2) for the Orion KL Hot Core (taken from Lerate et al. 2008) and the G31.41+0.31 (taken from Beltrán et al. 2009).

Parameter	Orion KL Hot Core	G31.41+0.31 HMC
`temp` [K]	10	10
ζ [s^{-1}]	3×10^{-17}	3×10^{-17}
`size` [pc]	0.02	0.05
`dens` [cm^{-3}]	2×10^{2}	2×10^{2}
`df` [cm^{-3}]	1×10^{7}	2×10^{8}
`tfin` [years]	10^{6}	10^{6}
`fr` [%]	98	98
`maxt` [K]	250	300

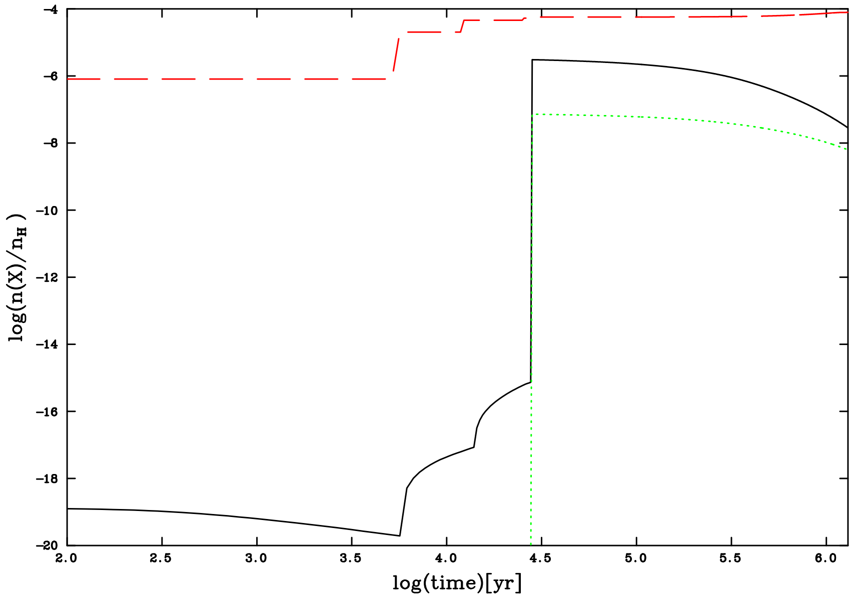

Figure 3.4. Fractional abundances of CO (red dashed line), CH_3OH (black solid line) and $HCOOCH_3$ (green dotted line) in the gas phase at the end of the warm-up phase. The plot is obtained using the physical parameters for the Orion KL Hot Core.

region is composed of four different components: the hot core, the compact ridge, the plateau and the photodissociation region (PDR) surrounding the quiescent gas. While the hot core and the plateau are characterised by elevated temperatures, the ridge consists of an extended and cooler region with quiescent material. We focus on the Orion Hot Core as it is one of the richest known astronomical sources of molecular lines. The main heating mechanism in this location is radiative, and gas kinetic temperatures are close to 200 K. Using UCL_CHEM, Lerate et al. (2008) computed different chemical models to simulate each component of the KL region. In the present work we use the physical and chemical parameters for their best-fitting model reported in Table 3.3.

Our results are displayed in Figure 3.4. The red dashed and the black solid lines refer to CO and CH_3OH respectively; the green dotted line is the trend for methyl formate that sublimates at the same temperature (and therefore at the same time) as methanol, another H_2O-like molecule.

A comparison between our model calculations and the observational column densities through the Orion Hot Core is shown in Table 3.6. Observational data are taken from Remijan et al. (2003), who have surveyed this source with the BIMA Interferometer with an angular resolution of about 2–5″.

G31.41+0.31

G31.41+0.31 is another example of a multiple massive star-formimg region, located at a distance of 7.9 kpc. It is associated with a Hot Molecular Core (HMC) of 0.05 pc in size, where the temperature is found to be about 300 K and the luminosity is about $3\times10^5\ L_\odot$ (Churchwell et al. 1990). It is in fact the region where the simplest sugar, glycolaldehyde (and also one of the isomers of methyl formate), was first detected by Beltrán et al. (2009). The authors also used UCL_CHEM to try to reproduce the abundance of glycolaldehyde. We adopt the physical and chemical input parameters from their study for our model (see Table 3.3).

The resulting plot is displayed in Figure 3.5. The red dashed and black solid lines refer to CO and CH_3OH respectively; methyl formate (green dotted line) shows a similar profile to its fractional abundance in the Orion KL Hot Core model apart from the fact that its final abundance is now lower by about an order of magnitude.

We compare our theoretical results with those given by Cesaroni et al. (1994), who performed high resolution observations of methyl formate by using IRAM Plateau de Bure

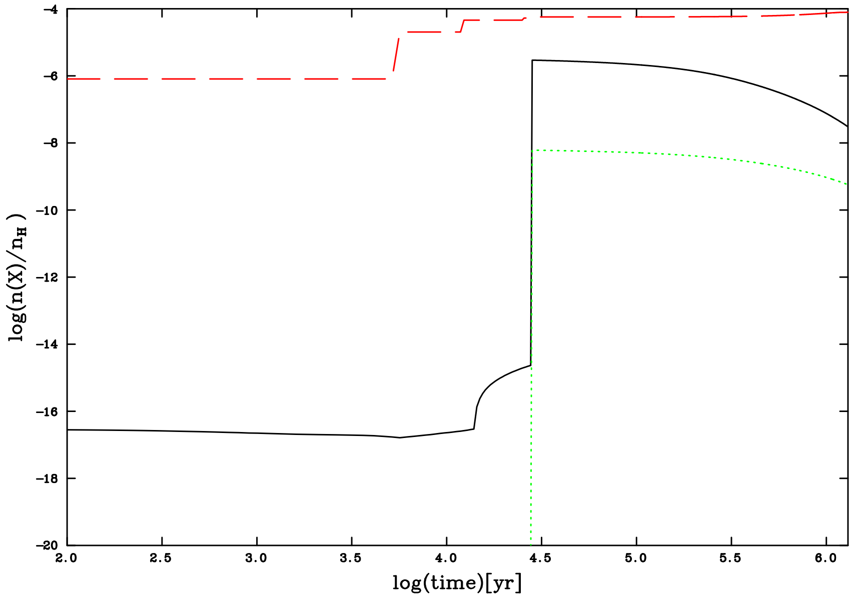

Figure 3.5. Fractional abundances of CO (red dashed line), CH_3OH (black solid line) and $HCOOCH_3$ (green dotted line) in the gas phase at the end of the warm-up phase. The plot is obtained using the physical parameters for the G31.41+0.31.

Interferometer.

NGC 1333-IRAS2

Located in the cloud NGC1333, belonging to the Perseus complex at 220 pc in distance, IRAS2 is a low-mass binary protostellar system, including IRAS2A and IRAS2B, separated by 30″. An infalling envelope, a circumstellar disk and multiple outflows seem to be associated with them. The advantage of observing such nearby objects is that these sources can be spatially resolved with millimetre interferometers.

We therefore adopt a multipoint model in order to reproduce the density profile of the hot corino associated with IRAS2, taken from Maret et al. (2004) (see Figure 3.6). We run 5 different models (see Table 3.4) corresponding to different final densities and sizes of the core evaluated based on Equation 3.4:

$$\log(n) = \log(k) - \alpha \times \log(r) \tag{3.4}$$

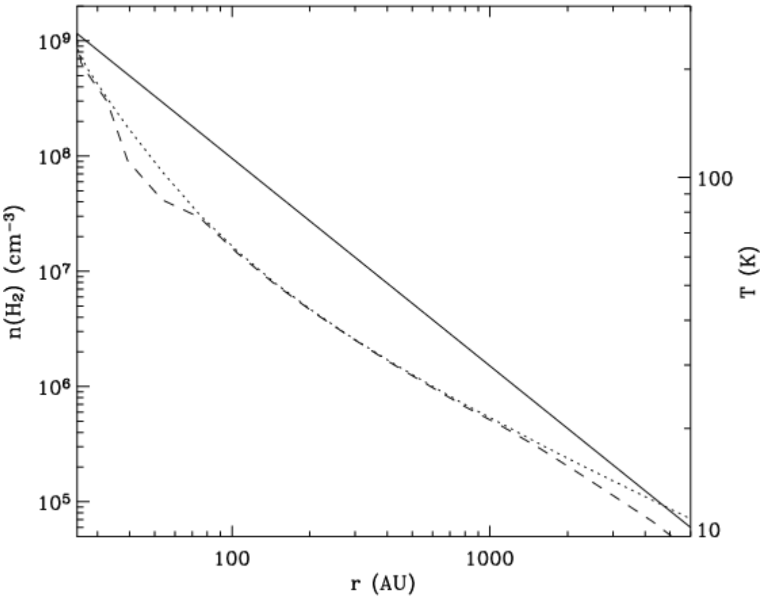

Figure 3.6. Density profile (solid line) of the hot corino associated with IRAS2 taken from Maret et al. (2004). The graph also reports the gas (dashed line) and the dust (dotted line) temperature across the envelope of the source.

Table 3.4. Final densities n and sizes r of the core chosen for each multipoint model as extrapolated by Maret et al. (2004).

Model	n[cm^{-3}]	r[AU]
1	2.8×10^8	50
2	1.0×10^8	100
3	8.9×10^6	500
4	3.2×10^6	1000
5	1.7×10^6	1500

where n is the final density in cm^{-3} and r is the corresponding distance from the centre of the core in AU. Note that the initial density for all models is fixed at a value of 10^2 cm^{-3}. We also used the temperature profile for a hot corino given in Awad et al. (2010) and contained in the Equation 3.5:

$$T_d = 10 + (0.1927 \times t^{0.5339}) \times (r/2.44 \times 10^{15})^{-0.5} \quad \mathrm{K} \tag{3.5}$$

where T_d is the temperature profile of gas and dust in the core surrounding the stellar object, t is the evolutionary age of the collapsing core in years, 0.1927 and 0.5339 are two constants derived from the boundary conditions (t=0 and t= 10^5 years) and r is the core

Table 3.5. Physical parameters of the model (described in Chapter 2) for B1-b core taken from Hirano et al. (1999).

Parameter	Value chosen
`temp` [K]	10
ζ [s^{-1}]	3×10^{-17}
`size` [pc]	0.04
`dens` [cm^{-3}]	2×10^{2}
`df` [cm^{-3}]	1×10^{6}
`tfin` [years]	10^{6}
`fr` [%]	40
`maxt` [K]	30

radius in cm.

We evaluated the total column density for methyl formate as follows:

$$N(\mathrm{HCOOCH_3}) = \sum(X \times A_\mathrm{v} \times r) \times (\mathrm{n(H)} + 2\mathrm{n(H_2)}), \tag{3.6}$$

where X is the methyl formate fractional abundance, A_v is the visual extinction at distance r [pc] from the centre of the core and n(H)+2n(H$_2$) is equal to 1.6×10^{21} cm^{-2} which is the hydrogen column density required to give 1 mag of extinction.

3.3.2 Methyl formate in cold cores

B1-b core

The protostar associated with the B1-b core is believed to be between a pre-stellar and a Class 0 protostar in evolutionary stage. Two sources are identified with the B1-b core, designated as B1-bN and B1-bS, separated by 20″ in the north-south direction at about 350 pc in distance (Hirano et al. 1999). The physical parameters of the two sources are very similar (T_{dust}= 18 K, M= 1.6–1.8 $M_\odot$, L= 2.6–3.1 $L_\odot$). We qualitatively model the B1-b core running our two-phase model with the physical parameters reported in Table 3.5.

For this core, during Phase II the temperature only rises up to 30 K, which implies that only the weakly-bound species partly sublimate due to thermal desorption (see Collings et al. 2004), hence any methyl formate formed on the grains remains in the solid phase. However, non-thermal desorption processes are known to be efficient even at 10 K (see Roberts et al. 2007; Boland & de Jong 1982; Hasegawa & Herbst 1993; Bringa & Johnson 2004). We therefore run Phase I including some non-thermal desorption mechanisms (as

Table 3.6. Observed and predicted column densities towards G31.41+0.31, Orion KL Hot Core, NGC1333-IRAS2 and B1-b core.

Source	Type	D [pc]	$T_{\rm rot}$ [K]	Observed N($HCOOCH_3$)[cm^{-2}]	Modelled N($HCOOCH_3$) [cm^{-2}]
G31.41+0.31 HMC	High mass	7900	300	[2]6.8×10^{18}	9.3×10^{15}
Orion KL Hot Core	High mass	480	250	[1]6.9×10^{16}	3.5×10^{14}
NCG1333-IRAS2	Low mass	220	38	[3]5.8×10^{14}	6.4×10^{12}
B1-b	Dark core	350	<30	[4]8.3×10^{12}	1.2×10^{12}

[1] Remijan et al. (2003)

[2] Note that the total methyl formate abundance reported herein is twice the value of the E-form isomer given in Cesaroni et al. (1994)

[3] Note that the total methyl formate abundance reported herein is twice the value of the A-form isomer given in Bottinelli et al. (2007)

[4] Öberg et al. (2010)

in Roberts et al. 2007). Due to the non-treatment of direct UV- and cosmic-ray induced desorption (see Chapter 2), our computed methyl formate fractional abundances represent only a lower limit.

We compare our results for methyl formate with those reported in Öberg et al. (2010), who observed B1-b with IRAM 30 m telescope in order to identify locations of efficient non-thermal ice desorption.

3.4 Observed and theoretical methyl formate column densities: a comparison

Table 3.6 reports all our model results and compares the theoretical predicted column densities for methyl formate with those observed in the sources described above. It is clear from our theoretical results reported in Table 3.6 that we found a dependence of the methyl formate column densities with the different physical parameters of the astronomical objects chosen: the greater the size of the core the greater the amount of the gaseous methyl formate in the pre-stellar core.

By comparing our calculated column densities with those from the observations (see the fifth column in Table 3.6), a relatively good agreement within a factor of 10 is found for the dark core associated with B1, but the theoretical values are too low for the cases of warmer star-forming regions. In fact around protostars the flux of ions due to stellar flares should also be considered. As discussed by Garozzo et al. (2011), the effects induced by cosmic-rays on icy grain mantles during the collapse phase era are comparable to the effects induced by stellar flare ions during the warm-up phase.

3.5 Conclusions

We have considered one approach to understanding how terrestrial-type organic molecules can be synthesised in cold starless and prestellar cores.

In summary, using the rate coefficient derived from laboratory experiments of the irradiation of ice-analogues, we investigated the viability of a cold solid state path to form methyl formate during the evolution of protostellar cores when the temperatures are low (10 K). We find that we cannot reproduce the abundance of methyl formate found in hot cores and hot corinos without invoking gas or solid phase reactions which necessitate high temperatures (and that can therefore only occur during the warm-up phase once the star is formed), while we were able to reproduce the observed abundances in cold cores. Photodissociation or particle bombardment processes can in fact cause temporary non-thermal motions of species so as to promote the rates of non-thermal diffusive reactions (Kim & Kaiser 2012).

This work supports the idea that cosmic ion irradiation of icy grain mantles may be able to contribute to the production of the methyl formate observed in dense molecular clouds, but that other routes of formation are also required.

Chapter 4

Modelling of ethylene oxide formation on grain surfaces

The work presented in this Chapter is based on the paper by Occhiogrosso et al. (2012) in collaboration with S. Viti, M. D. Ward and S. D. Price.

This chapter focuses on another important complex organic molecule, ethylene oxide, which it is thought to form mainly on the grain surface.

Ethylene oxide (c-C_2H_4O) is the simplest epoxide, a ring-shaped organic compound involving an oxygen atom bonded to two carbon atoms. Since it is believed to lead to the synthesis of amino acids (Ehrenfreund & Cleaves 2003) and hence potentially influence early pre-biotic pathways (Miller & Singer 1993), c-C_2H_4O may play an important role in the ISM.

First detected towards the Sgr B2N molecular cloud, associated with 10 rotational transitions (in the 79–116 GHz and 218–264 GHz, Dickens et al. 1997), this molecule has been investigated in a more extended frequency range (662 lines between 262–358 GHz, Pan et al. 1998) and more recently Bernstein & Lynch (2009) attributed the unidentified IR band features discovered by Gillett & Forrest (1973) to ethylene oxide and to another small carbonaceous molecule, cyclopropenylidene. Ikeda et al. (2001) estimated c-C_2H_4O fractional abundances by observing 20 massive star-forming regions and two dark clouds.

In fact, ethylene oxide was detected towards 10 of these sources but it was not found in the TMC-1 and TMC-1(NH_3) dark clouds, in contrast to one of its isomers, acetaldehyde (CH_3CHO) which seems to be ubiquitous.

A gas phase pathway for the formation of ethylene oxide has been proposed by Turner & Apponi (2001), who suggested the reaction chain to produce c-C_2H_4O and one of its isomers, vinyl alcohol (CH_2CHOH), starting with the interaction between $CH_3{}^+$ and H_2CO; unfortunately, they failed in the attempt of observing the intermediates of this reaction in the ISM.

Ikeda et al. (2001) investigated the relationship between c-C_2H_4O abundances and the dust temperature, but without finding any correlation. On the other hand, evidence of a correlation between the column densities of all the C_2H_4O isomers and ethanol identified the latter as a possible precursor of ethylene oxide and its isomers. Indeed, a gas phase pathway for ethylene oxide formation has been proposed (Dickens et al. 1997) with ethanol as one of the reactants:

$$\mathrm{CH_3^+ + C_2H_5OH} \longrightarrow \mathrm{C_2H_5O^+ + CH_4} \tag{4.1}$$

$$\mathrm{C_2H_5O^+ + e^-} \longrightarrow \mathrm{C_2H_4O + H} \tag{4.2}$$

where the formula C_2H_4O does not distinguish among the different isomers. However, by following the chemical evolution of c-C_2H_4O at different temperatures and volume densities, Ikeda et al. (2001) found that this molecule did not form in warm gas. The results of Ikeda et al. (2001) suggested that other reactions such as grain surface reactions may be important for the synthesis of ethylene oxide.

Hudson & Moore (2003) experimentally investigated a solid state route for the formation of CH_2CHOH involving exposure of H_2O:C_2H_2 ices to protons and photons, but the first proposed surface scheme for ethylene oxide formation dates back to the simulation by Charnley (2004) who identified acetaldehyde (CH_3CHO) as a possible precursor.

The contribution of grain surface reactions to the production of the three isomers with formula C_2H_4O has also been investigated by Bennett et al. (2005): they presented the results of electron irradiation on a mix of carbon dioxide and ethylene ice, under interstellar and cometary conditions, to highlight the effect of non-thermal processing of ices. The experimental abundance ratios among the three isomers, acetaldehyde, ethylene oxide and vinyl alcohol, seem to be very uncertain (Bennett et al. 2005), but generally

CH_3CHO was found to be the most abundant and CH_2CHOH was determined to have a lower abundance than ethylene oxide. This relationship can be explained in the light of the fact that the formation of ethylene oxide occurs via direct addition of the oxygen across the C=C double bond of ethylene, while vinyl alcohol requires the insertion of an oxygen into the C–H bond.

Recently, an alternative solid state pathway for the formation of ethylene oxide has been investigated by Ward & Price (2011) who studied the surface reactivity between C_2H_4 and thermal O atoms under astrophysically relevant conditions. They co-deposited the reactants on a graphite surface at various temperatures in the 12–90 K range. In order to identify the products formed, they recorded desorption spectra and they also selectively ionised the three different isomers with a tunable dye laser. Finally, they performed a similar laboratory study with C_3H_6 as reactant, but unfortunately although C_3H_6O was observed they were unable to identify the isomeric products of the reaction due to the large number of possible molecules with formula C_3H_6O. Despite these limitations, the authors assumed that the majority of the C_3H_6O formed is propylene oxide, c-C_3H_6O, by following the same mechanism as for the case of ethylene oxide production. Unlike c-C_2H_4O, c-C_3H_6O has not yet been detected in the ISM since it is believed to isomerise to propanal (CH_3CH_2CHO) or acetone (CH_3COCH_3), which have both been observed in the ISM (Hollis et al. 2004; Combes et al. 1987; Snyder et al. 2002).

To date, the observed abundances of ethylene oxide have not yet been reproduced by chemical models; in fact, to our knowledge, none of the grain surface pathways for the formation of ethylene oxide have been included in the models that simulate the star formation process.

In this study, we update the UCL_CHEM gas-grain chemical model with the reaction rates for the production of ethylene oxide as evaluated by Ward & Price (2011). By following the same logic as these authors, we extended our study to include the formation of propylene oxide in order to verify whether C_3H_6O can be produced under ISM conditions even without having any observational evidence of its presence in interstellar space. The content is organised as follows: Section 4.1 gives details of the model; Section 4.2 considers the astronomical implications of our study; Section 4.3 contains a discussion of our results and it also shows a comparison between our theoretical column densities and those taken from the observations. Finally, we give our conclusions in Section 4.4.

Table 4.1. Surface reactions investigated by Ward & Price (2011), with estimate rate coefficients at 20 K.

Reaction	α [cm^2 mol^{-1} s^{-1}]
mO + mC_2H_4 → mc-C_2H_4O	1.20×10^{-19}
mO + mC_3H_6 → mc-C_3H_6O	3.40×10^{-19}

The m before the molecular formula stands for *mantle*

4.1 Astrochemical interpretation of laboratory data

For the purpose of the present work we extend the UCL_CHEM surface reaction file to include the formation of c-C_2H_4O and c-C_3H_6O on the grain surface as investigated by Ward & Price (2011 ,see Table 4.1). In order to analyse their data, these authors developed a simple kinetic model in which molecules can react via Eley-Rideal (ER) or Langmuir-Hinshelwood (LH) mechanisms (see Chapter 1). In the latter case, both reactants adsorb and thermalize on the surface before a diffusion reaction occurs. In our model, we consider the reactions to occur via the LH mechanism, which seems of greater astrophysical relevance as stated by Awad et al. (2005) and by the authors themselves.

Since our code accounts for reactions that occur in three dimensions (i.e. gas phase reactions), we need to transform the surface rate constants of Ward and Price discussed above. Therefore we first evaluate two quantities: the volume of ice per grain (V_{ice}) and the number density of the grains (n_g). In order to estimate the volume of ice we consider the grains to be spheres and we assume a thick ice layer of 0.3 μm (Collings et al. 2003). V_{ice} is therefore equal to 2.6×10^{-13} cm^3. In order to calculate the number density of the grains we assume a dust/gas mass ratio of 0.01 and we solve the following equation:

$$M_d = 0.01 M_g, \tag{4.3}$$

where M_d and M_g are the total mass of dust and gas respectively. M_d can be expressed in turn as the product of the grain number density and the mass of a dust particle. The latter quantity is equal to $\sim1.5\times10^{-14}$ g, obtained assuming the volume of a sphere of 10^{-5} cm in radius and a density of 3.5 g cm^{-3} (Williams & Herbst 2002; Weingartner & Draine 2001). In order to evaluate M_g, we consider a number density of the order of 10^7 cm^{-3} (typical of a hot core source) and the mass of a proton. Thus, we obtain a grain number density of 3.8×10^{-5} cm^{-3}. The product of the grain number density and the volume of ice represents the number of cm^3 of ice in 1 cm^3 of space (1×10^{-17} cm$^3{}_{ice}$ cm$^{-3}{}_{space}$).

Since we consider our reactions to be taking place in one monolayer (ML), we can write the units for concentration as cm^{-2} ML^{-1}, giving the rate constant in units of cm^{2} ML s^{-1}. Assuming one ML has a height of 5 Å, we obtain 2×10^{7} ML s in 1 cm. By dividing our rate constants (reported in Table 4.1) by the latter quantity, we calculate a rate constant of 6.0×10^{-27} cm^{3} s^{-1} for the formation of ethylene oxide and a rate constant of 1.7×10^{-26} cm^{3} s^{-1} for the production of propylene oxide. We finally convert our new rate constants per cm^{3} of ice to cm^{3} of space given by the ratio:

$$\frac{6 \times 10^{-27} cm^3_{ice} s^{-1}}{1 \times 10^{-17} cm^3_{ice} cm^{-3}_{space}}$$

Since the major component of the ice mixture is water we also account for the fraction of C_2H_4 or C_3H_6 ice compared to water ice in order to avoid overestimating our rates. We consider that not all the oxygen ice will react with the ethylene or propene ice because of the presence of other ice components. We hence estimate a final value of 6×10^{-15} cm^{3} s^{-1} at 20 K for the reaction between O and C_2H_4 and a rate of 5×10^{-14} cm^{3} s^{-1} at 20 K for the reaction between O and C_3H_6 onto the grains. In order to determine the contribution of these rates to the abundance of c-C_2H_4O and c-C_3H_6O in the ISM, we initially did not include any gas phase pathway for the formation of these species.

The percentage of depletion of oxygen atoms on the grains is certainly one of the critical parameters in the formation of ethylene and propylene oxide: Caux et al. (1999) found that the fractional abundance of oxygen (relative to hydrogen nuclei) on the grains is of the order of 10^{-6} and this amount depends on the percentage of the oxygen that is depleted in the dense, cold cores. In our model, oxygen freezes on the grains in the form of H_2O, O and OH. It is known that oxygen containing species in interstellar ices consist mainly of H_2O and also that the fractional abundances of water ice (relative to the total number of hydrogen nuclei) are of the order of 10^{-4} (Caux et al. 1999); we vary the percentage contribution of each channel by which oxygen containing species accumulate on the grains by varying the efficiency of the different oxygen accretion pathways as shown in Table 4.2. Since we find that 1% of oxygen atoms in the ice (mO) is already sufficient for the observational values of water ice to be satisfied, we subsequently use this percentage for our models.

Figure 4.1 shows the fractional abundances of our selected species as a function of time at the end of Phase I; we run a simple model for a core of 0.03 pc in size, with a final density

Table 4.2. List of test chemical models to investigate the minimum percentage of oxigen needed in order to produce ethylene oxide on the grain surface.

Test	mH_2O (%)	mO (%)	mOH (%)
1	99.5	0.5	0
2	90	1	9
3	90	2	8
4	90	5	5
5	90	10	0
6	80	20	0
7	70	15	15

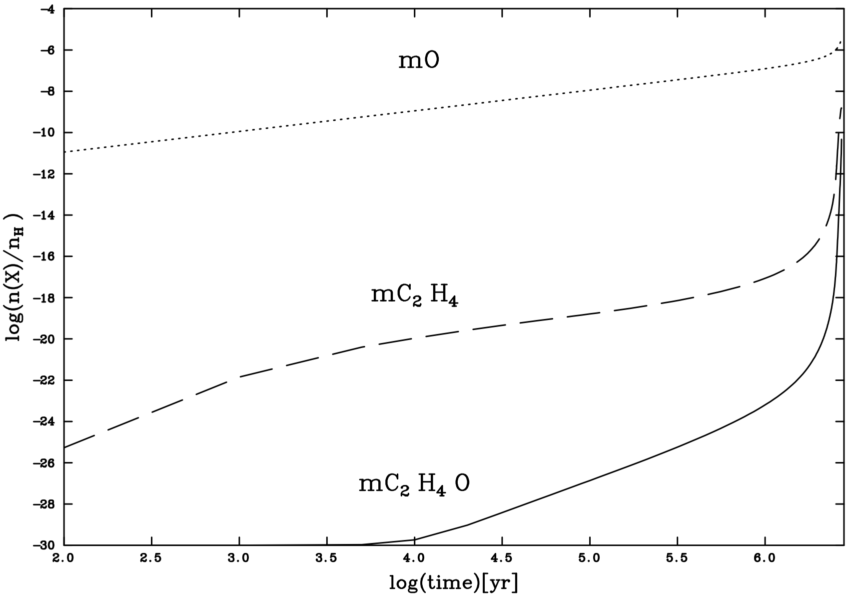

Figure 4.1. Grain surface formation of selected species during Phase I. The fractional abundances (with respect to the total number of hydrogen nuclei) vary along with the time.

of 10^7 cm^{-3} at 10 K, and under standard cosmic-ray ionization field ($\zeta_0 = 1.3\times10^{-17}$ s^{-1}). During this phase atoms and molecules freeze onto the grains and surface reactions can occur due to the catalytic effects of the icy mantles. The dotted and dashed lines refer to the reactants, atomic oxygen and ethylene respectively; the solid line shows the ethylene oxide formation. Note that the fractional abundance of ethylene at the beginning of Phase I is low since it also mainly forms on the grains. We mostly focus on ethylene oxide because results show that c-C_3H_6O is produced below the threshold of detection; this fact may mean that this molecule is not detectable in the ISM although we stress that we do not have a complete network of reactions (both in the gas phase and on the grain surfaces) for c-C_3H_6O and its precursors. Since we obtain a fractional abundance of solid ethylene oxide of the order of 10^{-10}, we conclude that the reaction between oxygen and ethylene on grains with a reaction rate of 6×10^{-15} cm^3 s^{-1} (evaluated as described above) may be the main formation path for c-C_2H_4O.

In order to compare our theoretical results with observations we ran further models where gas phase reactions were included, despite the fact that the routes proposed to date (as mentioned in the introduction to this Chapter) do not distinguish among the different isomers of formula C_2H_4O. We then include in our model the gas phase routes of formation for c-C_2H_4O listed in Table 4.3. We insert the C_2H_4O species into our database with the reaction rates taken from the OSU database (see Chapter 1). Since the literature does not distinguish among the different isomers, we assume the ratios of 2:1.5:1 (as reported by Ikeda et al. 2001) for acetaldehyde, ethylene oxide and vinyl alcohol respectively to evaluate the rate of formation of each product. The different paths listed in Table 4.3 are mostly two-body reactions. Specifically we have charge exchange and ion-neutral reactions, electronic recombination of positive ions with electrons followed by the dissociation of the resulting molecule (dissociative attachment) and finally photo-processes where the dissociation or ionisation of neutral species is performed by UV photons from a standard interstellar UV field. In the latter case, the reaction rates depend on the visual extinction of the source so we do not expect the reaction to be efficient at the high visual extinction of hot cores and hot corinos.

Before testing the sensitivity of the c-C_2H_4O abundances to the different physical conditions of potential astronomical sources, we investigate another important parameter for the formation of ethylene oxide: the amount of C_2H_4 available on the grain surfaces. Despite the fact that C_2H_4-ice has not been detected to date, several experiments have

Table 4.3. Gas phase paths of c-C_2H_4O formation and destruction. The rates are taken from the OSU database and they have been scaled by considering the ratio 2:1.5:1 as in Ikeda et al. (2001). R indicates a reactant, P a product.

R1	R2	P1	P2	P3	k [cm^3 s^{-1}]
C^+	C_2H_4O	$C_2H_3O^+$	CH		7.3×10^{-9}
C^+	C_2H_4O	$C_2H_4O^+$	C		7.3×10^{-9}
H^+	C_2H_4O	$C_2H_3O^+$	H_2		2.2×10^{-10}
H^+	C_2H_4O	$C_2H_4O^+$	H		2.2×10^{-10}
He^+	C_2H_4O	HCO^+	CH_3	He	6.1×10^{-9}
He^+	C_2H_4O	$CH_3{}^+$	HCO	He	6.1×10^{-9}
He^+	C_2H_4O	$C_2H_2O^+$	H_2	He	6.1×10^{-9}
He^+	C_2H_4O	$C_2H_3O^+$	H	He	6.1×10^{-9}
He^+	C_2H_5OH	$C_2H_3O^+$	H_2		2.9×10^{-9}
$S_2{}^+$	C_2H_5OH	$H_2S_2{}^+$	C_2H_4O		6.4×10^{-11}
$H_3{}^+$	C_2H_4O	$C_2H_5O^+$	H_2		2.7×10^{-8}
HCO^+	C_2H_4O	$C_2H_5O^+$	CO		1.1×10^{-8}
H_3O^+	C_2H_4O	$C_2H_5O^+$	H_2O		1.2×10^{-8}
O	$C_2H_5{}^+$	$C_2H_4O^+$	H		7.5×10^{-11}
$CH_3{}^+$	C_2H_4O	$C_3H_6OH^+$			4.3×10^{-10}
e^-	$C_2H_4O^+$	CH_3	HCO		6.5×10^{-7}
e^-	$C_2H_4O^+$	C_2H_2O	H	H	6.5×10^{-7}
e^-	$C_2H_4O^+$	C_2H_2O	H_2		6.5×10^{-7}
e^-	$C_2H_5O^+$	C_2H_4O	H		6.5×10^{-7}
e^-	$C_2H_5OH^+$	C_2H_4O	H_2		6.5×10^{-7}
e^-	$C_2H_5OH_2{}^+$	C_2H_4O	H_2	H	6.5×10^{-7}
e^-	$C_2H_6CO^+$	C_2H_4O	CH_2		6.5×10^{-7}
e^-	$C_3H_6OH^+$	C_2H_4O	CH_3		6.5×10^{-7}
C_2H_4O	photon	CH_3	HCO		2.2×10^{-10}
C_2H_4O	photon	CH_4	CO		2.2×10^{-10}
C_2H_4O	photon	$C_2H_4O^+$	e^-		1.5×10^{-10}

looked at its formation on grains under physical conditions relevant for the interstellar medium (Hiraoka et al. 2000; Kaiser & Roessler 1998; Baratta et al. 2003; Bennett et al. 2006). Using different experimental techniques, C_2H_4 was observed as a product following irradiation of CH_4-containing icy mixtures and it was also predicted to be an intermediate in the hydrogenation of C_2H_2 (Kaiser & Roessler 1998; Bennett et al. 2006). In these cases, ethylene formation competes with the formation of C_2H_6, which was found to be the most abundant molecule in the product mixture. In our model we include the hydrogenation of C_2H_2 on grains in Phase I to form C_2H_4 as well as C_2H_6 (see Table 4.4).

Based on the experimental studies performed to date (Baratta et al. 2003), each time C_2H_6 is produced, a small experimental signature that has been assigned to icy ethylene

Table 4.4. The main hydrogenation pathways for C_2H_2, C_2H_4, C_2H_6 on grain surfaces.

	Reaction	BRs [%]
1	$C_2H_2 \rightarrow mC_2H_2$	10
2	$C_2H_2 \rightarrow mC_2H_4$	40–1
3	$C_2H_2 \rightarrow mC_2H_6$	50–89
4	$C_2H_4 \rightarrow mC_2H_4$	10–1
5	$C_2H_4 \rightarrow mC_2H_6$	90–99
6	$C_2H_6 \rightarrow mC_2H_6$	100

can also be observed; it is therefore appropriate to investigate the minimum amount of ethylene on grains necessary to reproduce the relevant c-C_2H_4O observations. In a similar manner as described above for the case of oxygen, we vary the branching ratios for the different channels involved in the relevant hydrogenation pathways (see Table 4.4) in order to determine the minimum concentration of C_2H_4 on grains needed for the formation of ethylene oxide. As shown in Table 4.4, we investigate the variation of the branching of C_2H_2 hydrogenation to mC_2H_4 (m denotes a molecule in an icy mantle) between 1% and 40% and we obtain mC_2H_4 fractional abundances (relative to the total hydrogen nuclei) of 9.31×10^{-11} and 2.53×10^{-9}, respectively. We find that the lower abundance of mC_2H_4 still generates viable quantities of c-C_2H_4O and so we fix the branching of reaction 2 to 1% in all further studies. We then investigate the effect of the role of accretion of gas phase C_2H_4 to form mC_2H_4, a process which competes with hydrogenation of C_2H_4 to yield mC_2H_6 (reaction 4 and 5, Table 4.4). Here we find that a branching of only 1% in the direction of mC_2H_4 still results in a c-C_2H_4O abundance in agreement with observations.

In summary, the above investigations of the hydrogenation pathways showed that a branching of only 1% towards both reactions 1 and 4 in Table 4.4 yields c-C_2H_4O column densities (3.9×10^{12} cm^{-2}) comparable (within one or two orders of magnitude) with their observed values that range between 10^{13} and 10^{14} cm^{-2} among different hot core sources (see Section 4.3). These branching ratios are therefore used in all further modelling. In the next Section, we qualitatively model a sample of high-mass star-forming regions by looking at the influence of the physical parameters on the ethylene oxide abundances.

4.2 Astronomical implications

Based on the study by Ikeda et al. (2001), ethylene oxide has been detected towards the Orion compact ridge and several hot cores. We qualitatively model these regions with UCL_CHEM by varying the final sizes and densities of Phase I and the temperatures in Phase II. In Phase I non-thermal desorption is included as in Roberts et al. (2007). During Phase II icy mantles sublimate as in Viti et al. (2004). In the present work, we consider c-C_2H_4O as H_2O-like (it will co-desorb when the H_2O-ice desorbs) based on the fact that in the Ward & Price (2011) experiments, its desorption profile shows only one peak (as for the water desorption profile) and its dipole moment is big enough to assume that this species will have a lower desorption energy from the surface (in that specific case, graphite) than from itself. An alternative model, based on different considerations regarding ethylene oxide desorption, is described in Chapter 5. In our model the temperature of the gas is derived as a function of the luminosity (and therefore the age) of the accreting protostar through a simple power law (see Equation 2.1 in Chapter 2).

In order to investigate the sensitivity of the chemistry to the physical parameters of dense cores we run a grid of 16 chemical models by varying: (i) the size of the core, (ii) the final density of the collapsing core, (iii) the temperature in Phase II, (iv) the adsorption energy (controlled by ϵ, explained later in the present Section) and (v) the percentage of the species accreted onto the grain surfaces. Table 4.5 lists the different models and the c-C_2H_4O fractional abundances (X) (relative to hydrogen nuclei) obtained as outputs (see the last column). We also derive the column density (N) by using the formula below:

$$N(\mathrm{c-C_2H_4O}) = X \times A_\mathrm{v} \times (n(H) + 2n(H_2)), \tag{4.4}$$

where X is the ethylene oxide fractional abundance, A_v is the visual extinction and $n(H)+2n(H_2)$ is equal to 1.6×10^{21} cm^{-2} which is the hydrogen column density that gives 1 mag of extinction.

4.2.1 Sensitivity to variation in the density, temperature and core size

Models M1 to M10 simulate the typical physical parameters for an hot core model (as described in Lerate et al. 2008), that span a range of 2×10^7–2×10^8 cm^{-3} in density, 200–300 K in temperature and 0.02–0.04 pc in size. Models M11–M16 best represent the

Table 4.5. List of chemical models and their parameters: `size`, density (`df`), gas temperature (T) during Phase II, threshold adsorption energy (ϵ), efficiency of the freeze-out (`fr`) during Phase I, the percentage of mantle CO (mCO) given by the freeze-out parameter at the end of Phase I of the chemical model. The last column lists the c-C_2H_4O theoretical fractional abundances (X) (relative to the total number of hydrogen nuclei) obtained as outputs from each model. We also report its calculated column densities (N) at 10^6 years. Note that we consider a star of 25 $M_\odot$ in all the simulations.

	`size` [pc]	`df` [cm^{-3}]	T [K]	ϵ	`fr`	mCO [%]	N [cm^{-2}]	X
M1	0.02	$2{\times}10^8$	300	0.1	0.3	98	$1.1{\times}10^{13}$	$1.8{\times}10^{-11}$
M2	0.02	$2{\times}10^8$	300	0.01	0.3	98	$6.2{\times}10^{12}$	$1.0{\times}10^{-11}$
M3	0.02	$2{\times}10^8$	300	0.1	0.0075	75	$1.1{\times}10^{12}$	$1.8{\times}10^{-12}$
M4	0.02	$2{\times}10^8$	300	0.01	0.0075	75	$1.1{\times}10^{12}$	$1.7{\times}10^{-12}$
M5	0.02	$2{\times}10^7$	200	0.1	0.3	98	$6.8{\times}10^{12}$	$1.1{\times}10^{-11}$
M6	0.02	$2{\times}10^7$	200	0.01	0.3	98	$3.9{\times}10^{12}$	$6.4{\times}10^{-12}$
M7	0.02	$2{\times}10^7$	200	0.1	0.0075	75	$6.2{\times}10^{13}$	$1.0{\times}10^{-10}$
M8	0.02	$2{\times}10^7$	200	0.01	0.0075	75	$6.1{\times}10^{13}$	$9.9{\times}10^{-11}$
M9	0.04	$2{\times}10^8$	300	0.1	0.3	98	$2.2{\times}10^{13}$	$1.8{\times}10^{-11}$
M10	0.04	$2{\times}10^7$	200	0.1	0.3	98	$1.5{\times}10^{13}$	$1.2{\times}10^{-11}$
M11	0.06	$2{\times}10^6$	80	0.1	0.5	98	$2.7{\times}10^{14}$	$1.5{\times}10^{-10}$
M12	0.06	$2{\times}10^6$	80	0.01	0.5	98	$1.5{\times}10^{14}$	$8.1{\times}10^{-11}$
M13	0.06	$2{\times}10^6$	80	0.1	0.25	98	$1.5{\times}10^{14}$	$8.1{\times}10^{-11}$
M13	0.06	$2{\times}10^6$	80	0.1	0.25	75	$1.5{\times}10^{14}$	$8.1{\times}10^{-11}$
M14	0.06	$2{\times}10^6$	80	0.01	0.25	75	$1.6{\times}10^{14}$	$8.7{\times}10^{-11}$
M15	0.06	$2{\times}10^6$	80	0.1	0.1	40	$6.8{\times}10^{14}$	$3.7{\times}10^{-10}$
M16	0.06	$2{\times}10^6$	80	0.01	0.1	40	$6.4{\times}10^{14}$	$3.5{\times}10^{-10}$

characteristics for a compact ridge, where we set a temperature of 80 K in order to look at the molecular abundances when the water desorption has not yet occurred; the density is set at a fixed value of $2{\times}10^6$ cm^{-3} for a core size of 0.06 pc. A complete list of the physical parameters chosen in each simulation is reported in Table 4.5. We consider a star of 25 $M_\odot$, characterised by a visual extinction of about 300–500 mags. We then vary the density of the core (`df`) in the 10^6–10^8 cm^{-3} range and we also modify the temperature (T) according to the observations towards the different astronomical sources, even if for T $\geq$100 K we do not expect any influence of this parameter since, as already explained, the sublimation of ethylene oxide occurs simultaneously with the water desorption (at around 100 K).

If we compare, for instance, M1 and M5, no notable differences in the column densities can be found: with increasing density the values are slightly higher as expected from the faster chemistry in a denser medium. On the other hand, keeping all the other parameters

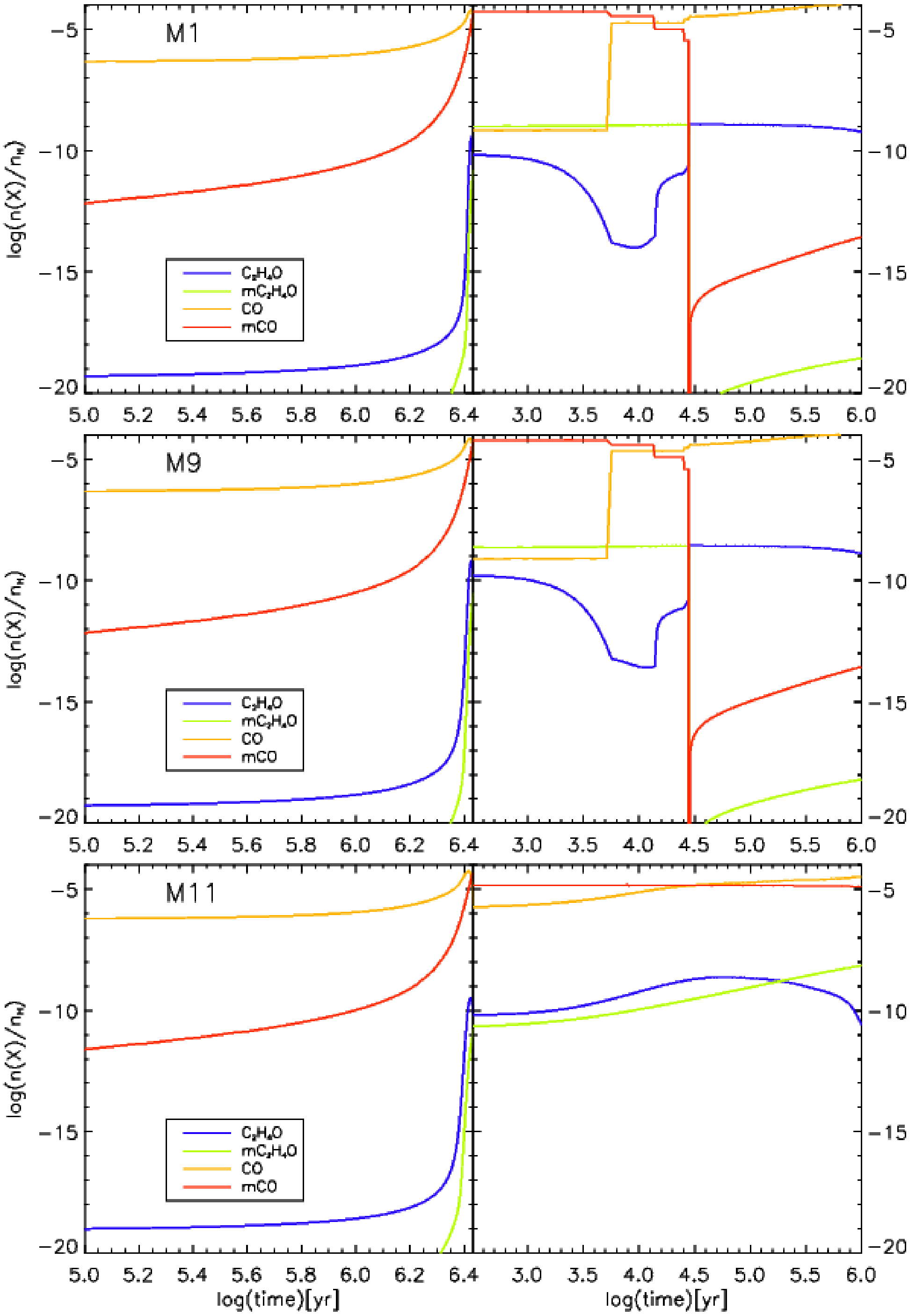

Figure 4.2. Outputs from models M1, M9, M11 (from the top to the bottom) during Phase I (left panel) and Phase II (right panel). The fractional abundances of ethylene oxide in the gas phase and on the grain surface (m stands for *mantle*) are reported as a function of the time. The trends for CO are also shown as a reference.

unchanged, the core size may influence the abundances of c-C_2H_4O.

Figure 4.2 compares the outputs from models M1, M9 and M11 (moving from the top to the bottom) during Phase I (left panels) and Phase II (right panels). In particular, we show the trends for ethylene oxide both in the gas phase (C_2H_4O) and on the grain surface (mC_2H_4O, where m stands for *mantle*); we also plot the fractional abundance of gaseous and solid CO as a reference. We found that the combined effect of the changes in the size and in the density of the core influences the estimated etylene oxide coloumn densities. In particular, c-C_2H_4O column density calculated from the output of M9 is double the value obtained for M1 (in the latter case, we in fact consider a core that is half the size of the one in M9); the differences in the ethylene oxide coloumn densities can vary up to one order of magnitude if we compare M1 or M9 with M11.

4.2.2 Sensitivity to variation in the percentage of the accreted species onto the grain surfaces

Based on the study by Roberts et al. (2007), we introduce three non-thermal desorption mechanisms during the cold phase of our model (Phase I). Specifically, desorption resulting from: H_2 formation on grains, direct cosmic-ray heating and cosmic-ray-induced photodesorption. All three non-thermal desorption processes are found to be very significant in dark cloud conditions where temperatures are too low for thermal desorption to be significant.

In particular, as mentioned in Section 1.3.2, the surface formation of molecular hydrogen releases an energy of around 4.5 eV, capable of inducing thermal desorption of molecules from the grains. This is a selective process which involves mainly the most volatile species.

Cosmic-ray-induced photodesorption is also a selective process that accounts for the number of molecules released to the gas phase after each cosmic-ray impact. These cosmic-rays are able to ionise and excite the surrounding gas, resulting in the emission of a UV photon, even where the visual extinction is high enough to extinguish any UV radiation propagating in from the outside of the cloud. This internal UV flux impinges on the grain surfaces and dissociates the absorbed molecules (mainly H_2O). As for the case of H_2 formation, molecules desorb due to energy released by recombination of OH and O; this type of desorption is non-selective.

Finally, direct cosmic-rays are an efficient heating source able to penetrate deeply into molecular clouds; indeed when these energetic particles impact on the grains, molecules (adsorbed on the surfaces) start to desorb because of the energy transfer from the cosmic-rays to the icy mantles.

The efficiency of the non-thermal desorption of molecules depends on the percentage of the accreted species on the grain surfaces, which is in turn linked to the rate of freeze-out. The latter quantity is a free parameter in our models, controlled by the product of the sticking coefficient and the average grain surface area. We vary the efficiency of freeze out, `fr`, in order to obtain different percentages of solid CO within a range of 75–98% for the hot core models and 40–98% for the compact ridge model. Specifically, the percentage of CO that freezes onto the grain surface is given by solving the formula:

$$\frac{mCO}{mCO + CO} \times 100\%. \tag{4.5}$$

Finally, we investigate the effects of varying the adsorption energy that is controlled by the ϵ parameter. The latter is defined as the number of species removed each time an H_2 molecule is formed. The value of ϵ is uncertain and may be greater than 1, but, as stated in Roberts et al. (2007), at large values, the desorption will be so efficient as to prevent the build-up of any mantle material until very late times. This justifies the choice of small values for ϵ, 0.01 and 0.1, in order to look at the effect of this free parameter on the desorption rates. As shown in Table 4.5, the column densities are slightly higher when the H_2 formation becomes the dominant non-thermal desorption mechanism ($\epsilon = 0.1$).

In general, we find that all the changes made to the physical parameters (see Table 4.5) produce fluctuations of the estimated ethylene oxide column densities within two orders of magnitude; indeed our theoretical column densities are in the 10^{12}–10^{14} cm^{-2} range for all models. This may seem surprising for the case of the compact ridge models since at 80 K (the temperature adopted for these models) the co-desorption of molecules with water has not yet occurred. The constancy of the column density of ethylene oxide may reflect the fact that non-thermal and thermal desorption provide the same contribution to the molecular abundances, but under different physical conditions. Specifically, the chemistry of denser, but smaller regions is mostly influenced by high temperatures. However, in low density, but more extended sources, the chemistry is driven mainly by non-thermal desorption phenomena.

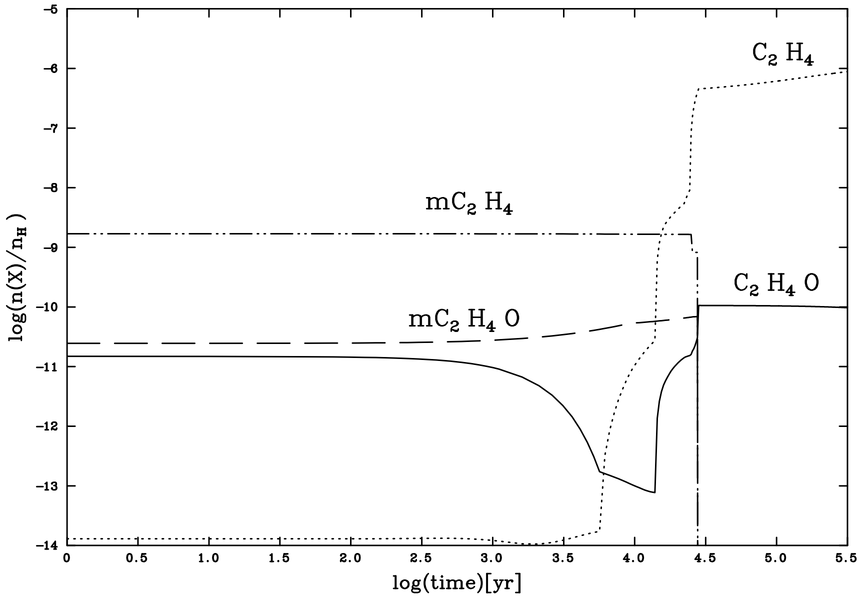

Figure 4.3. Fractional abundances of ethylene oxide in both the gas phase and on grain surfaces as a function of time during Phase II for model M7. The trends of C_2H_4 in gas phase (dotted line) and on grain surfaces (dashed-dotted line) are also displayed as a reference.

4.3 Results and discussion

We now set the same physical parameters as for M7 (see Table 4.5), simulating the case of a prototypical high-mass star-forming region.

Figure 4.3 reports the evolution of the fractional abundances of ethylene oxide in both gas phase (solid line) and solid state (dashed line) and its precursor C_2H_4 (dotted and dashed-dotted line, respectively) during Phase II. At the end of the collapse, c-C_2H_4O is mostly on the grain surfaces, but its abundance drops rapidly at around 100 K when its co-evaporation with water occurs (after $10^{4.4}$ years). At the same time we observe a small growth in the gas phase c-C_2H_4O abundances thanks to the thermal desorption of solid C_2H_4O. The amount of ethylene oxide in the gas phase remains high at all times due to non-thermal desorption effects.

We then compare the theoretical column densities with the observations towards several high-mass star-forming regions where c-C_2H_4O has been detected (see Table 4.6). In

Table 4.6. Comparison between our theoretical column densities (in cm^{-2}) from model M7 with those observed towards several high-mass star-forming regions (Ikeda et al. 2001; Wilner et al. 1994).

	$c\text{-}C_2H_4O$	CH_3OH	$HCOOCH_3$	CH_3CN
Model	6.2×10^{13}	2.4×10^{17}	5.6×10^{15}	2.2×10^{16}
Observations	1.3×10^{13}–1.7×10^{14}	1.4×10^{16}–1.4×10^{17}	1.0×10^{14}–1.2×10^{16}	$\geq 2.1\times10^{16}$

general, we achieve a good agreement, within an order of magnitude, with all of the observed values for $c\text{-}C_2H_4O$ reported by Ikeda et al. (2001). Referring to the range of column densities reported by these authors, we consider M7 as the model representing most of the physical characteristics of the regions listed in Ikeda et al. (2001).

In Table 4.6, we also report results for the calculated and observed column densities for three typical hot core tracers, CH_3OH, $HCOOCH_3$ and CH_3CN. The first two species were detected by Ikeda et al. (2001), the latter molecule was investigated by Wilner et al. (1994), who mapped the methyl cyanide lines in the millimetre spectrum of the Orion KL region. The trends of the fractional abundances of these species as a function of time are displayed in Figure 4.4. The $c\text{-}C_2H_4O$, CH_3OH (solid line), $HCOOCH_3$ (dashed line) and CH_3CN (dotted line) theoretical column densities agree perfectly with observational estimates.

This result suggests that the reaction between atomic oxygen and ethylene on grains is a suitable formation route for ethylene oxide.

4.4 Conclusions

We have investigated the feasibility of the reaction between oxygen ice and ethylene ice as possible route for the formation of ethylene oxide. For this purpose, we employed a chemical model for a collapsing core by updating the rate for the formation of ethylene oxide by using the recent experimental determination of this quantity of Ward & Price (2011). We also tested the sensitivity of ethylene oxide fractional abundances to the changes in the main physical parameters of the collapsing core. We finally reproduced the effects of non-thermal and thermal desorption of ethylene oxide during both the collapse and the warm-up phase, respectively.

Our work shows a good agreement between our estimated column densities for ethylene oxide (under hot core conditions) and those observed towards several high-mass star-

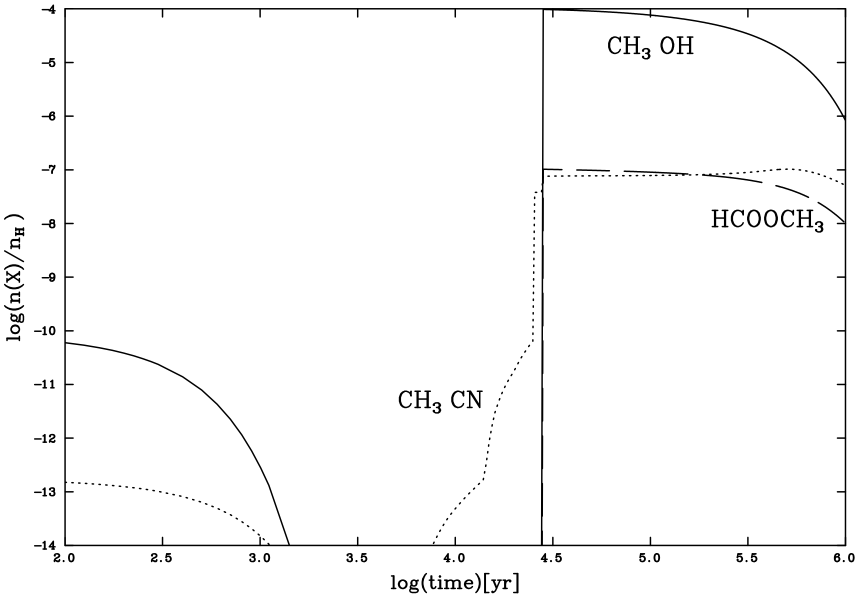

Figure 4.4. Theoretical fractional abundances of three typical tracers of hot cores: CH_3OH (solid line), $HCOOCH_3$ (dashed line) and CH_3CN (dotted line).

forming regions (Ikeda et al. 2001). In order to verify the reliability of our comparison we also looked at the theoretical and observational abundances of other molecules, such as CH_3OH, $HCOOCH_3$ and CH_3CN, known as good tracers of hot cores. We conclude that c-C_2H_4O can form on the grain surfaces thanks to the reaction between oxygen and ethylene.

We stressed that the depletion of only 1% of oxygen atoms has to be in form of oxygen ice in order to produce ethylene oxide on the icy mantle (see Section 4.1); we also note that there is experimental evidence for a small quantity of ethylene being produced during the hydrogenation of acetylene to form ethane; therefore, it is robust to assume that 1% of acetylene is hydrogenated to solid ethylene as an initial condition of our model. This amount of ethylene is already enough for the observed c-C_2H_4O column densities to be reproduced by our theoretical results.

Further experimental studies are perhaps needed to extend our study to other cyclic species that have been detected in the ISM, although the complexity of larger molecules may prevent their isomeric speciation as is the case for the recent laboratory study of the formation of C_3H_6O.

An alternative interpretation of the experimental results used in the present Chapter is described in Chapter 5. We also expand the chemistry of ethylene oxide to include a complete network of reactions for one of its isomers, acetaldehyde, in order to highlight differences and analogies between their chemical behaviours and to investigate possible correlations in their interstellar abundances.

Chapter 5

Ethylene oxide and acetaldehyde in the early stages of star formation

The work presented in this Chapter is based on the paper by Occhiogrosso et al., submitted to A&A, in collaboration with A. Vasyunin, E. Herbst, S. Viti, M. D. Ward, S. D. Price and W. A. Brown. This work is also the result of a collaborative visit to Prof. E. Herbst at the University of Virginia.

In this Chapter we extend our study on ethylene oxide (discussed in the previous Chapter) to its isomer acetaldehyde in order to highlight analogies and differences in their chemical behaviours.

The importance of ethylene oxide as well as acetaldehyde in the ISM has already been stressed in Chapter 4, where we have also investigated the feasibility of a new solid state route for the ethylene oxide production; however we did not include in our simulation the chemistry of its isomers and given the lack of observational data on vinyl alcohol in star-forming regions, we do not include this isomer in the calculations performed in the present study.

We now employ an alternative code labelled MONACO (Vasyunin & Herbst 2013) to our standard UCL_CHEM code and use a different approach for the treatment of the experimental data for the formation of c-C_2H_4O from atomic oxygen and ethylene (Ward & Price 2011). We do not attempt to include the high-energy electron irradiation mechanisms

Table 5.1. Non-zero initial abundances of species (with respect to the total number of hydrogen nuclei) used in the MONACO chemical model, based on Wakelam & Herbst (2008).

H	H_2	He	N	O	C^+	S^+
1.0×10^{-3}	4.9×10^{-1}	9.0×10^{-2}	7.6×10^{-5}	2.6×10^{-4}	1.2×10^{-4}	8.0×10^{-8}
Si^+	Fe^+	Na^+	Mg^+	Cl^+	P^+	F
8.0×10^{-9}	3.0×10^{-9}	2.0×10^{-9}	7.0×10^{-9}	1.0×10^{-9}	2.0×10^{-10}	6.7×10^{-9}

on ices of Bennett et al. (2005) since neither code is equipped to model these processes effectively.

In Section 5.1, we describe the details of the MONACO chemical model and we dedicate Subsection 5.1.1 to the computational treatment of the laboratory data. In Section 5.2, we present the results from the MONACO network and code, and we report a comparison with previous theoretical and observational work in Section 5.3. Our conclusions are given in Section 5.4.

5.1 Method

We use a modified version of the MONACO gas-grain chemical network/model, which was first implemented by Vasyunin et al. (2009) and then extended in order to take into account of the internal monolayers below the ice surface (Vasyunin & Herbst 2013). Although the latest version uses a Monte Carlo approach, the version used here is based on the rate equation method proposed by Hasegawa et al. (1992) and applied to the treatment of the diffusion mechanism, treating the ice as a bulk system (more details about this approach are given in Chapter 1, Section 1.7). The diffusion describes the mobility of species in the mantle and on its surface after they have been adsorbed. Specifically, molecules can jump between two adjacent sites either due to thermal energy (thermal hopping) or because of tunnelling effects. The theory behind these two mechanisms is explained in more detail in Subsection 5.1.1. In the MONACO model, molecular hydrogen, helium and ions are not allowed to stick on the grain surface, unlike all the other species, which accrete to it with a sticking coefficient of unity.

The code is used to treat the chemistry that occurs during the formation of a dense and warm core starting from a cold (20 K) and relatively diffuse medium (n_H = 3×10^3 cm^{-3}) where all the species (with the exception of hydrogen) are in an atomic form. The non-zero initial fractional abundances with respect to the total number of hydrogen nuclei are taken from Wakelam & Herbst (2008) and are reported in Table 5.1; note that they differ from those set in UCL_CHEM which are based on Sofia & Meyer (2001) (see Table 2.1). The species, with the exception of hydrogen and helium, have initial abundances significantly below those observed in diffuse interstellar clouds, with some metallic elements two orders of magnitude lower than the solar elemental abundances. These abundances are often referred to as “low-elemental” abundances (Vasyunin & Herbst 2013) and are often used in order to take into account additional elemental depletion on grains in cold interstellar cores.

Instead of assuming a constant density during the cold pre-stellar-core stage, or assuming an isothermal collapse during this stage, we describe the initial stage as one in which the temperature decreases from 20 K to 10 K in order to account for the fact that the efficiency of radiative heating of grains drops as the visual extinction increases. At the same time, the density increases, mimicking a collapse to form a cold core in which much of the material is in icy mantles. Once the system reaches 10 K, the temperature starts to rise to 200 K in order to reproduce the warm-up phase leading to the formation of a hot core. As a consequence, molecules sublime from the grain mantle. During the initial stages of the warm-up phase, non-thermal desorption effects play an important role. They include desorption due to cosmic-rays, UV photodesorption (treated according to the laboratory study by Öberg et al. 2007), and reactive desorption in which the products of an exothermic surface reaction are immediately ejected into the gas phase (Katz et al. 1999; Garrod et al. 2007). The temperature profile adopted for the hot core formation is shown in Figure 5.1 (left panel). We adapt the temperature profile contained in UCL_CHEM (see Chapter 2) to account for the decrease in temperature from 20 K to 10 K during the collapse phase. This simulation refers specifically to the case of a massive star of approximately 25 $M_{\odot}$.

In the version of the MONACO code employed for the present study, no results from TPD experiments (Collings et al. 2004) are included in the treatment of the thermal desorption (i.e. co-desorption, volcano desorption). Instead we use the method taken from Tielens & Hagen (1982). The mathematical treatment of thermal desorption, or sublimation, is based on the first-order Polanyi-Wigner equation:

$$k_{\mathrm{subl}} = \nu \times e^{-E_{\mathrm{D}}/T} \tag{5.1}$$

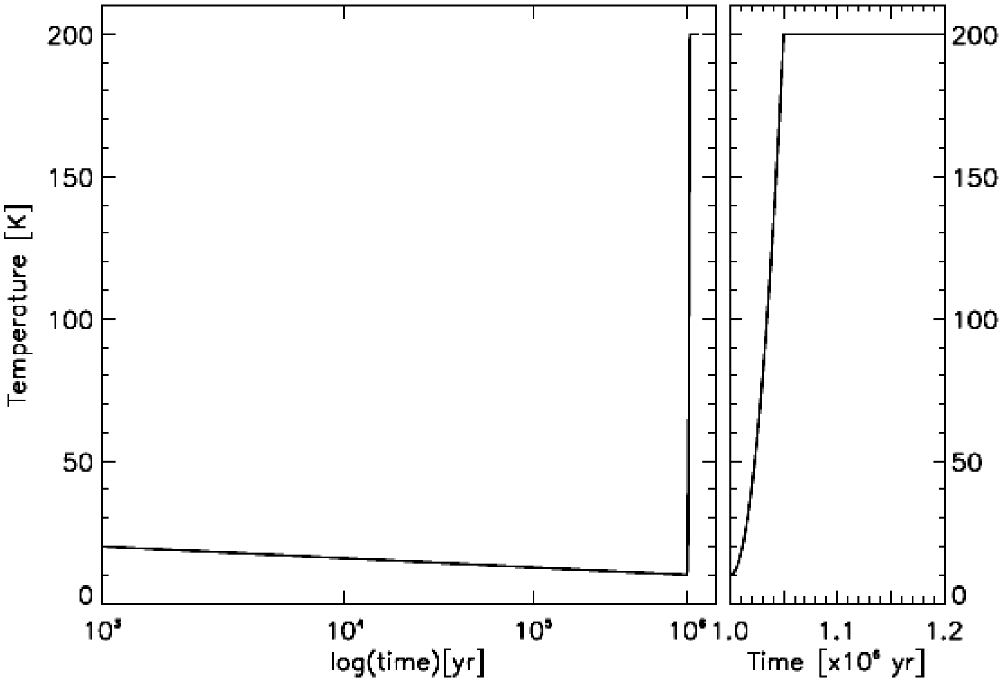

Figure 5.1. The temperature profile during the initial collapse phase and the subsequent warm-up phase leading to hot core formation plotted as a function of time. The panel on the right expands the final portion of the panel on the left.

where the frequency ν, often referred to as the trial frequency, contains a dependence on the molecular mass, $E_{\rm D}$ is the desorption energy for a selected species and T is the temperature in K. The trial frequency for physisorbed H atoms is normally assumed to be $3{\times}10^{12-13}$ s^{-1} (Herbst & Millar 2008). In the present study, we assume a value of 2450 K (Semenov et al. 2010) for the desorption energy for both ethylene oxide and acetaldehyde, although the one reported in the literature only refers to acetaldehyde. During the cold collapse stage, there is little to no thermal desorption (sublimation) for species heavier than hydrogen and helium. During the warm-up stage, the icy mantles eventually totally sublimate, but not before an active mantle chemistry leads to the production of complex molecules (Vasyunin & Herbst 2013).

The chemical network of the MONACO model is based on the OSU gas-grain database (see Chapter 1, Section 1.6) and we introduce the following changes for the purpose of the present study:

1. We insert a complete gas phase reaction network for ethylene oxide based on Table 4.3 in Chapter 4.

Table 5.2. Gas phase rate parameters for acetaldehyde formation and destruction taken from the KIDA database (Wakelam et al. 2012). R_1 and R_2 indicate the reactants and P_1, P_2, P_3 are the different products of the reaction; α, β, and γ are parameters for the rate coefficients, as seen in Equation 5.1.

R1	R2	P1	P2	P3	α [cm^{3}s^{-1}]	β	γ [K]
CH_3CHO	He^+	He	CH_3	HCO^+	1.40×10^{-9}	-0.50	0
CH_3CHO	He^+	He	CH_3CO^+	H	1.40×10^{-9}	-0.50	0
CH_3CHO	H^+	H_2	CH_3CO^+		5.00×10^{-9}	-0.50	0
CH_3CHO	O	CH_3CO	OH		1.79×10^{-11}	0.00	1100
CH_3CHO	OH	CH_3CO	H_2O		1.42×10^{-11}	0.00	0
CH_3CHO	CH_3O	CH_3OH	CH_3CO		8.30×10^{-15}	0.00	0
CH_3CHO	H	CH_3CO	H_2		6.64×10^{-11}	0.00	2120
CH_3CHO	N	H_2	HCN	HCO	1.99×10^{-14}	0.00	0
CH_3CHO	CH_3^+	$C_3H_6OH^+$	photon		5.70×10^{-11}	0.66	0
CH_3CO	C_2H_6	CH_3CHO	C_2H_5		1.95×10^{-13}	2.75	8830
CH_3CO	H_2	CH_3CHO	H		2.21×10^{-13}	1.82	8870
CH_3CO	H_2CO	CH_3CHO	HCO		3.01×10^{-13}	0.00	6510
CH_3CO	CH_4	CH_3CHO	CH_3		4.92×10^{-14}	2.88	10800
CH_3CO	HCO	CH_3CHO	CO		1.50×10^{-11}	0.00	0

2. We include the grain surface route for the formation of ethylene oxide investigated by Ward & Price (2011) in which oxygen atoms associate with ethylene on growing icy mantles covering a substrate of graphite (HOPG). The manner in which we utilise and adapt the experimental results of Ward & Price (2011) is explained in detail in Subsection 5.1.1. Acetaldehyde is produced either by several gas phase routes, or via an association reaction in the icy mantles.

3. We update some of the gas phase reaction rate coefficients involving acetaldehyde using values from the KIDA database (Wakelam et al. 2012) and we report them in Table 5.2.

As mentioned in Subsection 3.2.1, the rate parameters can be inserted in the following formula (also known as the Kooij formula) in order to evaluate the rate coefficients in units of cm^3 s^{-1}:

$$k(T) = \alpha(T/300)^{\beta}e^{-\gamma/T}, \tag{5.2}$$

where α, β and γ are the parameters characterising the variation of the rate coefficients with temperature. Reaction rates are calculated by solving coupled first-order differential equations with respect to the evolution time of the core, depending on the reactant concentrations and on the rate coefficients. The outputs from the code are fractional abundances (X), with respect to the total density of hydrogen nuclei, which can be easily converted into column densities (see Equation 4.4 in Chapter 4).

5.1.1 Computational treatment of experimental data

In their study of ethylene oxide formation, Ward & Price (2011) reported a value of 1.2×10^{-19} cm^2 s^{-1} for the reaction rate coefficient of the association between O and C_2H_4 at 20 K. From the temperature dependence of the rate coefficient, they also determined a total energy barrier of 190 K. This quantity represents the contribution to the system of the activation energy as well as the diffusion barrier E_{D}, if we assume the reaction is to occur via diffusion. The rate coefficient for the formation of ethylene oxide can then be expressed as

$$k = a \times e^{-190/T} \tag{5.3}$$

from which it follows by substitution of the value at 20 K that $a = 1.6\times10^{-15}$ cm^2 s^{-1}. In order to obtain the rate coefficient in units of s^{-1}, which is necessary if the amounts of reactants are expressed as numbers rather than real concentrations, we multiply a by the site density $d_{\mathrm{site}} = 1.5\times10^{15}$ cm^{-2} (Hasegawa et al. 1992) to determine a value of a[1] equal to 2.4 s^{-1}.

If we assume that the reaction proceeds via diffusion, also known as the Langmuir-Hinshelwood mechanism (see Chapter 1, Subsection 1.3.2), we can also make the approximation that at low temperatures, the diffusion is dominated by light atomic species, in this case oxygen. As reported by Herbst (1985), if we neglect the effect due to quantum tunnelling, the hopping rate coefficient can then be expressed by Equation 5.1, where E_D is now the diffusion barrier (in units of K) between two adjacent binding sites. For a system in which there is also chemical activation energy, the diffusion barrier must be replaced by a total energy, which we label E_{tot}.

The first-order rate coefficients for diffusion are defined as the hopping rates over a number of reactive sites equivalent to the total number of sites on the dust particles. The

---

[1] Note that a in Equation 5.3 $\neq \alpha$ in Equation 5.2 because a has the units of area [cm^2 s^{-1}] as it refers to a surface reaction.

concentrations of surface species are expressed in units of numbers per grain. Starting with a trial frequency of $3{\times}10^{12}$ s^{-1} and a total number of 10^6 sites for a grain radius of 0.1 μm, we obtain a reduced frequency of $3{\times}10^6$ s^{-1}. To obtain the theoretical total barrier $E_{\rm tot}$ in the diffusive approach, we equate the laboratory formula for the rate coefficient with the theoretical formula:

$$2.4 \times e^{-190/T} = 3 \times 10^6 e^{-E_{\rm tot}/T}. \tag{5.4}$$

Note that according to Equation 5.4 the energy barrier shows a temperature dependence. It follows that we cannot assume a fixed value for $E_{\rm tot}$ during the warm-up phase of our model, where the temperature changes from 10 K to 200 K. By solving Equation 5.4, we obtain the trend for the theoretical energy barrier (see Equation 5.5), that we introduce in our calculations:

$$E_{\rm tot}(T) = 190 + 14.22 \times T \quad \mathrm{K}. \tag{5.5}$$

We also point out that the experimental expression used here is only valid over a temperature range of 10–90 K. Despite the fact that we run our models up to 200 K, any deviation from Arrhenius behaviour in the fit to the experimental data will not affect our results as ethylene oxide and acetaldehyde both desorb at temperatures much lower than 90 K (~65 K, see the following Section for more details).

5.2 Modelling

In the present study we adopt two different sets of physical conditions. First, we consider a one-phase model that runs at a single temperature and density. Secondly, as mentioned previously, we consider a more complex two-phase model based on a density-temperature profile that follows an initial cooling down as the density increases (Phase I or collapse phase) until densities typical of a hot core are reached, at which time the warm-up phase (Phase II) begins. During the latter phase, species desorb from the grain surfaces back into the gas phase at different temperatures depending on their desorption energies (Garrod et al. 2006b, 2008a). We run our model over 10^6 years.

We start by inserting a complete chemical network for ethylene oxide into the MONACO network. We include the gas phase channels reported in Table 4.3 of Chapter 4. We com-

Table 5.3. Results for gaseous and solid ethylene oxide fractional abundances at 1.2×10^6 years in different single-temperature chemical models.

	$n_{\rm H}$ [cm^{-3}]	T [K]	N-td	X(c-C_2H_4O)	X(mc-C_2H_4O)
M1	10^4	10	ON	5.7×10^{-14}	6.8×10^{-18}
M2	10^4	15	ON	3.7×10^{-14}	5.5×10^{-18}
M3	10^4	20	ON	6.3×10^{-15}	1.1×10^{-18}
M4	10^4	20	OFF	1.9×10^{-17}	1.1×10^{-12}
M5	10^4	50	ON	4.6×10^{-15}	1.2×10^{-18}
M6	10^4	50	OFF	2.0×10^{-21}	6.4×10^{-25}
M7	10^7	200	ON	3.3×10^{-16}	2.1×10^{-32}
M8	10^7	200	OFF	3.3×10^{-16}	2.1×10^{-32}
M9	10^8	300	ON	4.3×10^{-18}	5.8×10^{-35}
M10	10^8	300	OFF	4.3×10^{-18}	5.8×10^{-35}

The m before the molecular formula stands for *mantle*

plete the reaction scheme by introducing other desorption mechanisms for solid ethylene oxide.

Single-temperature models have been run in order to predict the ethylene oxide fractional abundances at different specific temperatures and densities. The different physical parameters adopted for these preliminary models are listed in Table 5.3 along with the ethylene oxide fractional abundances in the gas phase as well as in the icy mantles (the m before the molecular formula stands for *mantle*).

Assuming local thermodynamic equilibrium conditions, we adopt $T_{dust} = T_{gas}$. We utilise different temperatures as well as densities in order to test the sensitivity of the molecular abundances to the changes in these parameters. In order to emphasise the effects due to non-thermal desorption (N-td), we run models with these processes ON and OFF.

Our results are summarised in Table 5.3, which reports the fractional abundance of ethylene oxide in the gas phase (X(c-C_2H_4O)) as well as on the grain surface (X(mc-C_2H_4O)) at the final time. They show that, regardless of the different physical parameters chosen and assuming that all the solid ethylene oxide sublimates to the gas phase, the models are unable to produce gaseous ethylene oxide above the detection threshold ($\sim10^{-12}$) with the exception of model M4, where ethylene oxide reaches an abundance of the order of 10^{-12} on the grain surface. A general conclusion is that non-thermal desorption is more efficient at low temperatures than at higher temperatures, when the thermal desorption becomes more important. This is unequivocal if we look at the fractional abundances of our molecule obtained as output from the models at higher temperatures with and without the influence due to non-thermal desorption effects: in both cases the amount of ethylene oxide is still the same. Some effects mainly due to reactive desorption can be highlighted at 50 K (see M5 and M6), but the major consequences due to non-thermal desorption are manifest at 20 K (see M3 and M4) where ethylene oxide is not efficiently produced on the grain surface when the mechanism is operating.

Single temperature models are advantageous in terms of computational time but the chemical scenario may not be realistic because reactants can conspicuously desorb before they interact to produce more complex species, depending upon the temperature chosen. Moreover, star formation occurs with rising temperatures. Hence, we ran models where the temperature eventually increases as a function of time. This helps to produce complex molecules in the gas phase because at temperatures usually $T \geq 25$ K, molecular reactants on the grain start to diffuse appreciably and react after photo-activation to form complex molecules. The complex molecules formed on the grains then either start to evaporate as the temperature continues to rise or they desorb non-thermally (Garrod et al. 2006b, 2008a).

As previously mentioned, the warm-up phase model runs in two stages. First, we follow the trend for the free-fall collapse during which we observe an increase in density from 3×10^3 cm^{-3} to 10^7 cm^{-3} and a decrease in temperature from 20 K to 10 K to account for the fact that the efficiency of radiative heating of grains drops as the visual extinction increases (Vasyunin & Herbst 2013). The visual extinction is initially set equal to 2 mags and by the end of Phase I it rises to $\sim$430 mag. The simulation continues until the final density is reached, which takes over 10^6 years. The accretion efficiency is controlled by the sticking probability of gaseous atoms and molecules, which is assumed to be unity. During Phase II, the density is kept constant, while the temperature goes from 10 K up to 200 K over 5×10^4 years. By the end of this second phase a hot core is formed. We consider the process of formation for a massive star of 25 $M_\odot$. Note that lower masses lead to different desorption times as a consequence of the different temperature profiles. Specifically, the sublimation of molecules in lower mass stars is shifted towards higher temperatures (Viti et al. 2004).

Figure 5.2 shows the calculated abundances of gaseous and solid ethylene oxide and acetaldehyde from the two-stage model as a function of time. The solid and dashed lines

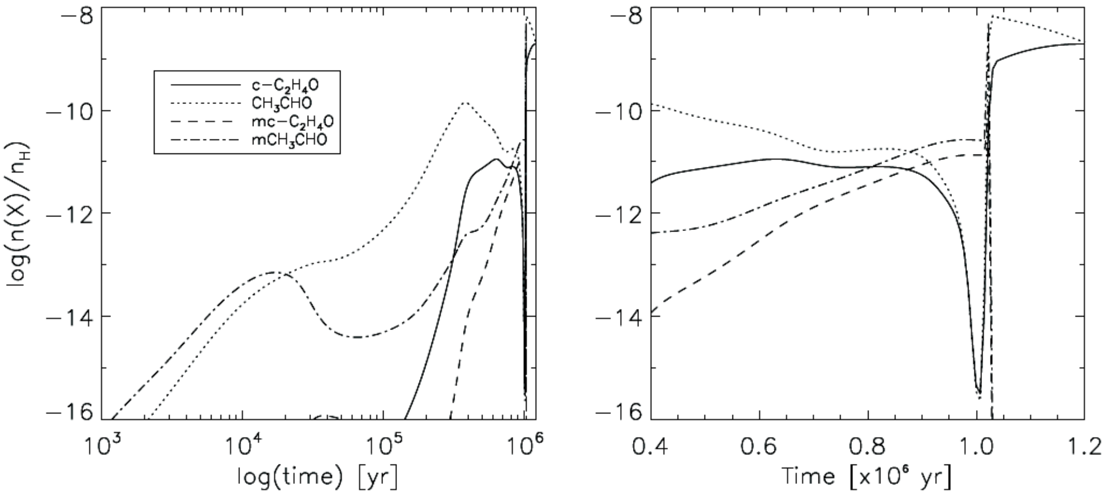

Figure 5.2. Fractional abundances of gaseous and solid ethylene oxide and acetaldehyde as a function of time during two phases, over 10^6 years. The panel on the right expands the final portion of the panel on the left.

represent the abundances of gaseous and solid ethylene oxide, while the dotted and dashed-dotted lines represent the abundances of gaseous and solid acetaldehyde. The panel on the left reports results from the collapse and warm-up phases, while that on the right expands the results from the warm-up phase, where desorption eventually leads to large abundances of gaseous ethylene oxide and acetaldehyde. While the initial diffuse medium is collapsing, ethylene oxide forms slowly on the grain surface via the reaction between oxygen atoms and ethylene. Solid ethylene oxide reaches a peak fractional abundance of about 10^{-11} just before 10^6 years. When the warm-up phase has started, c-C_2H_4O sharply decreases on the grain surface because of changes in the physical conditions that make its production inefficient in the solid state and enable its gas phase formation (see left panel, Figure 5.2). At this stage the cloud temperature is still too low (about 65 K) for most of the icy molecules to desorb, with the exception of CO-like species (Collings et al. 2004) and simple hydrocarbons like methane. Despite the cloud being quite cold, the fact that the rotational temperature for ethylene oxide species has been estimated to be up to 40 K (Nummelin et al. 1998) is enough to justify the early sublimation of solid ethylene oxide reported in Figure 5.2 (right panel). During Phase II, the desorption of c-C_2H_4O from the icy mantles contributes to an increase in its gas phase abundance; we can observe a sharp increment up to $\sim 2\times10^{-9}$ in the abundance of gaseous ethylene oxide just after 10^6 years.

Apart from desorption following the solid phase O + C_2H_4 reaction, another important contribution to the high abundance of ethylene oxide in the gas phase comes from the dissociative recombination reaction below:

$$\mathrm{e^- + C_2H_5O^+ \rightarrow c - C_2H_4O + H;} \tag{5.6}$$

if we assume that the cyclic neutral isomer can be formed from the molecular ion, whose structure (cyclic or non-cyclic) is not followed in our calculations. Thanks to the combined contribution of desorption and dissociative recombination, ethylene oxide reaches a plateau in its gaseous abundance, that lasts until the end of our simulation ($\sim 10^6$ years).

Acetaldehyde is formed on the grain surface by the radical-radical association reaction between CH_3 and HCO. However, gas phase reaction pathways produce a large amount of this molecule to such an extent that the gaseous acetaldehyde abundance overcomes the amount of its isomer up to a factor of 3.5 at the peak value. This larger abundance of acetaldehyde compared to ethylene oxide is also predicted by the ratio between the two isomers reported in the literature; this ratio ranges from a lower limit of 1.3 (Ikeda et al. 2001) to 2.6 (Nummelin et al. 1998) on average, although there are still some uncertainties in the derivation of this ratio (e.g. the ratio was found to be equal to 8.5 in G327.3–0.6, Nummelin et al. 1998).

The main channel for acetaldehyde production is the reaction between O and C_2H_5, that contributes 40% on average of the overall rate of formation at 1.2×10^6 years. As with the case of ethylene oxide, another gas phase contribution to acetaldehyde formation comes from dissociative recombination of $C_2H_5O^+$:

$$\mathrm{e^- + C_2H_5O^+ \rightarrow CH_3CHO + H} \tag{5.7}$$

assuming that the ion can form a non-cyclic structure upon recombination.

The ionic species is in turn formed via several gas phase reactions including the one between CH_4 and H_2CO^+, which represents the most favourable reaction pathway. The ion is also formed by so-called *loop* reactions, in which neutral acetaldehyde is protonated by ions such as H_3^+ and H_3O^+:

$$CH_3CHO + H_3^+ \longrightarrow C_2H_5O^+ + H_2 \quad (5.8)$$

$$CH_3CHO + H_3O^+ \longrightarrow C_2H_5O^+ + H_2O \quad (5.9)$$

Such reactions can also be considered as destruction reactions of acetaldehyde as long as the protonated ion does not fully re-convert back to acetaldehyde.

By comparison, as with the case of ethylene oxide, the abundance of gaseous acetaldehyde increases up to 10^{-10} just after 10^5 years and shows a peak at $\sim 6.8\times10^{-9}$ just after 10^6 years; therefore, as for the case of ethylene oxide, acetaldehyde desorbs at lower temperatures than previously predicted.
Finally, the acetaldehyde's gas phase abundance drops to 1.9×10^{-9} by the end of our simulation due to the reaction with H_3O^+ to form $C_2H_5O^+$ and H_2O (see reaction 5.9).

5.3 Results and Discussion

In this section we compare our hot core results with those from the models developed in our previous Chapter, as well as with observations. In Chapter 4, we used UCL_CHEM to investigate the chemistry of ethylene oxide towards high-mass star-forming regions and it was able to reproduce its observed abundances in these environments.

In Table 5.4 we therefore report the fractional abundances for the two isomers achieved with the MONACO model for a hot core at their peak value and those from our best model in Chapter 4 for the case of a massive protostar of 25 $M_\odot$ at 200 K. At the final time, the fractional abundance of ethylene oxide obtained using the UCL_CHEM model is lower by one order of magnitude compared to that used in our models. We point out that the simulations performed in Chapter 4 did not take into account the chemistry of acetaldehyde and this factor may affect the results. Moreover, relatively high temperatures (~100 K) were needed in order to desorb ethylene oxide from the grain surface to the gas phase; hence, we did not predict the peak of the ethylene oxide abundance at around 65 K as found by running the MONACO model.

In light of these dissimilarities we update the UCL_CHEM model with a complete network of reactions for acetaldehyde as shown in Table 5.2. We also included grain chemistry for this species taken from the MONACO model. Although the two codes

Table 5.4. Comparison between the fractional abundances of the two isomers derived from MONACO (at 10^6 years) and those obtained in Chapter 4 (at 200 K).

	c-C_2H_4O	CH_3CHO
MONACO	1.9×10^{-9}	6.8×10^{-9}
UCL_CHEM	1.0×10^{-10}	-

present important differences in the way they treat the physics and chemistry under ISM conditions, we minimised these divergences by using in UCL_CHEM the same physical parameters as in the simulations performed with the MONACO code.

One of the key issues concerns the treatment of the thermal desorption of species occurring during the warm-up phase. In Chapter 4, we adopted the classification of species developed by Viti et al. (2004) (see Chapter 2) and we set the thermal desorption of ethylene oxide from the grain surface to occur at ∼100 K via co-desorption with water ices. In order to investigate the presence of a peak of ethylene oxide at lower temperatures, we now assign ethylene oxide as intermediate between CO- and H_2O-like molecules in their desorption pattern. This signifies that ethylene oxide will undergo mono-molecular desorption (which will depend on its binding energy of ∼2450 K), volcanic desorption and co-desorption with water ice. Based on the similarities found in their gas phase chemical behaviours, we assume acetaldehyde to behave similarly to its isomer. Moreover, we set in UCL_CHEM the same initial elemental abundances as in the MONACO models (see Table 5.1).

The output for ethylene oxide and acetaldehyde obtained from the updated chemistry in UCL_CHEM is plotted in Figure 5.3. The plot shows the fractional abundances of gaseous (solid line) and solid (dashed line) ethylene oxide as well as gaseous (dotted line) and solid (dashed-dotted line) acetaldehyde, during the warm-up phase leading to a hot core. For both isomers we clearly observe the existence of a sharp desorption peak during which the gas phase abundance first increases sharply and the solid state abundance decreases. The sharp decrease in the solid state abundances of both molecules at 6×10^3 years occurs at even lower temperatures (∼43–45 K) than those predicted by running the MONACO model. Volcanic and co-desorption effects can also be highlighted at late stages.

Comparing the results obtained from the two codes, we find general agreement in predicting the sub-thermal sublimation of the two isomers. Another important consideration concerns the ratio between the acetaldehyde-to-ethylene oxide abundances in the gas phase

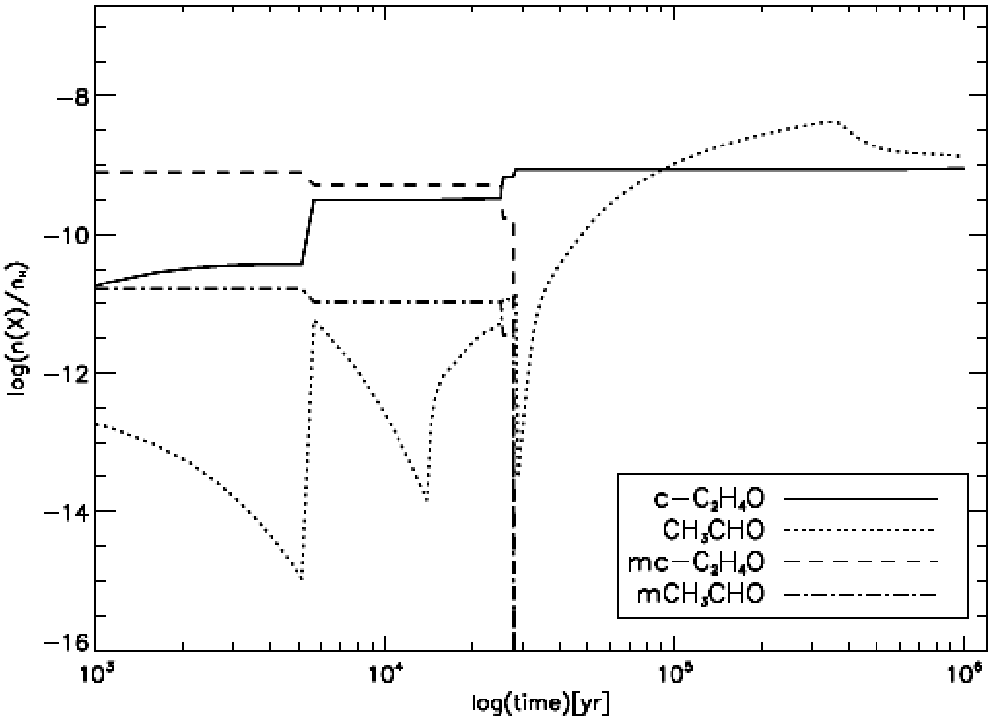

Figure 5.3. Fractional abundances as a function of time [years] for ethylene oxide and acetaldehyde, both in the gas phase and on the grain surface. The output obtained by running UCL_CHEM refers to the warm-up phase.

at the end of the warm-up phase (∼1.2×10^6 years). From UCL_CHEM, we find a value of ∼1.5, which fits well within the interval of values reported in the literature (Nummelin et al. 1998; Ikeda et al. 2001).

We finally compare the new fractional abundances obtained by running UCL_CHEM with those from MONACO and with some observations towards various high-mass star-forming regions by Ikeda et al. (2001). The results are summarised in Table 5.5. Note that the UCL_CHEM value for ethylene oxide abundance has increased from the value in Table 5.4 by a factor of 9, due principally to reactions involving the conversion of acetaldehyde, newly added to the model, to ethylene oxide.

All of the theoretical fractional abundances agree within less than an order of magnitude to their corresponding observational values. The observed ranges reported in Table 5.5 do not include the abundances of molecules detected towards Orion S and Orion Compact Ridge since these two sources are characterised by a different density compared with that used in our models.

Table 5.5. Comparison between the fractional abundances of the two isomers obtained from MONACO and UCL_CHEM models (at 200 K) and with observations towards several high-mass star-forming regions (fractional abundances taken from Ikeda et al. 2001).

	c-C_2H_4O	CH_3CHO
MONACO	2×10^{-9}	2×10^{-9}
UCL_CHEM	9×10^{-10}	1×10^{-9}
[1]Observations	4×10^{-11}–6×10^{-10}	8×10^{-11}–3×10^{-9}

[1] Note that observations of c-C_2H_4O refer to a T_{rot} between 11 K and 36 K range and those of CH_3CHO are in the 14–33 K temperature range.

5.4 Conclusions

We used the MONACO code, written by Vasyunin & Herbst (2013), to model the formation and destruction of ethylene oxide and acetaldehyde for a typical hot core. In particular, we extended the MONACO model to include recent experimental results (Ward & Price 2011) on ethylene oxide formation on icy mantle analogues by the association of oxygen atoms and ethylene.

For comparison, we considered our previous study in Chapter 4 that focused on the formation of solid ethylene oxide and we inserted a reaction network for the formation and the loss pathways of acetaldehyde into the UCL_CHEM code. We then ran a model with the same physical parameters as in the simulation performed using the MONACO model. Our main conclusions from this computational analysis are:

1. By employing the two different codes, ethylene oxide and acetaldehyde seem to have a similar desorption behaviour, showing an increase in their gaseous abundances at low temperatures during the warm-up phase of the star formation process. In particular, both codes for ethylene oxide display a plateau after its gaseous abundance reaches its peak value, while, in both cases, the amount of acetaldehyde slightly decreases (after its peak value) due to the reaction with H_3O^+ to form $C_2H_5O^+$ and H_2O (see reaction 5.9).

2. Both models show a more efficient formation of ethylene oxide on grains compared with the amount of solid acetaldehyde produced at early stages during the collapse phase. After $\sim10^6$ years the importance of the surface reaction for ethylene oxide formation becomes comparable to its production in the gas phase thanks to the loop reactions in which acetaldehyde is destroyed to form $C_2H_5O^+$ (which is in turn one

of the reactants to produce gaseous ethylene oxide, as shown in reaction 5.6). These reaction chains are a possible explanation supporting the speculation that ethylene oxide should be present everywhere acetaldehyde is observed.

3. The theoretical ratios between the fractional abundances of the two isomers evaluated with both codes fit well within the range of values reported in the literature for the case of a hot core source (Nummelin et al. 1998; Ikeda et al. 2001). This factor may be important to quantify the amount of ethylene oxide towards cold regions based on the acetaldehyde abundance in these astronomical environments.

4. A final important consideration regards the theoretical treatment of the experimental results. Despite the fact that the same laboratory data (Ward & Price 2011) have been used in this Chapter as well as in Chapter 4, different assumptions were made in the two cases in converting experimental data for use in the interstellar environment. In fact, while in Chapter 4 we move from a bi-dimensional system to a three-dimensional space, in the present Chapter we adopt theoretical considerations from the diffusion theory in the convertion of the reaction rates. The consistency between the two approximations in reproducing the ISM chemistry of ethylene oxide and acetaldehyde may be a confirmation of the reliability of the scientific justification asserted in both studies.

While the present Chapter shows what the potential products of the reaction between atomic oxygen and ethylene on the grain surface are, Chapter 6 reveals all the reaction channels experimentally identified for the same reaction in the gas phase. The different mechanisms by which species react according to their physical state adds a note of interest to these particular studies.

Chapter 6

Oxygen chemistry in star-forming regions

The work presented in this Chapter is based on the paper by Occhiogrosso et al. (2013), in collaboration with S. Viti and N. Balucani.

The present Chapter focuses on updates to the oxygen gas phase reaction network based on new experiments by the group of Prof. Nadia Balucani in Perugia, Italy. In particular, it concentrates on the reactions driven by atomic oxygen in the presence of linear carbon-chain molecules.

Oxygen is an important player in ISM chemistry because it is the most abundant element after hydrogen and helium. Interstellar oxygen can be found in different forms and compounds, such as neutral or ionised gas, in the water of icy mantles or even in refractory materials. Its gas phase abundances in the diffuse medium are well known (Meyer 1997), while the oxygen chemistry in denser environments seems to be poorly understood due to observational constraints (Jensen et al. 2005).

Oxygen chemistry has been widely investigated towards extragalactic and galactic environments, where it seems there is a correlation between the oxygen and carbon chemistries. In particular, in line with the fact that the C/O ratio determines the kind of reactions taking place in a specific region of ISM (Tsuji 1973), Agúndez & Cernicharo (2006), looking at the circumstellar shells of IRC+10216, observed that carbon is locked either as CO or other O-bearing species when $C/O < 1$, while a higher concentration of reduced C-bearing species is present when $C/O > 1$. The latter condition leads to an increase in the growth of unsaturated hydrocarbons.

The presence of hydrocarbons in carbon-rich environments has been extensively confirmed by modelling and observations; in particular, Millar et al. (2000b) found a large abundances of unsaturated hydrocarbons and cyanopolyynes, by computing the physical conditions around the carbon-rich star IRC+10216 and these abundances appear to be enhanced at sub-solar metallicities (Woods et al. 2012). Unsaturated hydrocarbons are organic molecules characterised by double or triple covalent bonds between adjacent carbon atoms; presently, there is no generally accepted explanation of their formation mechanisms but, as mentioned above, their abundances seem to be inversely correlated to the availability of atomic oxygen (Fortney 2012). The most likely reactions originate with unsaturated hydrocarbons and proceed through the addition of atomic and radical species, breaking their unsaturated bonds. In most cases, the elimination of a hydrogen atom or of a group follows, leading to more complex compounds (see, for instance, the cases of the reactions $C + C_2H_2$, $C_2 + C_2H_2$, $CN + C_2H_2$, Huang et al. 2000; Kaiser 2002, 2003; Leonori et al. 2008, 2010).

Recent experiments in the gas phase (Capozza et al. 2004; Fu et al. 2012a,b; Leonori et al. 2012) suggest that the C–C bond-breaking channel with the formation of CO is an important reaction channel for the reaction $O + C_2H_2$ and $O + C_2H_4$, while it is by far the dominant loss path for the reactions $O + CH_2CCH_2$ (allene). The fact that the reactions of atomic oxygen with unsaturated hydrocarbons lead in one step to CO can have a pivotal role in estimating the CO abundances both in the gas phase and on grain surfaces. Carbon monoxide is in turn a key species for the synthesis of organic complex molecules on grain surfaces since it can easily hydrogenate to methanol as experimentally demonstrated by Modica & Palumbo (2010).

Another important aspect regarding these small hydrocarbons is their loss paths to form CH_2. This molecular radical is known to be a potential precursor of polycyclic aromatic hydrocarbons (PAHs) and many studies have been performed to investigate the several implications due to the presence of these aromatic hydrocarbons on the dust (Verstraete 2011; Salama 2008). On the other hand, small unsaturated hydrocarbons are the building blocks of polyynes (organic compounds with alternating C–C single and triple bonds) and cumulenes (hydrocarbons with three or more consecutive C=C double bonds) that are also known as starting points for the synthesis of PAHs.

In the present study, we focus on the reactions between O atoms and small unsaturated hydrocarbons, namely, acetylene, ethylene, methylacetylene and allene, under interstellar medium conditions. In particular, we propose a revised chemical scheme (compared to those included in the available databases) where our reaction rates are based on new experimental branching ratios (BRs) for different reaction channels. In order to assess the effects of recent laboratory data on hydrocarbon abundances across different astrophysical environments, we model four typical astrochemical regions and we compare our theoretical results with the observations. The chapter is organised as follows: Section 6.1 describes the laboratory technique used and the revised chemistry we inserted in our model; Section 6.2 focuses on the modelling of four different astrochemical environments; results are discussed in Section 6.3 and our conclusions are summarised in Section 6.4.

6.1 The reactions of atomic oxygen with small unsaturated hydrocarbons

The following gas phase neutral-neutral reactions were experimentally investigated as part of my Master degree studies at the University of Perugia by means of the crossed molecular beam (CMB) technique with mass spectrometric detection (Occhiogrosso 2010).

- $O + C_2H_4 \rightarrow$ products
- $O + C_2H_2 \rightarrow$ products
- $O + CH_3CCH \rightarrow$ products
- $O + CH_2CCH_2 \rightarrow$ products

In particular, the reaction mechanisms, the nature of the primary products of the different competing channels and their branching ratios have been determined (Capozza et al. 2004; Fu et al. 2012a,b; Leonori et al. 2012). From the analysis of the measured product angular and velocity distributions, the product branching ratios are evaluated. The CMB technique with mass spectrometric (MS) detection is an adequate tool for the investigation of elementary reactions under single collision conditions; a detailed description of the procedure can be found in Balucani et al. (2006) and Casavecchia et al. (2009). To derive the rate for each reaction channel, we consider the global rate constants for O + C_2H_2, O + C_2H_4, O + CH_3CCH and O + CH_2CCH_2 scaled by the experimental BRs (see Table 6.1 and Table 6.3). For the reactions listed in Table 6.1, the rate coefficients and temperature dependence are those recommended by Baulch et al. (2005) in the range 200–2500 K and 220–2000 K for the two reactive systems, respectively. For the reactions reported in Table 6.3, we have considered the rate constants and temperature dependence recommended by Cvetanovic (1987) in the ranges 290–1300 K and 290–500 K for the two isomers, respectively. The temperatures of interest in interstellar objects are lower than those for which the temperature dependencies have been determined. Therefore, we have extrapolated the trends down to 10 K, but this is an approximation and significant deviations are possible.

The oxygen chemistry with hydrocarbons based on the new laboratory data was inserted in the UCL_CHEM chemical model (see Chapter 2 for the details about the code). Besides new experimental values for the reactions listed above, we updated the chemical network with a new species, the ketyl radical (HCCO), which is produced in the reaction O + C_2H_2. To date, HCCO has not been detected in the interstellar medium, but its presence was already predicted in the past by Turner & Sears (1989) who provided an upper limit for the HCCO/H_2CCO ratio.

We also introduced the vinoxy radical (CH_2CHO), produced in the reaction O + C_2H_4. Furthermore, in addition to methylacetylene, its isomer CH_2CCH_2 (allene or propadiene) is explicitly considered. We have used either laboratory data or the rate coefficients included in the KIDA database (Wakelam et al. 2012) for the reactions that involve these two hydrocarbon species. This distinction is not present in the UMIST database by Woodall et al. (2007) nor in its new version recently published by McElroy et al. (2013).

We first investigate how the revised part of the chemical model affects the trends in the hydrocarbon fractional abundances (relative to hydrogen nuclei) at typical densities in the ISM. Thus, we run a grid of models representing (i) a diffuse cloud, (ii) a translucent cloud, (iii) a dark core and (iv) a hot core. We analyse the contribution to the hydrocarbon abundances from their primary products formed during their interactions with oxygen atoms. We finally compare our theoretical hydrocarbon abundances with those from the observations in cold and warm interstellar medium environments, where these species have been detected.

Table 6.1. Rate constants (at 200 K, typical for a hot core) for the different competing reaction channels for ethylene and acetylene with oxygen atoms. The last column contains the formula (taken from the NIST database) adopted in order to evaluate the rate constants.

Reaction	BRs[%]	k(200K)[cm^3 mol^{-1} s^{-1}]	k(T)[cm^3 mol^{-1} s^{-1}]
$O + C_2H_2 \rightarrow HCCO + H$	79	9.9×10^{-15}	1.89×10^{-12} (T/298K)$^{2.10}$ e$^{-786/T}$
$O + C_2H_2 \rightarrow CH_2 + CO$	21	2.6×10^{-15}	
$O + C_2H_2 \rightarrow C_2H + OH$	0	0	
$O + C_2H_4 \rightarrow CH_3 + HCO$	34	1.0×10^{-13}	1.01×10^{-12}(T/298K)$^{1.88}$ e$^{-92/T}$
$O + C_2H_4 \rightarrow CH_2CHO + H$	30	9.0×10^{-14}	
$O + C_2H_4 \rightarrow H_2CO + CH_2$	20	6.0×10^{-14}	
$O + C_2H_4 \rightarrow CH_2CO + H_2$	13	3.9×10^{-14}	
$O + C_2H_4 \rightarrow CH_3CO + H$	3	9.0×10^{-15}	
$O + C_2H_4 \rightarrow C_2H_3 + OH$	0	0	

Table 6.2. Loss processes for HCCO (Baulch et al. 2005 and references therein.)

Reaction	k(300K)[cm^3 mol^{-1} s^{-1}]
$H + HCCO \rightarrow CO + CH_2$	1.7×10^{-10}
$H_2 + HCCO \rightarrow$ products	2.8×10^{-14}
$O + HCCO \rightarrow CO + CO + H$	1.6×10^{-10}

Table 6.3. Rate constants (at 200 K, typical for a hot core) for the different competing reaction channels for methyl acetylene and allene with oxygen atoms. The last column contains the formula (taken from the NIST database) adopted in order to evaluate the rate constants.

Reaction	BRs[%]	k(200K)[cm^3 mol^{-1} s^{-1}]	k(T)[cm^3 mol^{-1} s^{-1}]
$O + CH_3CCH \rightarrow C_2H_4 + CO$	68.0	5.2×10^{-13}	2.18×10^{-11} e$^{-99/T}$
$O + CH_3CCH \rightarrow C_2H_3 + HCO$	10.0	7.7×10^{-14}	
$O + CH_3CCH \rightarrow C_2H_2 + H_2CO$	10.0	7.7×10^{-14}	
$O + CH_3CCH \rightarrow CH_3CCO + H$	5.5	4.3×10^{-14}	
$O + CH_3CCH \rightarrow CH_3 + HCCO$	0.4	3.1×10^{-15}	
$O + CH_2CCH_2 \rightarrow C_2H_4 + CO$	81.5	9.8×10^{-13}	2.82×10^{-11} e$^{-93/T}$
$O + CH_2CCH_2 \rightarrow C_2H_2 + H_2CO$	9.6	1.1×10^{-13}	
$O + CH_2CCH_2 \rightarrow C_2H_3 + HCO$	7.0	8.4×10^{-14}	
$O + CH_2CCH_2 \rightarrow CH_2CCHO + H$	1.6	1.9×10^{-14}	
$O + CH_2CCH_2 \rightarrow CH_2CO + CH_2$	0.3	3.6×10^{-15}	

6.1.1 The reactions O + C_2H_2 and O + C_2H_4

Ethylene or ethene, C_2H_4, is the simplest alkene (alkenes are hydrocarbons with a carbon-carbon double bond), while acetylene or ethyne, C_2H_2, is the smallest alkyne (alkynes are hydrocarbons with a carbon-carbon triple bond). These two molecules have a similar structure, but their reactivity with oxygen atoms seems to be different (see Table 6.1). In particular, because of the larger number of atoms, ethylene leads to the formation of a greater number of products. According to experimental results (Capozza et al. 2004; Fu et al. 2012a,b) in both cases the channels leading to OH formation are inefficient; these two channels of OH production have low reaction rates also according to the data reported in the UMIST 2006 database (Woodall et al. 2007).

The main channels for the reaction O + ethylene have been found to be those leading to CH_3 + HCO (34%) and CH_2CHO + H (30%) (Fu et al. 2012a,b). Regarding the reaction between acetylene and atomic oxygen, the dominant channel is the one leading to HCCO + H with a BR of 79% while the channel leading to CH_2 and CO accounts for the remaining 21% (Capozza et al. 2004; Leonori et al. 2013).

We find that HCCO might play a pivotal role in the trends of hydrocarbon abundances. To date the ketyl radical has not been included in any database. However, we have introduced a chemistry network for the loss processes of HCCO as shown in Table 6.2, using the summary of Baulch et al. (2005) and we have derived the rate parameters for a few simple reactions involving HCCO with the major gas components.

6.1.2 The reactions O + CH_3CCH (methylacetylene) and O + CH_2CCH_2 (allene)

Since the experimental results by Leonori et al. (2012) and Balucani et al. (in preparation) have demonstrated that the reactions O + CH_3CCH and O + CH_2CCH_2 are characterised by different branching ratios (and also their rate coefficients are different), we have separated the two isomeric species in our codes. The UMIST 2006 database (Woodall et al. 2007) does not distinguish between the two C_3H_4 isomers. Therefore, it is implicitly assumed that CH_3CCH and CH_2CCH_2 are formed and destroyed in the same reactions and with the same efficiency. Such an assumption, however, is not warranted. For instance, it has been suggested that an important contribution to the formation of both isomers is the reaction between methylidyne radical (CH) and ethylene (Gosavi et al. 1985; Wang 1998).

Nevertheless, recent laboratory investigations (Zhang et al. 2012) have shown allene to be the main product with a BR of 75-80%.

To account separately for CH_3CCH and CH_2CCH_2 formation we have inserted the main path rate coefficients as recommended by KIDA database (Wakelam et al. 2012 ,see Table 6.4). In Table 6.3 the open channels for the reactions between atomic oxygen and the two isomers are reported with their relative yields, as experimentally determined (Leonori et al. 2012 ; Balucani et al., in preparation).

We want to point out that, at this stage, we do not distinguish between the two C_3H_3O isomers, CH_3CCO (for the case of methylacetylene) and CH_2CCHO (for the case of allene); however we plan to investigate their chemistry in a future work.

In Table 6.3, the main dissimilarity is that, in the case of allene, the channel for the formation of CO dominates with a BR of 81.5%, while the BR of the reaction producing carbon monoxide from methylacetylene is only 68% (Balucani et al., in prep.). The other channels contribute to a minor extent, especially in the case of the O + CH_2CCH_2 reaction.

6.2 Chemical modelling

We investigated how the new reaction networks included in the model affect the hydrocarbon abundances by running simple models at typical densities for the ISM in the 10^2–10^6 cm^{-3} range; in particular, we simulate the case of an unphysical cloud at 10 K and constant density where we do not account for any freeze-out reaction during the collapse phase. We plot the fractional abundances obtained as outputs from these test models for C_2H_2, C_2H_4 and the two C_3H_4 isomers as a function of the density of the cloud at 5×10^5 years (see Figure 6.1). In order to highlight the changes in the hydrocarbon abundances, we run models with the same physical parameters as described above but including the same chemistry as in the UMIST 2006 database. In other words, the differences observed are only due to the new reaction scheme (which is not included in the UMIST 2006 database) with all the other parameters kept constant.

In the first two panels of Figure 6.1, starting from the left, we report a comparison between the hydrocarbon fractional abundances (with respect to the total number of hydrogen atoms) from the original version of the code (blue line) and the ones from the models containing the revised chemistry (green and red lines) at selected density values. In the case of C_3H_4, the blue line refers to the output obtained with the same chemistry as

Table 6.4. Paths of formation for C_3H_5, CH_3CCH and CH_2CCH_2 based on data from KIDA database (Wakelam et al. 2012).

Reaction	α	β	γ
$H + CH_3CHCH_2 \rightarrow C_3H_5 + H_2$	4.47×10^{-13}	2.50	1250
$C_2H_5 + CH_3CHCH_2 \rightarrow C_3H_5 + C_2H_6$	2.01×10^{-11}	0	0
$C_2H_3 + CH_3CHCH_2 \rightarrow C_3H_5 + C_2H_4$	1.72×10^{-15}	3.50	2360
$CH_2 + CH_3CHCH_2 \rightarrow C_3H_5 + CH_3$	2.70×10^{-12}	0	2660
$CH_3 + C_2H_3 \rightarrow C_3H_5 + H$	1.20×10^{-10}	0	0
$CCH + CH_3CHCH_2 \rightarrow C_3H_5 + C_2H_2$	2.40×10^{-10}	0	0
$C_3H_5{}^+ + NH_3 \rightarrow CH_3CCH + NH_4{}^+$	9.00×10^{-10}	0	0
$C_2H_6 + CH_2CCH \rightarrow CH_3CCH + C_2H_5$	5.83×10^{-14}	3.30	9990
$CH_4 + CH_2CCH \rightarrow CH_3CCH + CH_3$	1.74×10^{-14}	3.40	11700
$H_2 + CH_2CCH \rightarrow CH_3CCH + H$	1.42×10^{-13}	2.38	9560
$C_2H_3 + C_3H_5 \rightarrow CH_3CCH + C_2H_4$	4.00×10^{-12}	0	0
$CH_3 + C_3H_5 \rightarrow CH_3CCH + CH_4$	4.03×10^{-13}	0.32	-66
$CCH + CH_3CHCH_2 \rightarrow CH_3CCH + C_2H_3$	2.00×10^{-11}	0	0
$OH + C_3H_5 \rightarrow CH_3CCH + H_2O$	1.00×10^{-11}	0	0
$H + C_3H_5 \rightarrow CH_3CCH + H_2$	3.00×10^{-10}	0	0
$^aCH + C_2H_4 \rightarrow CH_3CCH + H$	7.80×10^{-11}	0	0
$C_3H_5 + C_3H_5 \rightarrow CH_2CCH_2 + CH_3CHCH_2$	1.40×10^{-13}	0	-132
$C_2H_6 + CH_2CCH \rightarrow CH_2CCH_2 + C_2H_5$	5.83×10^{-14}	3.30	9990
$CH_4 + CH_2CCH \rightarrow CH_2CCH_2 + CH_3$	1.74×10^{-14}	3.40	11700
$H_2 + CH_2CCH \rightarrow CH_2CCH_2 + H$	1.42×10^{-13}	2.38	9560
$C_2H_3 + C_3H_5 \rightarrow CH_2CCH_2 + C_2H_4$	2.00×10^{-12}	0	0
$CH_3 + C_3H_5 \rightarrow CH_2CCH_2 + CH_4$	4.03×10^{-13}	0.32	-66
$H + C_3H_5 \rightarrow CH_2CCH_2 + H_2$	3.30×10^{-10}	0	0
$^aCH + C_2H_4 \rightarrow CH_2CCH_2 + H$	3.12×10^{-10}	0	0

[a] α is evaluated by the product between the ratio for each reaction channel (Zhang et al. 2012) and the total rate constant of 3.9×10^{-10} cm^3 mol^{-1} s^{-1}.

in the UMIST 2006 database (that does not distinguish between the two isomers), while the green line and the red line are the results for CH_3CCH and CH_2CCH_2, respectively, produced with our updates.

In general, in the absence of freeze-out, for each selected density we obtain very low amounts of all species and a resulting negligible discrepancy between the hydrocarbon fractional abundances between the two networks; the only exception is C_2H_2, where we highlight differences of more than an order of magnitude between the acetylene abundances, depending on the density value chosen. We therefore run a model at higher temperatures to test if the effects of our updates are more evident at 300 K. Figure 6.2 shows the results from this second test. In order to quantify the impact of the new reaction scheme on the hydrocarbon chemistry, we need to make a comparison between their theoretical

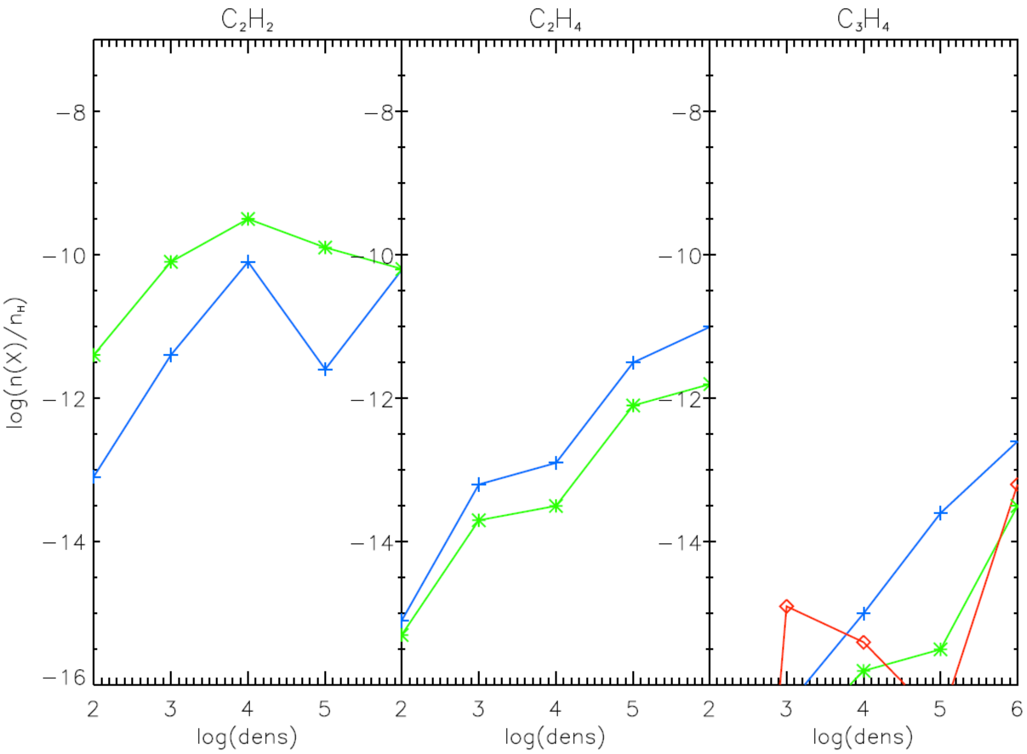

Figure 6.1. The fractional abundances (with respect to the total number of hydrogen nuclei) of selected species at 10^6 years and at specific density values when the temperature is kept at 10 K. Starting from the left, the results for C_2H_2, C_2H_4 and both isomers of formula C_3H_4 are shown. In the first two cases, the green line represents the outputs from the model with the updates and the blue line those from the original version of the code. In the third panel from the left, the green line represents the methyl acetylene abundance and the red line is the abundance of allene, while the blue line refers to the two isomers that were undistinguished in the UMIST 2006 database.

column densities and those from the observations. Unfortunately, the values obtained for the fractional abundances of all the species in Figure 6.2 are still too low to allow us a comparison between their theoretical and observed coloumn densities, although we certainly observe an increase in all the hydrocarbon abundances in the version of the code where the new reaction scheme is included. On the other hand, the greater abundances of C_2H_2 obtained with the revised reaction scheme (mainly at high densities) are already enough to prompt us to investigate the causes of such changes.

We emphasise that with this kind of comparison we are only analysing the effect of the new schemes on the hydrocarbon abundance prediction. We wish to stress that all the updated reactions are characterised by a certain activation energy and, therefore, their

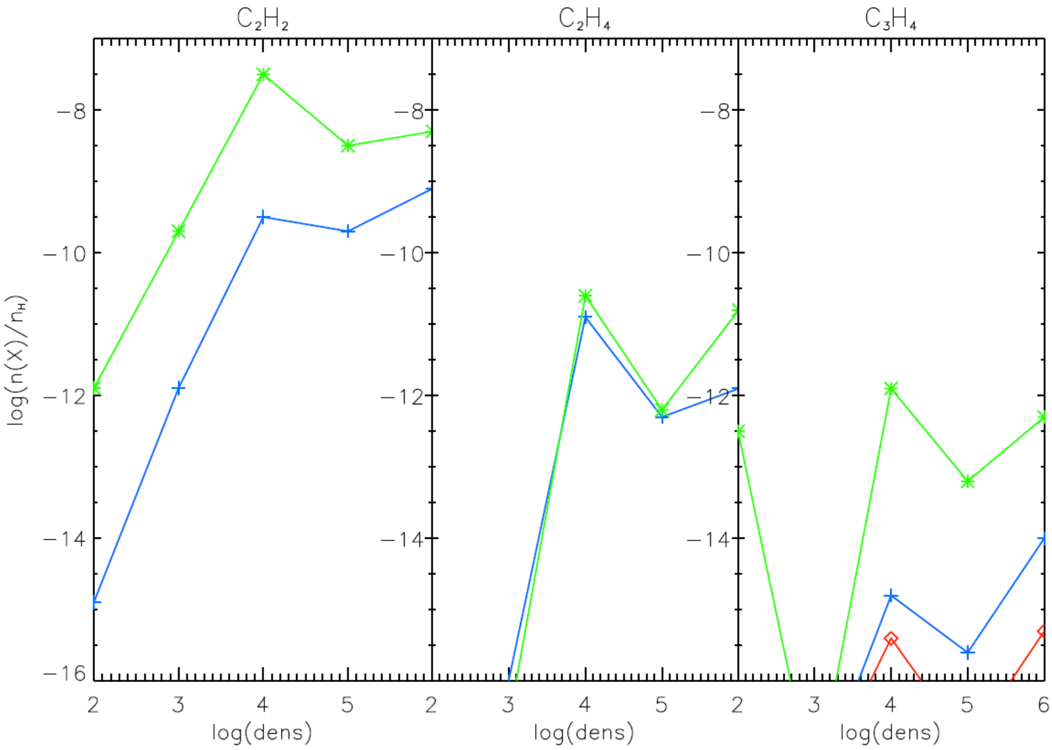

Figure 6.2. The fractional abundances (with respect to the total number of hydrogen nuclei) of selected species at 10^6 years and at specific density values and at 300 K. Starting from the left, the results for C_2H_2, C_2H_4 and both isomers of formula C_3H_4 are shown. In the first two cases, the green line represents the outputs from the model with the updates and the blue line those from the original version of the code. In the third panel from the left, the green line represents the methyl acetylene abundance and the red line is the abundance of allene, while the blue line refers to both isomers that were undistinguished in the UMIST 2006 database.

rate coefficients are very small at temperatures between 10–200 K. Nevertheless, they make a significant contribution in controlling the abundances of unsaturated hydrocarbons probably because of the large abundance of atomic oxygen.

In order to understand the real influence of oxygen in the hydrocarbon chemistry, we modelled four different astronomical regions: a diffuse cloud, a translucent cloud, a dark cloud and a hot core. The following section describes the models in more detail.

6.2.1 Modelling of different astrochemical environments

Table 6.5 lists the physical parameters used for our modelling. For each astronomical source we run two models: we employ a rate file with the same chemistry as in the UMIST 2006 database and another one with the revised chemical network proposed in the present

Table 6.5. List of physical parameters for the different models: visual extinction (A_v), density (`df`), gas temperature (T), efficiency of the freeze-out (`fr`) during Phase I (the percentage of mantle CO (mCO) given by the freeze-out parameter at the end of Phase I of the chemical model).

	A_v [mag]	df [cm^{-3}]	T [K]	`fr` [%]
1. Diffuse cloud	0–1	1×10^2	100	0
2. Translucent cloud	1–5	1×10^3	20	0
3. Dark core	5–10	1×10^4	10	∼40
4. Hot core	∼500	1×10^7	300	∼98

study.

We start by considering the case for a diffuse cloud (Model 1), a quite extended low density (10^2 cm^{-3}) region permeated by the ultraviolet interstellar radiation field; temperatures go up to 100 K and the visual extinction is around 1 mag. Due to their relatively low-visual extinction diffuse clouds are dominated by photodissociation reactions and there is no chemistry occurring on the grain surfaces.

As for the case of a diffuse cloud, atoms and molecules do not freeze onto the dust for a translucent cloud (Model 2) either; a translucent cloud is an intermediate phase (in terms of physical conditions) between the diffuse and the dense medium (van Dishoeck 2000); the fact that they are called *translucent* is due to the presence of a bright star in their proximity that allows absorption lines to be observed. Translucent clouds are relatively cold regions (20–50 K) where densities can reach values up to 10^3 cm^{-3} although there is no evidence of a collapsing core inside these objects. Since translucent clouds can be penetrated by radiation (their A_v is between 1 and 5 mag), their chemistry is also affected by photoprocesses. Diffuse and translucent clouds are two examples of low-density interstellar regions.

We also explore the case for high-density sources, such as dark and hot cores, where a grain surface chemistry is included in order to simulate the isothermal collapse phase during which atoms and molecules freeze onto the surfaces of dust and new species can be produced. This process is more efficient during the formation of a hot core (a very compact object characterised by densities $\geq 10^6$ cm^{-3}, Model 4) than for the case of a dark core (Model 3) where densities increase only up to 10^4 cm^{-3}. For the case of a hot core, moreover, we need to model a second phase that describes all the heating effects that could induce molecules to thermally desorb (indeed temperatures rise up to 200–300 K);

for a dark core we only account for the non-thermal desorption of species (for more details see Chapter 2) efficient already at 10 K.

6.3 Results and discussion

We discuss our results only for the case of a hot core (Model 4). Results obtained as outputs from Models 1, 2, 3 show only small differences in the abundances of the species involved, and the resulting abundances for our selected hydrocarbons are in all cases below the observational thresholds. Concerning the hot core model, in order to simulate the warm-up of icy mantles and the consequent sublimation of molecules from their surfaces, we allow a time-step desorption of species as described in Viti et al. (2004) which is based on the laboratory data obtained from temperature programmed desorption experiments by (Collings et al. 2004 , briefly described in Chapter 1). C_2H_2 and C_2H_4 were classified as intermediate between CO-like and H_2O-like species. Intermediate molecules were found in the hydrogenated ice layer although they were also able to escape via monomolecular desorption because of their moderate interaction with water ice. Since the two C_3H_4 isomers have a low dipole moment (∼0.8 D), we assumed for them a similar behaviour, classifying methylacetylene and allene as intermediate species.

We analyse the outputs for the hydrocarbon abundances as well as the trends for the abundances of other species involved in the updated oxygen chemistry during the warm-up phase (see Figure 6.3).

In particular, we focus on the small counterparts such as CH_2, CH_3, HCO and H_2CO that have been detected as products of dissociation for all the hydrocarbon species considered. While it is difficult to determine the percentage contribution of each reaction channel to the abundances of all hydrocarbons, UCL_CHEM provides us with an analysis of the percentage of destruction and formation pathways for any selected species and we can therefore draw some conclusions on the trends displayed in Figure 6.3. For instance, C_2H_2 is mainly formed in the reaction between H_2O and $C_2H_3^+$; on the other hand one of his major destruction routes is the formation of $C_2H_3^+$ after interaction with H_3^+. This loop of reactions keeps the fractional abundance of acethylene approximately constant (within an order of magnitude) during the entire warm-up phase. Other loss pathways for C_2H_2 are the production of HCCO and CO in the reactions with oxygen atoms. C_2H_4 is primarily produced by CH and CH_4 and destroied by the reactions with oxygen atoms; in particular,

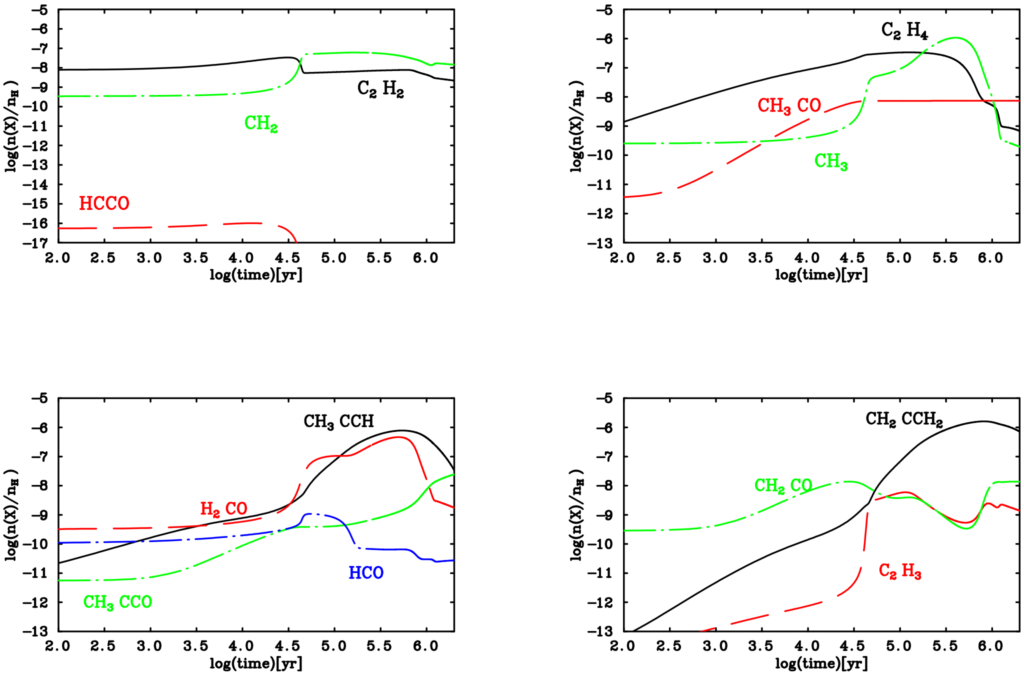

Figure 6.3. The fractional abundances (with respect to the total number of hydrogen nuclei) for selected species as a function of time during the warm-up phase.

the dominant loss channels lead to the formation of HCO, CH_3 and CH_2CHO. Ethylene also represents the main reactant for the synthesis of allene and methylacetylene and this fact explains the decrease in the ethylene fractional abundance (see Figure 6.3) where the two C_3H_4 isomers show a peak in their abundance profiles (between $10^{5.5}$ and 10^6 years). Finally, since we classified all the hydrocarbons as intermediate species, we observe their evaporation occurring between 10^4 and 10^5 years because of the volcano effect ($\sim$90 K) and co-desorption with water ice ($\sim$100 K; see Figure 6.4).

In order to validate the revised hydrocarbon chemistry, we evaluate the column densities (by the end of our simulations, at $10^{6.5}$ years) for most of the species involved and we compare our theoretical values with those from observations towards hot cores. The

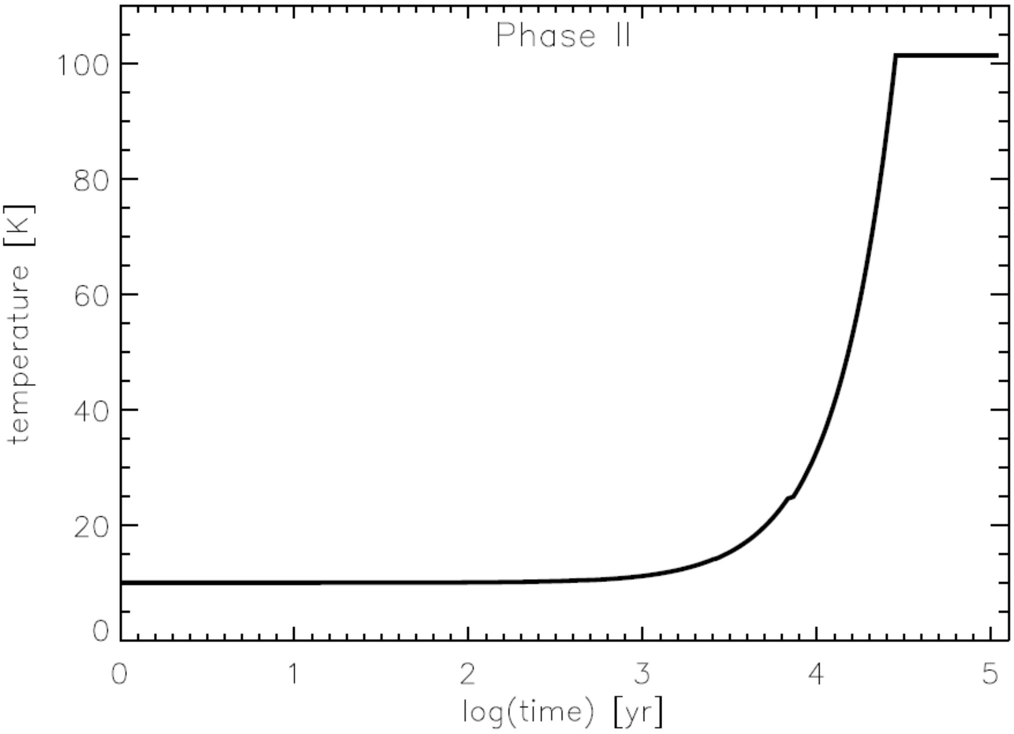

Figure 6.4. Temperature profile as a function of time during Phase II.

column densities (in cm^{-2}) for a generic species Y are estimated by the approximation:

$$N(\mathrm{Y}) \sim X(\mathrm{Y}) \times A_{\mathrm{v}} \times (n(H) + 2n(H_2)), \tag{6.1}$$

where X is the fractional abundance of the species Y, A_{v} is the visual extinction and $n(H)+2n(H_2)$ is the column density of hydrogen that provides 1 mag of extinction, equal to 1.6×10^{21} cm^{-2}, as in previous chapters. We also calculate the column densities obtained by the models without the new chemistry.

Results are shown in Table 6.6. We observe that for all the molecules listed in the table, except CH_3, the abundances obtained as outputs from the updated version of the code are one order of magnitude higher than those evaluated from its original version.

Hydrocarbons have been found across different astrochemical environments, from planet atmospheres to dark clouds, in the Milky Way as well as towards other Galaxies (Pendleton 2004). One of the first hydrocarbon detections was made by Ridgway et al. (1976), who observed CH_4 and C_2H_2 towards the carbon star IRC + 10216, where a few years later

Table 6.6. Comparison between observational and theoretical column densities (in cm^{-2}) for selected species towards various hot cores. Starting from the left, the second column shows results from the original version of the code; in the third column we report the molecular column densities calculated after our updates by the end of our simulations ($10^{6.5}$ years).

Molecule	Original	Revised	Observations	Source	References
C_2H_2	2.70×10^{15}	4.08×10^{14}	5.50×10^{14}	SgrA	Lacy et al. (1989)
C_2H_4	1.93×10^{13}	1.26×10^{14}	-	-	-
CH_3CCH	1.11×10^{15}	6.18×10^{15}	1.20×10^{15}	Orion-KL	Wang et al. (1993)
CH_2CCH_2	not present	1.78×10^{16}	-	-	-
CH_2	2.09×10^{15}	4.88×10^{14}	6.60×10^{13}	Orion-KL	Hollis et al. (1995)
CH_3	2.70×10^{15}	7.73×10^{13}	8.00×10^{14}	SgrA	Feuchtgruber et al. (2000)
HCCO	not present	$4.68\times10^{\;3}$	-	-	-
CH_2CO	4.25×10^{14}	2.55×10^{15}	1.00×10^{14}	SgrB2	Turner et al. (1977)
HCO	5.62×10^{12}	5.13×10^{12}	1.03×10^{12}	W3	Snyder et al. (1976)
H_2CO	6.55×10^{14}	1.85×10^{14}	8.32×10^{14}	Orion-KL	Wright et al. (1996)
CH_3CO	not present	9.13×10^{14}	-	-	-
CH_3CCO	not present	5.80×10^{15}	-	-	-
C_2H_3	5.44×10^{13}	1.30×10^{13}	-	-	-

Betz (1981) found C_2H_4 with a column density of 10^{16}–10^{17} cm^{-2}.

Hydrocarbons were predicted to be abundant in the ISM but many of them were not observed at millimeter wavelengths because their symmetry forbids dipole rotational transitions. Some of the species listed in Table 6.6 have indeed not been detected towards hot cores yet, but since their column densities are in the 10^{13}–10^{15} cm^{-2} range we expect detections to be forthcoming.

A comparison between our theoretical results and data taken from the observations highlights a general agreement within an order of magnitude (with the exception of CH_2CO); in particular, after our updates, we achieve a greater match with the observed column densities of C_2H_2 and CH_2 than if we had used the chemistry in the UMIST 2006 database alone. Concerning the two C_3H_3O isomers, we only calculate an upper limit in their column densities since we do not account for a complete reaction network for their loss mechanisms. We would also like to stress that we have only qualitatively modelled a hot core without looking at a specific high-mass source, therefore our theoretical column densities could be refined.

6.4 Conclusions

In this study we have presented how a revised gas phase chemical network featuring the reactions of atomic oxygen with several unsaturated hydrocarbons affects the abundances of simple organic species in the ISM. We mostly focus on the modelling of hot ISM regions where these variations were found to be more evident; however colder regions such as diffuse and translucent clouds or a dark core have also been investigated. A first conclusion is that in hot cores/corinos atomic oxygen easily degrades unsaturated hydrocarbons directly to CO or to its precursor species (such as HCCO or HCO) and destroys the double or triple bond of alkenes and alkynes. Therefore, environments rich in atomic oxygen at a relatively high temperature are not expected to be characterised by the presence of large unsaturated hydrocarbons or polycyclic aromatic hydrocarbons. On the contrary, in O-poor and C-rich objects, hydrocarbon growth can occur to a large extent. In colder objects, the effect of the reactions of atomic oxygen with small unsaturated hydrocarbons is reduced because of the presence of a small activation energy for these reactions.

Moreover we highlight the main contribution from other reaction channels that are not yet included in the available databases: ketyl and vinoxy radicals are among the new significant species that should be considered in the modelling. New attempts to detect them should be pursued and a chemical scheme for the loss pathways of the vinoxy radical devised.

Furthermore, we have established that structural isomers, such as methylacetylene and allene, should be treated separately when they manifest a different chemical behaviour.

A more general conclusion is that, if we wish to fully understand the formation of the numerous organic species detected in ISM, the intricate chemistry that leads to their formation should be treated in detail.

We finally plan to refine our theoretical results by modelling specific sources where hydrocarbons have been found. In the present study we calculated column densities of hydrocarbons that match those from the observations to within an order of magnitude although we were unable to make a comparison for all the species considered: most hydrocarbons are indeed non-polar molecules and therefore they cannot be detected through rotational emission. Despite this constraint, we aim to estimate the column densities for the case of symmetric hydrocarbons based on the abundances of their derivative species; for instance, as already stated by Quan & Herbst (2007), the amount of allene in a source should be related to the abundance of its derivative cyanoallene that, contrary to allene, is detectable.

The present Chapter highlights the importance of keeping our treatment of gas phase chemistry current, despite the flood of interest that nowadays is addressed to gas-grain reactions.

The following Chapter returns to surface chemistry, but we direct our attention to the products (formed on the grains) that, once sublimated to the gas phase, may contain important clues to understanding the molecular complexity and the variety of interactions occurring on the icy mantles.

Chapter 7

What form does sulfur take on the grain surface?

The present chapter aims to shed light on the form that sulfur takes inside icy mantles by introducing an updated network of reactions occurring on the grain surface, and based on recent experimental and theoretical results.

The interest in the form of sulfur on mantles is due to the fact that, in the gas phase, it is a ubiquitous element: it has been detected in different astronomical environments, from the diffuse medium (Liszt 2009) to dark clouds (Dickens et al. 2000), as well as in hot cores and hot corinos (Schöier et al. 2002; Sutton et al. 1995); in comets (Boissier et al. 2007); and in the atmosphere of Venus (Krasnopolsky 2008), in various chemical forms.

Many observations have therefore been performed. For instance, Jenkins (2009) observed atomic sulfur lines towards the diffuse medium and showed a relationship between the amount of depletion of the elements and the density of the cloud. Herpin et al. (2009) focused their studies on four different samples of high and low-mass star forming regions. By observing OCS, H_2S, SO, SO_2 and CS, they classified the high-mass clump W43-MM1 as the youngest object, followed by the low-mass star IRAS 18264-1152, IRAS 05358+3543 and IRAS 18162-2048.

In Table 7.1 we report all the sulfur-bearing species that have been, to date, detected in the ISM, organised according to the year of their discovery.

Table 7.1. List of sulfur-bearing species with the sources where they were observed. References are provided in the third column.

Molecule	Source	Reference
CS	Hot cores/corinos	Penzias et al. (1971)
OCS	SgrB2	Jefferts et al. (1971)
HCS^+	SgrB2, Orion	Thaddeus et al. (1981)
H_2S	Hot cores	Thaddeus et al. (1972)
H_2CS	SgrB2	Sinclair et al. (1973)
SO	Orion A	Gottlieb & Ball (1973)
SO_2	Orion A	Snyder et al. (1975)
SiS	IRC+10216	Morris et al. (1975)
NS	SgrB2	Gottlieb et al. (1975); Kuiper et al. (1975)
CH_3SH	SgrB2	Linke et al. (1979)
HNCS	SgrB2	Frerking et al. (1979)
C_2S	TMC-1, SgrB2, IRC+10216	Saito et al. (1987); Cernicharo et al. (1987)
C_3S	TMC-1, SgrB2	Kaifu et al. (1987); Yamamoto et al. (1987)
SO^+	IC 4434	Turner et al. (1992)
HSCN	SgrB2(N)	Halfen et al. (2009)
SH^+	SgrB2	Menten et al. (2011)
HS	W49N	Neufeld et al. (2012)

Additionally, the importance of sulfur-bearing species is linked to the fact that they may act as evolutionary tracers for a specific region. In an attempt to study this potential role, Charnley (1997) proposed SO/H_2S and SO/SO_2 ratios as molecular clocks for mantle disruption since they seemed to change along with different astronomical objects: dark clouds, hot cores, shocks and winds around protostars and also within individual star-forming regions. He suggested hydrogen sulfide (H_2S) as starting point for sulfur chemistry in the gas phase, as shown in reaction 7.1.

$$H_3O^+ + H_2S \rightarrow H_3S^+ + H_2O \tag{7.1}$$

The presence of H_2S had already been detected towards the Orion Hot Core with a fractional abundance of 10^{-8}, in other hot cores (X(H_2S)= 10^{-8}–10^{-7}) and also in the Orion Plateau by Minh et al. (1990). The subsequent dissociative recombination of reactive sulfur, H_3S^+, produces HS that reacts with H or O to form atomic sulfur or SO, respectively. Two factors were found to influence sulfur chemistry:

i) the gas phase metallicity: if it is high, there will be less H_3O^+ available for reaction 7.1;

ii) the amount of O_2 and other reactive species like O and OH, which in turn depends upon the core temperature (for instance see the competitive channel in reaction 7.2).

Another sulfur species that is predicted to form at all temperatures is CS; three different mechanisms were suggested for its production:

$$\mathrm{SO + C \rightarrow CS + O}, \tag{7.2}$$

(this reaction competes with O_2 + C → CO + O),

$$\mathrm{HCS^+ + e^- \rightarrow CS + H}, \tag{7.3}$$

(where HCS^+ is produced by H_2S + C^+), and

$$\mathrm{H_3CS^+ + e^- \rightarrow CS + H + H_2}. \tag{7.4}$$

On the other hand, CS is destroyed by O to form CO + S that associate to produce OCS. This species has been detected towards the embedded protostar W33A (Palumbo et al. 1995) and it is believed to be formed in icy mantles in dense environments. Alternative paths for the formation of this molecule are the following:

$$\mathrm{HOCS^+ + e^- \rightarrow OCS + H} \tag{7.5}$$

and

$$\mathrm{O + HCS \rightarrow OCS + H}. \tag{7.6}$$

Destruction mechanisms of OCS occur in the presence of HCO^+ and $H_3{}^+$, producing $HOCS^+$, which restarts the cycle of reactions.

At higher temperature another species is detected: H_2CS, and its amount depends upon the availability of sulfur that interacts with CH_3.

Beside this gas phase chemistry, sulfur species are involved in several interactions occurring on grain surfaces. However, the nature of such interaction is not well known (see details in Section 7.1). Models that include both gas phase and grain surface reactions have been developed in recent years and some important considerations have been derived about the role of sulfur as a possible clock for the evolutionary age of different cores.

Charnley (1997) developed two gas-grain models for Sgr B2M and the Orion Compact

Ridge in order to compare his theoretical results with observations. For the case of Sgr B2M, he found a good agreement for OCS, CS and SO abundances in the model without O_2 injection from grains. By considering O_2 injection he was able to reproduce only the abundance of H_2S at 1.6×10^3 years and 200 K. Concerning the Orion Compact Ridge, SO and SO_2 abundances were well reproduced and they were not affected by the introduction of O_2. On the other hand, when O_2 was considered in the model, they showed lower abundances than those observed.

Despite the inconsistency highlighted by Charnley (1997), Hatchell et al. (1998) followed the idea to constrain the core ages by looking at the ratios of sulfur-bearing species towards ultra compact HII regions. In particular, they developed different chemical models for each of the eight sources they investigated, by varying the following three parameters:

- gas densities: 2×10^5–2×10^7 cm^{-3}
- temperatures: 50–300 K
- cosmic-ray rates: 1.3×10^{-17}, 1.3×10^{-16}, 1.3×10^{-15} s^{-1}.

Temperatures and cosmic-ray rates were shown to have the greatest effects on the sulfur-bearing species abundance. With the exception of OCS (for which the model predicted higher abundances compared to those observed), they found lower amounts of all the sulfur species with respect to their observed values, perhaps due to the influence of the chemistry of NH_3 (predicted to fall at similar timescales to H_2S) and CH_3CN (predicted to peak when there are H_2S, SO and SO_2 simultaneously). They classified the sulfur-bearing species along with the core ages:

- H_2S, SO in younger cores
- H_2S, SO, SO_2 at intermediate ages
- later, SO and SO_2 without H_2S
- finally, CS, H_2CS, OCS. For OCS, they suggested a route of formation on the grain surface.

A few years later, Viti et al. (2001) proposed the NS/CS and SO/CS ratios as specific indicators of a shock passage in the vicinity of a hot core; these shocks were attributed to a massive star which begins to irradiate the interstellar gas surrounded the core. In these physical conditions, the sulfur chemistry was found to be connected to those of the HCO/H_2CO ratio. High values of these ratios meant that a shock had occurred. In another paper, Hatchell & Viti (2002) compared their theoretical values for NS/CS with those from the observations for six different hot cores in order to verify whether these cores were shocked. They found that a shock had occurred whenever the production of NS was happening at late stages, because at early stages OH was preferentially used to form H_2O (instead of NS).

Wakelam et al. (2004) repeated the study by Hatchell et al. (1998) and highlighted how none of the ratios involving the four most abundant sulfur-bearing species (H_2S, OCS, SO and SO_2) can be useful by itself for estimating the core ages, because the amount of each molecule depends at least on the physical conditions, the adopted grain mantle composition and also the time. They therefore developed chemical models in which they assumed three different compositions of the pre-evaporative gas phase in order to investigate the influence of this parameter on the sulfur abundances. They also found a link between the sulfur chemistry and the amount of atomic oxygen in the gas phase: in particular, SO was found to be a product in several reactions involving O as one of the reactants.

The key issue in all of these studies seems to be the uncertainty related to the species that acts as the major sulfur reservoir on the grains in these astronomical environments. In a theoretical study, Ruffle et al. (1999) proposed that in collapsing translucent clouds sulfur is efficiently adsorbed onto grain mantles. Gas phase sulfur was found to exist in form of S^+, hence, since grains are negatively charged, sulfur is removed from the gas phase more rapidly than neutral species. Dimers and cyclic molecules like S_8 can also be dust grain components, as demonstrated by the most recent experiments involving UV-processing and sublimation of H_2S and H_2S:H_2O ice by Jiménez-Escobar & Muñoz Caro (2011). The authors aimed to reproduce the sulfur depletion towards dense clouds and in circumstellar regions, although, so far, the only S-bearing species firmly detected on grain surfaces has been OCS, with relatively low fractional abundances on the order of 10^{-7} (Palumbo et al. 1997). Codella et al. (2006) found indirect evidence of OCS as a significant reservoir of sulfur in grain mantles by modelling the presence of an eroding interface between a fast wind and a dense core. Ferrante et al. (2008) also investigated the mechanism of formation of OCS that seemed to be the reaction of CO with free S atoms produced by the fragmentation of the sulfur parent species. OCS was seen to be readily formed by irradiation, but at the same time it was easily destroyed after continued exposure. An alternative molecule, hydrated sulfuric acid, was suggested by Scappini et al. (2003) as the main sulfur reservoir and later Moore et al. (2007) produced this species by ion irradiation of SO_2 and H_2S in water-rich ice in the temperature range of 86–130 K.

Finally, a recent paper by Wakelam et al. (2011) reported the study of S-bearing species in four different sources in order to investigate the dependence of their abundances along with time. In their models species are allowed to deplete on grains and thermally and non-thermally evaporate but no reactions on grains are taken into account. Diffusion is also considered (see their paper for the details). They were unable to reproduce the observed abundances for OCS, SO, SO_2, H_2S and CS, but they found that the ratios between OCS/SO_2 and H_2S/SO_2 could be used to constrain some evolutionary timescales: they highlighted the difficulty in reproducing the CS amount, which was overestimated due to the fact that its abundance varies with radius such that there is an uncertainty about the location of the emission.

7.1 Update of UCL_CHEM with recent theoretical and experimental results

In this chapter we update the UCL_CHEM gas-grain chemical model to include some published and unpublished experimental and theoretical data on reactions involving S-bearing species occurring on icy mantle analogues. Our aim is to predict which are the best candidates for the sulfur reservoir. First of all, we summarise the results obtained from the different experiments and calculations (see Subsections 7.1.1, 7.1.2 and 7.1.3) and then we insert them into the chemical modelling. Hence, we run models to benchmark the difference that the new data make on the sulfur chemistry (see Section 7.2). We then run a grid of models covering a large parameter space to find trends in the variations of the fractional abundances of S-bearing species as a function of several physical parameters (see Subsection 7.2.1). A comparison between the theoretical and the observed column densities for each sulfur derivative is also performed (see Subsection 7.2.2).

7.1.1 The effect of cosmic-rays on icy H_2S mantle analogues

Cosmic-rays impinging on icy mantles are energetic enough to induce chemical and structural modifications on the grain surface. As a consequence the ice constituents differ from the gas phase composition, and experiments of astronomical interest are therefore the

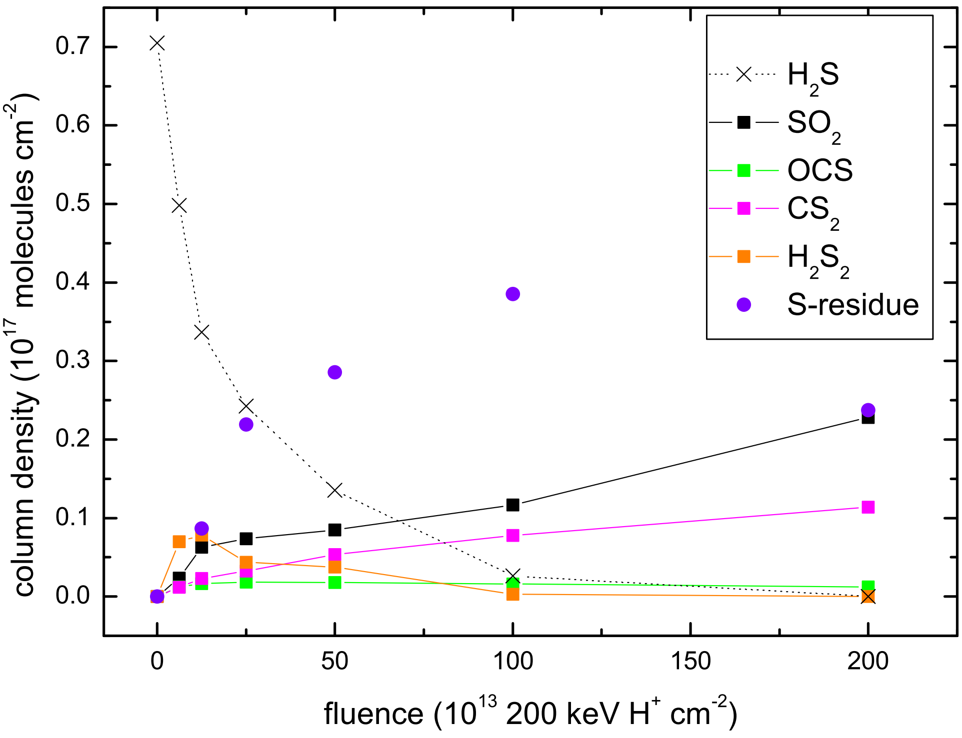

Figure 7.1. Column density of selected species as a function of ion fluence after irradiation of the ice mixture. Data have been provided by Prof. M. E. Palumbo.

only tools to provide us with information concerning the potential interactions that can arise after these dynamic impacts.

In order to simulate a flux of cosmic-ray particles, Garozzo et al. (2010) irradiated their sample with 200 keV protons at 20 K in a high-vacuum chamber (P $< 10^{-7}$ mbar). Their substrate consisted of a CO:H_2S=10:1 mixture. IR spectra were recorded before and after the bombardment in order to estimate the column densities for each species, N(X), calculated as the ratio with respect to the initial amount of H_2S, $N_i(H_2S)$, in the mixture. Figure 7.1 shows the decrease of the initial amount of hydrogen sulphide as the products of its dissociation form. The failure to detect H_2S in the solid phase (Ehrenfreund et al. 2004; Jiménez-Escobar & Muñoz Caro 2011) may therefore be linked to the strong ($\sim 80\%$) reduction in its column density when it is subjected to irradiation. This is in fact what was postulated in Codella et al. (2004) in order to justify the presence of a large amount

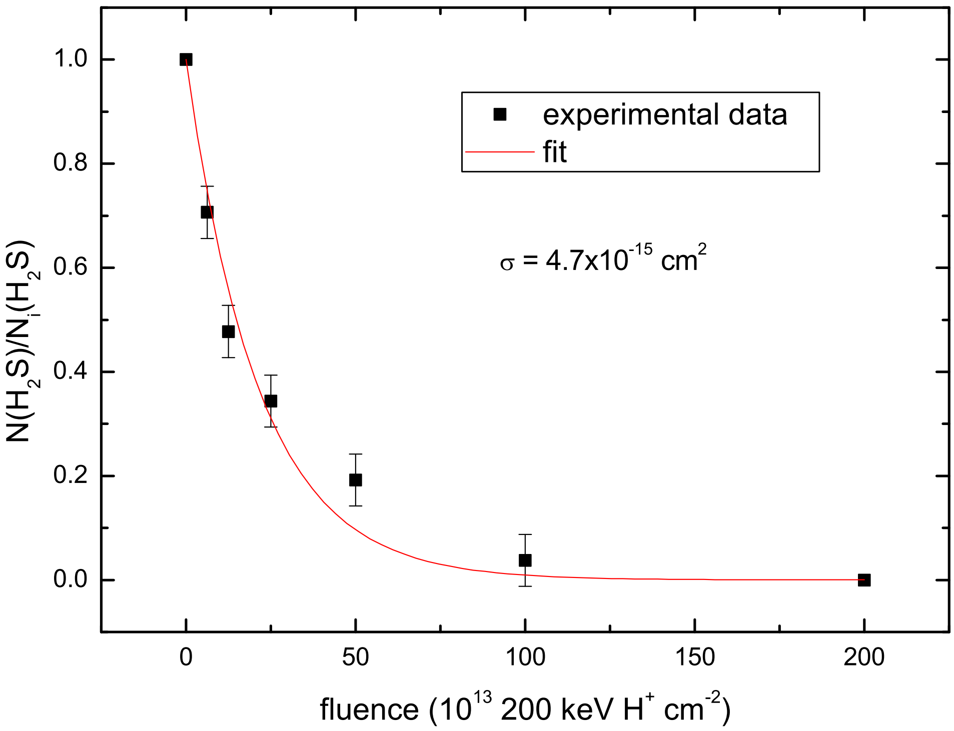

Figure 7.2. Column density ratio $N_i(H_2S)/N(H_2S)$ of hydrogen sulphide as a function of ion fluence after irradiation of the ice mixture. Data have been provided by Prof. M. E. Palumbo.

of OCS on the icy mantles. Experimental data were fitted with an exponential curve (as plotted in Figure 7.2) in order to evaluate the reaction cross section ($\sigma = 4.7\times10^{-15}$ cm^2). The identified molecules with their specific production rates relative to the ion fluence are listed in Table 7.2. The latter parameter was extrapolated by fitting the experimental data at low fluence with a straight line. The relevance of these experimental results derives from three main considerations:

1. A detection of CS_2 has not yet been made in the ISM. Laboratory data allow us to quantify this molecule and to extend our model to include a reaction scheme for its formation and loss channels.

Table 7.2. A List of the experimentally-detected sulfur-bearing species and their laboratory production rates depending on the ion fluence.

Molecule	p [cm^2]
H_2S_2	1.03×10^{-15}
SO_2	6.78×10^{-16}
CS_2	2.64×10^{-16}
OCS	2.05×10^{-16}
S-residue	1.19×10^{-15}

Table 7.3. Dissociation of solid H_2S due to cosmic-ray impact (CR) experimentally investigated by Garozzo et al. (2010). All the reaction channels are provided with a rate (in s^{-1}) of ISM relevance. The m before the molecular formula stands for *mantle*. Note that for all the reactions listed below the remaining solid hydrogen is implied.

Reaction			k [s^{-1}]
mH_2S +	CR	$\rightarrow$ mSres	2.20×10^{-16}
mH_2S +	mCO	$\rightarrow$ mOCS	3.80×10^{-17}
mH_2S +	mH_2S	$\rightarrow mH_2S_2$	1.90×10^{-16}
$2mH_2S$ +	mCO	$\rightarrow mCS_2$ + mO	4.89×10^{-17}
mH_2S +	2mO	$\rightarrow mSO_2$	1.25×10^{-16}

2. The evidence of a residue of species containing sulfur that can be estimated as follows:

$$\mathrm{N(S-residue) = N_i(H_2S) - N(H_2S) - N(SO_2) - N(OCS) - 2\times N(CS_2) - 2\times N(H_2S_2).} \tag{7.7}$$

   This residue provides a constant supply of sulfur and it may affect the role of sulfur as an evolutionary tracer.

3. These experiments help to predict the different forms that sulfur can take on the grain surface and to estimate the ratios among them.

We therefore insert in UCL_CHEM the chemical reactions experimentally investigated by Garozzo et al. (2010) and reported in Table 7.3. All the interactions occur in the solid state and, with the exception of the first channel, all the routes of loss of hydrogen sulphide are examples of two-body reactions. CR stands for cosmic-ray particles and it means that the hydrogen sulphide dissociation is catalysed by their impact on the surface.

The rate constants, k [s^{-1}], have been evaluated by the product of the reaction cross section (σ in cm^2) and the flux of cosmic ions (F$_{ISM}$ in cm^{-2} s^{-1}). To apply the laboratory results to interstellar medium conditions both quantities have been corrected using the following assumptions:

1. We consider a standard ionisation rate (ζ_{ISM}= 3×10^{-17} s^{-1}) and derive the flux of cosmic ions in the approximation of effective mono-energetic 1 MeV protons (Mennella et al. 2003): F$_{ISM}$= 0.5 ions cm^{-2} s^{-1}. F$_{ISM}$ must be regarded as an effective quantity: it represents the equivalent flux of 1 MeV protons which gives rise to the ionisation rate produced by the cosmic-ray spectrum if 1 MeV protons were the only source for ionisation.

2. Furthermore, we speculate that the cross section scales with the stopping power (S, the energy loss per unit path length of impinging ions). According to the SRIM code by Ziegler et al. (2008, see Section 3.1), in the case of protons impinging on a CO:H_2S mixture, S(200 keV protons)= 2.7×S(1 MeV protons).

In the case of hydrogen sulphide we define σ_{ISM}= σ/2.7 cm^2 and we derive a destruction rate of hydrogen sulfide equal to 8.7×10^{-16} s^{-1}. In the case of species formed after irradiation we define σ_{ISM}= p/2.7 cm^2 (see Table 7.2 for p values) and the calculated formation rates for each species are given in Table 7.3.

In our code the treatment of the grain surface reactions is adapted from a gas phase model. We therefore need the rate coefficients in units of cm^3 s^{-1}. Hence, we apply the same logic as in Subsection 3.2.2. In particular, we consider our reactions on the grain as examples of first order reactions where one of the reactants is in excess and it can therefore be included in the constant value. This means that the rate constant will depend only on the quantity of the second reactant. The concentration of molecules is set in terms of fractional abundances (unit-less), which we multiply by the gas density [cm^{-3}] in order to quantify our species in the three dimensional space. The insertion of experimental results in the modelling of ISM regions is a difficult task; for instance, the abundances of species vary with time and this implies that, when we scale our experimental rate for the concentration of the reactant in excess, we have to consider a different amount of that reactant at each time. For simplicity, we only account for the final abundance of the reactant in excess, although we run some tests using the initial concentration as well as some intermediate values in order to estimate the range within which our rates vary. For instance, when we consider CO as the most abundant reactant (this is the case of the second and the fourth reaction in Table 7.3), reaction rates cover six orders of magnitude because of the wide interval spanned by the CO abundances during the collapse phase of protostar formation. Density and freeze-out rate play a pivotal role in controlling the trends of the molecular abundances and since both of these two physical parameters only significantly change towards the end of the collapse, the abundances of species will also vary accordingly. We therefore refer only to the final abundance of CO in order to scale our reaction rates.

7.1.2 Laboratory investigations of solid OCS formation

In the experiments at the Cosmic Dust Laboratory (Department of Chemistry, University College London) reactants are co-deposited onto an highly ordered pyrolytic graphite (HOPG) substrate. During the dosing period, the substrate is held at a constant temperature, typically in the range 12–100 K; once the reactants are deposited, the material is allowed to cool to 12 K. Following the deposition, the sample is heated up to 200–300 K (depending on the system studied) during which time mass spectra are recorded. The result is an histogram of ion intensity as a function of ion m/z ratio (m stands for mass and z for the charge) and surface temperature. These experiments are repeated at different temperatures to give the dependence of the amount of product formed on the substrate during dosing.

Finally, a simple kinetic model is run to derive reaction barriers and Arrhenius pre-exponential factors from the temperature profile, allowing rate constants to be calculated. In particular, Ward et al. (2012) studied the following route for the formation of solid OCS:

$$\mathrm{mCS_2 + mO \rightarrow mOCS + mS}, \tag{7.8}$$

with CS_2 and O that are both adsorbed on the icy mantles. They found a rate constant of 1.34 $\times 10^{-20}$ cm^{-2}ML s^{-1} (where ML stands for *monolayer*).

Since our code accounts for reactions that occur in three dimensions (i.e. as gas phase reactions), we need to transform the surface rate constants from Ward et al. (2012) into standard units, cm^3 s^{-1}. We apply the same logic as in Section 4.1. Therefore, we first evaluate two quantities: the volume of ice per grain, which is equal to 2.6×10^{-13} cm^3, and the number density of grains. In the latter case, we obtain a grain number density of 3.8×10^{-5} cm^{-3}. We then use these two quantities to convert our rates per ML of ice to

Table 7.4. Routes of OCS formation on a coronene surface. α, β, γ represent the parameters for the rate coefficient. Data are taken from Adriaens et al. (2010).

Reaction	α [s^{-1}]	β	γ [K]
CO + S $\rightarrow$ OCS	1.66×10^{-11}	0	1893
CO + HS $\rightarrow$ OCS + H	1.66×10^{-11}	0	831

cm^3 of space (see Section 4.1 for the details of the calculations). Since the major partner in the ice mixture is water, we estimate the fraction of CS_2 ice compared to water ice in ISM conditions in order to avoid overestimating our rates; in other words, by dividing our rates by the ratio mCS_2/mH_2O, we consider that not all of the oxygen ice will react with the CS_2 ice because of the presence of other ice components (mainly water) in between. We, therefore, calculate a final value of the rate constant as 6.4×10^{-23} cm^3 s^{-1} at 20 K for the reaction between O and CS_2.

7.1.3 A theoretical study of OCS formation on the grain surface

The formation of carbonyl sulfide, OCS, was theoretically investigated by Adriaens et al. (2010) using density functional theory applied to a model of a coronene grain surface. DFT calculations were performed and benchmarked against high-level ab initio calculations to ensure the accuracy of the results. Values obtained for the reactions in the gas phase were compared to those estimated considering a coronene substrate in order to stress the catalytic effect driven by the presence of the surface in absorbing the energy excess.

We only focus on the reactions happening on the grains and in particular we introduce in our model the grain surface reactions occurring via a Langmuir-Hinshelwood mechanism (see Subsection 1.3.2), that was found to be the most probable in ISM conditions, as listed in Table 7.4. The rate parameters relative to each channel are also reported; γ represents the reaction barrier in units of Kelvin [K]. Note that, unlike Adriaens et al. (2010), we do not account for the formation of any species in the transition states and we do not distinguish among the different geometries of the reactants and the products.

The calculated adsorption energies turned out smaller in values than those experimentally determined in previous studies (Piper et al. 1984; Mattera et al. 1980) due to the fact that the theory considers a perfect coronene surface and neglects the weak physisorption interactions observable in the presence of substrate defects. Every reaction activation barrier given can therefore be seen as an upper limit to the effective barrier.

Table 7.5. Gas phase paths of OCS formation and destruction and their competitive routes. The α values are taken from Loison et al. (2012).

Reaction	α [$cm^3 mol^{-1} s^{-1}$]
$CH + SO \rightarrow OCS + H$	1.1×10^{-10}
$CH + SO \rightarrow SH + CO$	9.0×10^{-11}
$O + HCS \rightarrow OCS + H$	5.0×10^{-11}
$O + HCS \rightarrow SH + CO$	5.0×10^{-11}
$H + HCS \rightarrow H_2 + CS$	1.5×10^{-10}
$S + HCO \rightarrow OCS + H$	8.0×10^{-11}
$S + HCO \rightarrow SH + CO$	4.0×10^{-11}
$OH + CS \rightarrow OCS + H$	1.7×10^{-10}
$OH + CS \rightarrow SH + CO$	3.0×10^{-11}
$C + OCS \rightarrow CO + CS$	1.0×10^{-10}
$CH + OCS \rightarrow CO + CS + H$	4.0×10^{-10}
$CN + OCS \rightarrow CO + NCS$	1.0×10^{-10}

In order to incorporate the theoretical rates for OCS formation on grain surfaces in UCL_CHEM, we make the same assumptions as in Subsection 7.1.1, by considering an excess of CO (compared to the other reactants) and a first order equation for the evaluation of the reaction rates.

7.2 Incorporation of data into the model and results

In order to study the problem concerning the form of sulfur once it freezes onto the grain surface, we insert into our gas-grain network an extended chemistry for all the S-bearing species.

We start by setting the initial fractional abundance of gaseous S equal to 1.4×10^{-6} (see Chapter 2), although we ran a few test models to investigate the effect of having a lower (10^{-5}) or a greater value (10^{-7}) for this parameter. We then extend UCL_CHEM model to include the experimental and theoretical data on the solid state chemistry of sulfur-bearing species as explained in the Subsections 7.1.1, 7.1.2, 7.1.3.

Concerning the gas phase reactions, we update our network with new rate coefficients taken from the KIDA database (Wakelam et al. 2012). Moreover, we amend the rate parameters for different OCS routes of formation as described in Loison et al. (2012 , see Table 7.5).

We first investigate the influence of those updates on the sulfur chemistry. We therefore run various models that reproduce the physical conditions of a pre-stellar core at short

Table 7.6. Fractional abundances of selected sulfur-bearing species obtained as outputs from our code before (OLD) and after (NEW) our updates (see text for more details).

	Model	Version	S	CS	OCS	HS	H_2S
1	Protostellar core (young)	NEW	1.8×10^{-8}	1.5×10^{-9}	4.5×10^{-11}	2.6×10^{-12}	1.8×10^{-11}
		OLD	1.9×10^{-8}	1.4×10^{-9}	1.1×10^{-10}	2.4×10^{-12}	1.8×10^{-11}
2	Protostellar core (evolved)	NEW	7.9×10^{-10}	7.7×10^{-11}	4.2×10^{-11}	3.6×10^{-11}	9.9×10^{-12}
		OLD	9.6×10^{-10}	8.5×10^{-11}	3.8×10^{-11}	4.3×10^{-11}	1.4×10^{-11}
3	High-mass star	NEW	2.6×10^{-9}	9.5×10^{-8}	3.9×10^{-6}	1.2×10^{-8}	1.9×10^{-7}
		OLD	3.3×10^{-9}	5.9×10^{-8}	5.2×10^{-6}	4.0×10^{-10}	5.1×10^{-10}
4	Low-mass star	NEW	2.1×10^{-10}	4.2×10^{-10}	1.9×10^{-11}	1.6×10^{-11}	3.5×10^{-13}
		OLD	2.4×10^{-10}	4.3×10^{-10}	2.5×10^{-6}	1.2×10^{-13}	1.9×10^{-13}

	Model	Version	H_2S_2	SO_2	H_2CS	HCS
1	Protostellar core (young)	NEW	3.7×10^{-13}	3.5×10^{-11}	3.6×10^{-10}	2.6×10^{-15}
		OLD	3.6×10^{-13}	3.4×10^{-11}	3.6×10^{-10}	3.9×10^{-15}
2	Protostellar core (evolved)	NEW	1.4×10^{-12}	5.8×10^{-11}	1.1×10^{-10}	1.1×10^{-12}
		OLD	4.3×10^{-14}	7.2×10^{-11}	1.3×10^{-10}	2.5×10^{-11}
3	High-mass star	NEW	1.2×10^{-16}	2.6×10^{-6}	5.5×10^{-6}	3.6×10^{-9}
		OLD	4.8×10^{-9}	1.6×10^{-6}	5.7×10^{-6}	1.2×10^{-7}
4	Low-mass star	NEW	1.4×10^{-20}	7.4×10^{-6}	3.3×10^{-6}	2.4×10^{-11}
		OLD	1.3×10^{-11}	6.7×10^{-6}	3.5×10^{-6}	3.5×10^{-11}

(5×10^6 years, Model 1) and long (10^7 years, Model 2) timescales and of a high-mass (Model 3) and a low-mass (Model 4) star-forming region and we compare our new outputs (NEW) with those from our original version (OLD) of the code (see Table 7.6).

The main differences within each set of models are the temperatures and densities chosen. For the case of the pre-stellar core, we follow the collapse at 10 K with a final density of 10^5 cm^{-3}. Once the collapse ends, our simulation stops for Model 1, while it continues up to 5×10^7 years for Model 2. We also run two models that qualitatively simulate the formation of a high- and low-mass star characterised by a density of 10^7 cm^{-3} and 10^8 cm^{-3} and a temperature of 300 K and 100 K, respectively. For the case of Models 3 and 4, we also consider the thermal evolution of our pre-stellar core. As investigated by Viti et al. (2004), species can evaporate from the icy mantle in different bands of temperatures; in particular, they set H_2CS as a H_2O-like molecule that co-desorbs with the H_2O-ice when it starts to sublimate from the grain surface (at $\sim$ 100 K). On the other hand, the authors classified HCS, OCS, H_2S, SO_2 as intermediate species since they showed two peaks (due to volcano and co-desorption effects) in their TPD traces. After private conversations with Prof. W. A. Brown (who is currently performing TPD experiments of sulfur-bearing species), we set HS and H_2S_2 as intermediates between CO- and H_2O-like molecules.

Table 7.7. Observed fractional abundances of selected sulfur-bearing species towards dense regions. Data are taken from Herpin et al. (2009), except for HS (Neufeld et al. 2012) and H_2CS (Hatchell et al. 1998).

CS	OCS	HS	H_2S	SO_2	H_2CS
1.6×10^{-8}	1.3×10^{-8}	1.0×10^{-9}	4.0×10^{-10}	1.6×10^{-9}	1.0×10^{-9}

Looking at Table 7.6 we found that the changes in the sulfur chemistry considerably affect the abundances of some S-bearing species only in the cases of high- and low-mass star (Model 3 and 4, respectively) models, where the amount of H_2S_2 varies up to seven and nine orders of magnitude, respectively. Moreover, in Model 3, H_2S shows higher abundance of about three orders of magnitude and HCS and HS change by two orders of magnitude between the updated and the original version of our code. We also highlight fluctuations by two and five orders of magnitude in the fractional abundances of HS and OCS, respectively, in the outputs from Model 4. Results do not diverge significantly when we consider the chemistry of a prototypical pre-stellar core at early and late stages.

We therefore compare our theoretical abundances with those observed in order to verify the reliability of our new models; we focus on the data acquired for the case of a hot core source (Model 3) because of the greater amount of observations available. Note that not all the S-bearing species reported in Table 7.6 have been detected yet. Observations are reported in Table 7.7.

Although we highlight several agreements (within one order of magnitude) between the theoretical and observational results for each species, none of the models reproduces the observed amount for all the sulfur species; we therefore refine our results by looking at the sensitivity of the fractional abundances of species to different physical parameters and we verify the conditions needed for our theoretical results to match their corresponding observations.

7.2.1 Analysis of trends

We start by investigating the effect on selected S-bearing species abundances when different routes of freeze-out are considered. The grid of the freeze-out pathways chosen is reported in Table 7.8. We therefore run five models (one for each freeze-out chemistry) for a prototypical of high-mass star, with the physical parameters listed in Table 7.9.

The changes in the ice composition are more evident at the end of the collapse phase,

Table 7.8. Grid of possible paths of S-bearing molecules freeze-out. Note that we only report the S-bearing species involved in the different reaction routes.

Model	S→grains	H_2S_2→grains	CS_2→grains	HS→grains	CS→grains
F1	100% mS	100% mH_2S_2	100% mCS_2	100% mHS	100% mCS
F2	100% mH_2S	100% mH_2S+mS	100% mHCS+mHS	100% mH_2S	100% mH_2CS
F3	50% mH_2S 25% mOCS 25% mS	50% mH_2S+mS 50% mH_2S_2	50% mCS_2 50% mHCS+mHS	50% mH_2S 50% mHS	50% mHCS 25% mCS 25% mH_2CS
F4	10% mH_2S 5% mOCS 85% mS	20% mH_2S+mS 80% mH_2S_2	20% mCS_2 80% mHCS+mHS	20% mH_2S 80% mHS	10% mHCS 5% mCS 85% mH_2CS
F5	85% mH_2S 5% mOCS 15% mS	80% mH_2S+mS 20% mH_2S_2	80% mCS_2 20% mHCS+mHS	80% mH_2S 20% mHS	85% mHCS 5% mCS 15% mH_2CS

Table 7.9. Physical parameters for the model of a prototypical high-mass star.

Parameter	High-mass star model
`temp` [K]	10
`fr` [%]	98
`maxt` [K]	200
`size` [pc]	0.03
`dens` [cm^{-3}]	2×10^{2}
`df` [cm^{-3}]	1×10^{7}
`tfin` [years]	5×10^{6}
ζ [s^{-1}]	3×10^{-17}

when temperatures are as low as 10 K. Hence, in Figure 7.3, we plot the outputs obtained from the five models (F1–F5) at the end of Phase I; here, we consider the fractional abundances on the grain surfaces of selected S-bearing species.

First of all, it is evident that, regardless of the freeze-out chemistry chosen, H_2S is the most abundant species formed on the grain surfaces, with a fractional abundance of the order of 10^{-6}. F1 and F2 represent the two limiting cases where each species freezes as itself or it hydrogenates. By comparing the results from these two models, we find that some molecules, such as OCS, HS, H_2S, H_2S_2 and SO_2 do not seem to be significantly affected by these changes in their freeze-out routes. H_2CS forms slower in F2 on the icy mantles, although, at the end of Phase I, its abundance is similar to the one from F1. On the other hand, HCS is lower by about two orders of magnitude in F2; finally, S and CS undergo a sharp decrease in their abundances when conditions vary from F1 to F2.

In the intermediate cases (F3, F4, F5), where new S-bearing species can be formed on the icy mantles during the freeze-out, the fractional abundances of all of the species vary

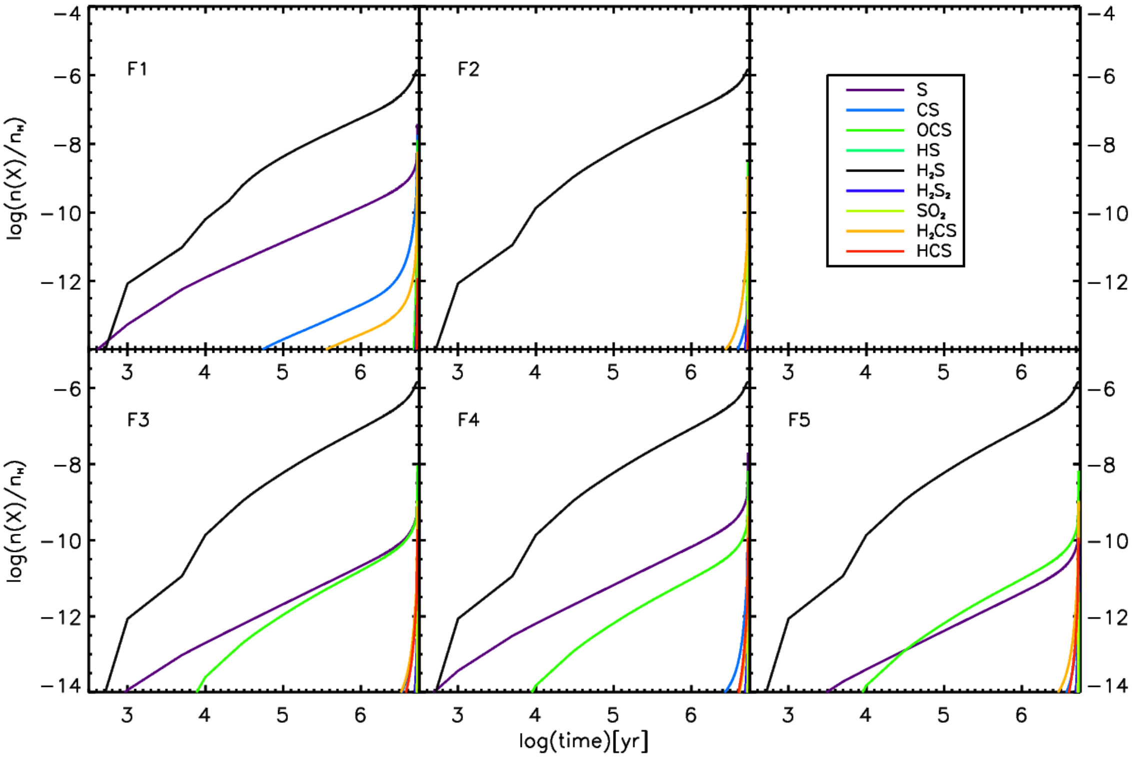

Figure 7.3. Fractional abundances of selected S-bearing species as a function of time when various freeze-out pathways are considered. Each graph refers to a different chemistry adopted (see Table 7.8 for more details).

within one order of magnitude or even less. From all the three combinations, we obtain a great amount of S, comparable to the abundance reached in the output from F1; moreover we observe a considerable amount of OCS ice, that now forms faster than in its outputs from F1 and F2.

We then look at the sensitivity of the abundances of our selected species to the different physical parameters of the core. In particular, we investigate the effects due to the core density at the end of the isothermal collapse in the 10^5–10^7 cm^{-3} range. We also explore how the predicted abundances vary with the cosmic-ray ionisation rate by choosing a standard interstellar (1.3×10^{-17} s^{-1}), an enhanced (1.3×10^{-16} s^{-1}) and a super-enhanced (1.3×10^{-15} s^{-1}) value for this parameter. Moreover, we vary the initial elemental abundance of sulfur to be either 1×10^{-6} (as in the previous study by Charnley 1997) or 3×10^{-5} (as in Wakelam et al. 2004) and we follow the evolution timescale up to 10^4 years (early stages) and 10^7 years (late stages). We repeat our sensitivity tests for each combination reported in Table 7.8, running 24 models for each freeze-out chemistry for a total of 120 models, which include Phase I and Phase II.

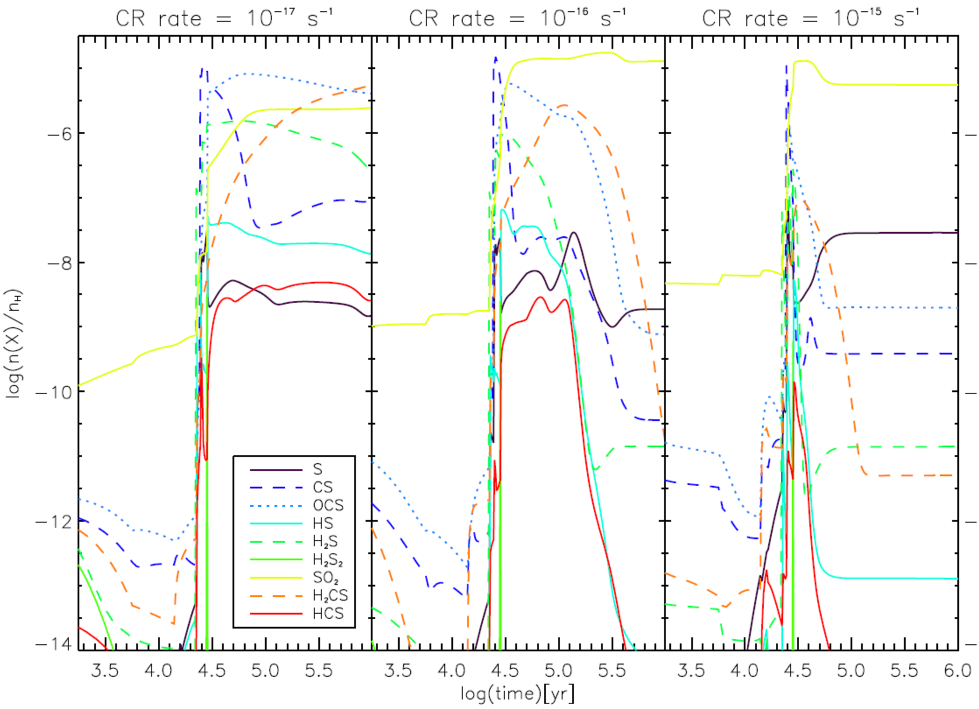

Figure 7.4. Fractional abundances of selected S-bearing species as a function of time for different cosmic-ray ionisation rates. Results refer to the abundances of species in the gas phase and at the end of Phase II, when the same chemistry as in F3 is employed. The panel on the left is the output obtained at the standard value for ζ; the central and the right panels show the results for an enhanced and a super-enhanced ζ, respectively.

With the exception of the cosmic-ray ionisation rate, all the explored physical parameters have relatively little effect on the chemistry of the S-bearing species considered and this confirms the results from a previous study by Hatchell et al. (1998). In contrast, the increase in cosmic-ray ionisation rate from the standard Galactic interstellar value to the super enhanced one significantly affects the final abundances of S-bearing species.

Figure 7.4 displays the evolution of the gaseous abundances of S-bearing species as a function of time (at the end of Phase II), for different cosmic-ray ionisation rates and a fixed freeze-out chemistry; note that we only show our outputs when the freeze-out routes in F3 are adopted, but we observe similar trends in the results from all of the remaining combinations. We found that the effect of changes in this parameter are particularly evident for the cases of HCS, H_2S_2 and H_2CS, which drastically drop when the rate at which molecules are processed by the cosmic-rays is the most efficient (1.3×10^{-15} s^{-1}).

Table 7.10. Theoretical fractional abundances for selected sulfur-bearing species in the gas phase at the end of Phase II with the same freeze-out chemistry as in F3 and comparison with observations.

	S	**CS**	**OCS**	**HS**	**H_2S**
Modelling	2.6×10^{-9}	9.5×10^{-8}	3.9×10^{-6}	1.2×10^{-8}	1.9×10^{-7}
Observations		1.6×10^{-8}	1.3×10^{-8}	1.0×10^{-9}	4.0×10^{-10}
	H_2S_2	**SO_2**	**H_2CS**	**HCS**	
Modelling	1.2×10^{-16}	2.6×10^{-6}	5.5×10^{-6}	3.6×10^{-9}	
Observations		1.6×10^{-9}	1.0×10^{-9}		

7.2.2 Observations and theoretical results

We briefly compare out theoretical fractional abundances, obtained after the sensitivity tests, with those from the observations listed in Table 7.7. For our purpose, we adopt the model with a standard cosmic-ray ionisation rate and setting the same freeze-out pathways as in F3 (Table 7.8). Results are reported in Table 7.10.

The theoretical and observed fractional abundances of CS and HS agree within an order of magnitude; the OCS abundance differs by two orders of magnitude, and the observed H_2S is lower by three orders of magnitude than its theoretical abundance. We also found a greater amount of H_2CS and SO_2 compared to their detected values. Note that in order to theoretically reproduce the observed abundance of H_2CS, keeping the same freeze-out percentages, an enhanced or super-enhanced cosmic-ray ionisation rate is required. Finally, the lack of observations of H_2S_2 does not allow us to conclude that this species forms inefficiently in the solid state: it is a symmetric molecule and its predicted abundances are below common detection thresholds. However, S is predicted to be abundant in our models, but may remain as a residue on the grain surface (as observed in the experiments by Garozzo et al. 2010), and thus not be detectable.

7.3 Conclusions

Summarising, we extended the UCL_CHEM chemical model to include new experimental and theoretical results on sulfur chemistry; in particular, we inserted laboratory data from H_2S-ice processed by protons which simulate cosmic-ray impacts on the grain surface. Garozzo et al. (2010) detected in their icy mantle analogues the formation of CS_2, which has not been detected in the gas phase yet. Based on this evidence, Ward et al.

(2012) studied the production of solid OCS from CS_2 and O ice. We therefore updated the latter reaction in our code. Finally, we considered the formation of OCS on grains via alternative paths as theoretically investigated by Adriaens et al. (2010). We look at the influence of the new reaction network on the fractional abundances of selected S-bearing species by comparing these results on the sulfur chemistry with the original version of our code. A comparison with the observations was also carried out.

We find it difficult to reconcile observations with theoretical estimates, in particular we over-produce H_2S by three orders of magnitude and OCS by two orders of magnitude.

The present study is still in progress. We wish to further refine our theoretical results with the aim of reproducing the observed abundances for the entire set of S-bearing species. In an attempt to introduce a more complete sulfur chemistry, we plan to add new experimental results from recent and unpublished TPD experiments. We also intend to test the reliability of the assumptions made concerning the thermal desorption of species occurring during the ice sublimation. Moreover, we would like to speculate more about the existence of a sulfur reservoir in the icy mantles and look at the influence of this residue on the role of sulfur as evolutionary tracer.

Chapter 8

Concluding remarks and future work

In this thesis we explored the fascinating world of interstellar molecules. Each chapter represents a contribution to understanding the chemical interactions occurring at the early stages of star formation. The thread which runs through this thesis is an updating of the UCL_CHEM gas-grain chemical model (described in Chapter 2) with the most recent experimental results involving reactions of interstellar medium relevance, that occur in the gas phase as well as in a solid state. A summary of these updates is reported in the Tables 8.1 and 8.2.

As mentioned in the Introduction to this thesis (Chapter 1), the weakest point of this approach lies in the numerous assumptions made in the treatment of the laboratory data for their conversion to ISM conditions. Experiments are constrained in time and, in general, the sources of radiation employed in order to process the sample are more energetic compared to those existing in ISM environments, where the fluxes are further attenuated by the presence of dust. Moreover, most of the experiments do not employ water ice, while it is well known that water is the main interstellar ice component. We have therefore to speculate whether the chemical interactions occurring on the grain surface are the same regardless of the mixture used as a sample.

The following summary contains the key conclusions that I have drawn at the end of each study.

1. In Chapter 3, we investigated a possible solid phase route of formation for methyl formate ($HCOOCH_3$). We used a chemical model updated with recent results from

Table 8.1. Rate constants derived from experimental branching ratios for the competing channels of the reactions between atomic oxygen and small unsaturated hydrocarbons.

Reaction	k(200K)[$cm^3 mol^{-1}\ s^{-1}$]
$O + C_2H_2 \rightarrow HCCO + H$	9.9×10^{-15}
$O + C_2H_2 \rightarrow CH_2 + CO$	2.6×10^{-15}
$O + C_2H_2 \rightarrow C_2H + OH$	0
$O + C_2H_4 \rightarrow CH_3 + HCO$	1.0×10^{-13}
$O + C_2H_4 \rightarrow CH_2CHO + H$	9.0×10^{-14}
$O + C_2H_4 \rightarrow H_2CO + CH_2$	6.0×10^{-14}
$O + C_2H_4 \rightarrow CH_2CO + H_2$	3.9×10^{-14}
$O + C_2H_4 \rightarrow CH_3CO + H$	9.0×10^{-15}
$O + C_2H_4 \rightarrow C_2H_3 + OH$	0
$O + CH_3CCH \rightarrow C_2H_4 + CO$	5.2×10^{-13}
$O + CH_3CCH \rightarrow C_2H_3 + HCO$	7.7×10^{-14}
$O + CH_3CCH \rightarrow C_2H_2 + H_2CO$	7.7×10^{-14}
$O + CH_3CCH \rightarrow CH_3CCO + H$	4.3×10^{-14}
$O + CH_3CCH \rightarrow CH_3 + HCCO$	3.1×10^{-15}
$O + CH_2CCH_2 \rightarrow C_2H_4 + CO$	9.8×10^{-13}
$O + CH_2CCH_2 \rightarrow C_2H_2 + H_2CO$	1.1×10^{-13}
$O + CH_2CCH_2 \rightarrow C_2H_3 + HCO$	8.4×10^{-14}
$O + CH_2CCH_2 \rightarrow CH_2CCHO + H$	1.9×10^{-14}
$O + CH_2CCH_2 \rightarrow CH_2CO + CH_2$	3.6×10^{-15}

Table 8.2. Experimental and theoretical rate parameters of astronomical relevance for the formation of selected species on grain surfaces.

	Reaction			α	β	γ
mCH_3OH	$+ mCO$	$\rightarrow mHCOOCH_3$		6.2×10^{-18} [s^{-1}]	0	0
mO	$+ mC_2H_4$	$\rightarrow mc\text{-}C_2H_4O$		6.0×10^{-15} [$cm^3\ s^{-1}$]	0	0
mO	$+ mC_3H_6$	$\rightarrow mc\text{-}C_3H_6O$		5.0×10^{-14} [$cm^3\ s^{-1}$]	0	0
mH_2S	+ CR	→ mSres		2.2×10^{-16} [s^{-1}]	0	0
mH_2S	+ mCO	→ mOCS		3.8×10^{-17} [s^{-1}]	0	0
mH_2S	$+ mH_2S$	$\rightarrow mH_2S_2$		1.9×10^{-16} [s^{-1}]	0	0
$2mH_2S$	+ mCO	$\rightarrow mCS_2$	+ mO	4.9×10^{-17} [s^{-1}]	0	0
mH_2S	+ 2mO	$\rightarrow mSO_2$		1.2×10^{-16} [s^{-1}]	0	0
mCO	+ mS	→ mOCS		1.7×10^{-11} [s^{-1}]	0	1893 [K]
mCO	+ mHS	→ mOCS	+ mH	1.7×10^{-11} [s^{-1}]	0	831 [K]
mCS_2	+ mO	→ mOCS	+ mS	6.4×10^{-23} [$cm^3\ s^{-1}$]	0	0

an experiment where grain surfaces analogues were irradiated, with 200 keV protons at 16 K, to simulate the effects of cosmic-ray irradiation on interstellar grain surfaces. By modelling four different (in terms of physical parameters) astronomical environments, we found that, after the updates, our model may be sufficient to reproduce the observed methyl formate abundances in cold cores, but not those in hot cores and corinos, where we need to invoke alternative mechanisms of methyl formate production that are efficient at higher temperatures.

2. In Chapter 4, we tested whether ethylene oxide (c-C_2H_4O) can be formed during the cold phase (when the ISM dense cores are formed), via addition of an oxygen atom across the C=C double bond of the ethylene molecule, and released by thermal desorption during the hot core phase. A simplistic comparison between our theoretical results and those from the observations showed that we are able to reproduce the abundances of ethylene oxide towards high-mass star-forming regions.

3. Chapter 5 represents an extention of Chapter 4, but with the aim of understanding the chemistry for the formation and loss of ethylene oxide in hot and cold interstellar objects by employing an alternative gas-grain network, MONACO, and by comparison with the chemical behaviour of its isomer, acetaldehyde. We tested the code for the case of a hot core. The model allowed us to predict the gaseous and solid state ethylene oxide abundances during a cooling-down phase prior to star formation and during the subsequent warm-up phase. We therefore predicted at what temperatures ethylene oxide forms on grain surfaces (10–20 K) and at what temperature (45–65 K) it starts to desorb into the gas. In particular, we found that ethylene oxide desorbs at lower temperatures than what we had assumed in Chapter 4. The observed low rotational temperature of ethylene oxide in star-forming regions confirmed the hypothesis that the excitation of this species can be significantly sub-thermal. Moreover, despite their different chemical structures, ethylene oxide and acetaldehyde are predicted to react via similar chemistries in the gas phase. The similarities highlighted in the present study suggest that acetaldehyde may be used as a tracer for ethylene oxide towards cold cores.

4. In Chapter 6, we presented an upgraded chemical model including a revision of the reactions between oxygen atoms and small unsaturated hydrocarbons for different astrochemical environments. The first conclusion is that towards hot cores/corinos

atomic oxygen easily degrades unsaturated hydrocarbons directly to CO or to its precursor species (such as HCCO or HCO) and destroys the double or triple bond of alkenes and alkynes. Therefore, environments rich in atomic oxygen at a relatively high temperature are not expected to be rich in large unsaturated hydrocarbons or polycyclic aromatic hydrocarbons. In contrast, in O-poor and C-rich objects, hydrocarbon growth can occur to a large extent. In addition, new radical species, namely ketyl and vinoxy radicals, generated from other reaction channels, can influence the abundances of hydrocarbons in hot cores. We, therefore, suggest that they should be included in the available databases. Hydrocarbon column densities are calculated in the 10^{13}–10^{15} cm^{-2} range, in good agreement with their observed values, despite the small number of data currently published in the literature.

5. In Chapter 7, we aimed to shed light on what form sulphur takes on the icy mantles. For this purpose we investigated the sensitivity of the code to changes in different physical parameters, as well as in the freeze-out pathways of selected sulphur-bearing species. Due to the high reactivity of sulphur and the several forms in which it has been detected, this work is still in progress in the attempt to further expand the sulphur reaction network by including new experimental results that are currently being collected by the group of Prof. Wendy Brown at the University of Sussex (UK).

It would be ideal, as the next step, to answer the several open questions regarding the discrepancies between laboratory and interstellar medium conditions. For instance, in the laboratory, fluxes are of the order of 10^{11} species/cm^2 s^{-1}, against the 10^5 species/cm^2 s^{-1}, estimated on a single grain under typical interstellar cloud conditions (see review by Tielens & Hagen 2013). Moreover, only the 20% of the reactions included in databases have been experimentally studied; therefore, chemical models contain several uncertainties in reaction routes and their relevant rates.

In order to make progress in the area of chemical modelling, I wish to implement more sophisticated codes based on laboratory data, that account, for example, for the details of the surface (such as geometry, composition) and contain a more accurate treatment of the cosmic-rays impinging onto the grain surface, in order to consider not only for the impact of protons (as in Chapter 3 and 7) but also for the effects (if any) due to the electrons while crossing the icy mantles.

The successful results obtained so far in the attempt to reproduce the molecular abundances of some COMs in star-forming regions encourage us to pursue my future work in this direction such as, for example, an investigation of the chemistry of more complex organic molecules of biological interest (e.g. ribose). My new goals are to identify key chemical species, understand their mechanisms of distruction and formation and, in doing so, contribute to shedding light on the origin and evolution of the Universe in regions of star formation.

Bibliography

Abbas, M. M., Tankosic, D., Craven, P. D., Spann, J. F., LeClair, A., West, E. A., Weingartner, J. C., Tielens, A. G. G. M., Nuth, J. A., Camata, R. P. & Gerakines, P. A., 2006, ApJ, **645**, 324

Adriaens, D. A., Goumans, T. P. M., Catlow, C. R. A. & Brown, W. A., 2010, *The Journal of Physical Chemistry C*, **114**(4), 1892

Agúndez, M. & Cernicharo, J., 2006, ApJ, **650**, 374

Aikawa, Y., Wakelam, V., Hersant, F., Garrod, R. T. & Herbst, E., 2012, ApJ, **760**, 40

Allamandola, L. J., Sandford, S. A. & Valero, G. J., 1988, Icarus, **76**, 225

Allamandola, L. J., Tielens, A. G. G. M. & Barker, J. R., 1989, ApJS, **71**, 733

Allen, M. & Robinson, G. W., 1977, ApJ, **212**, 396

Amiaud, L., Fillion, J. H., Dulieu, F., Momeni, A. & Lemaire, J. L., 2007, in *Molecules in Space and Laboratory*

Awad, Z., Chigai, T., Kimura, Y., Shalabiea, O. M. & Yamamoto, T., 2005, ApJ, **626**, 262

Awad, Z., Viti, S., Collings, M. P. & Williams, D. A., 2010, MNRAS, **407**, 2511

Bacmann, A., Taquet, V., Faure, A., Kahane, C. & Ceccarelli, C., 2012, A&A, **541**, L12

Balucani, N., Capozza, G., Leonori, F., Segoloni, E. & Casavecchia, P., 2006, *International Reviews in Physical Chemistry*, **25**(1-2), 109

Baouche, S., Hornekær, L., Petrunin, V. V., Luntz, A. C., Zecho, T. & Baurichter, A., 2005, in *IAU Symposium*, volume 235 of *IAU Symposium*, p. 123P

Baratta, G. A., Domingo, M., Ferini, G., Leto, G., Palumbo, M. E., Satorre, M. A. & Strazzulla, G., 2003, *Nuclear Instruments and Methods in Physics Research B*, **209**, 283

Barzel, B. & Biham, O., 2007, ApJ, **658**, L37

Baulch, D. L., Bowman, C. T., Cobos, C. J., Cox, R. A., Just, T., Kerr, J. A., Pilling, M. J., D.Stocker, Troe, J., Tsang, W., Walker, R. W. & Warnatz, J., 2005, *Journal of Physical and Chemical Reference Data*, **34**, 757

Beltrán, M. T., Codella, C., Viti, S., Neri, R. & Cesaroni, R., 2009, ApJ, **690**, L93

Bennett, C. J., Jamieson, C. S., Osamura, Y. & Kaiser, R. I., 2006, ApJ, **653**, 792

Bennett, C. J. & Kaiser, R. I., 2007, ApJ, **661**, 899

Bennett, C. J., Osamura, Y., Lebar, M. D. & Kaiser, R. I., 2005, ApJ, **634**, 698

Bergin, E. A. & Langer, W. D., 1997, ApJ, **486**, 316

Bernasconi, P. A. & Maeder, A., 1996, A&A, **307**, 829

Bernstein, L. S. & Lynch, D. K., 2009, ApJ, **704**, 226

Betz, A. L., 1981, ApJ, **244**, L103

Bless, R. C. & Savage, B. D., 1972, ApJ, **171**, 293

Boissier, J., Bockelée-Morvan, D., Biver, N., Crovisier, J., Despois, D., Marsden, B. G. & Moreno, R., 2007, A&A, **475**, 1131

Boland, W. & de Jong, T., 1982, ApJ, **261**, 110

Bottinelli, S., Ceccarelli, C., Williams, J. P. & Lefloch, B., 2007, A&A, **463**, 601

Bringa, E. M. & Johnson, R. E., 2004, ApJ, **603**, 159

Brown, P. D., Charnley, S. B. & Millar, T. J., 1988, MNRAS, **231**, 409

Brown, R. D., Crofts, J. G., Godfrey, P. D., Gardner, F. F., Robinson, B. J. & Whiteoak, J. B., 1975, ApJ, **197**, L29

Burke, D. J. & Brown, W. A., 2010, *Phys. Chem. Chem. Phys.*, **12**, 5947

Cami, J., Bernard-Salas, J., Peeters, E. & Malek, S. E., 2010, *Science*, **329**, 1180

Capozza, G., Segoloni, E., Leonori, F., Volpi, G. G. & Casavecchia, P., 2004, *The Journal of Chemical Physics*, **120**(10), 4557

Casavecchia, P., Leonori, F., Balucani, N., Petrucci, R., Capozza, G. & Segoloni, E., 2009, *Phys. Chem. Chem. Phys.*, **11**, 46

Caselli, P., Hasegawa, T. I. & Herbst, E., 1993, ApJ, **408**, 548

Caselli, P., Hasegawa, T. I. & Herbst, E., 1998, ApJ, **495**, 309

Caux, E., Ceccarelli, C., Castets, A., Vastel, C., Liseau, R., Molinari, S., Nisini, B., Saraceno, P. & White, G. J., 1999, A&A, **347**, L1

Cazaux, S., Tielens, A. G. G. M., Ceccarelli, C., Castets, A., Wakelam, V., Caux, E., Parise, B. & Teyssier, D., 2003, ApJ, **593**, L51

Cernicharo, J., Kahane, C., Guelin, M. & Hein, H., 1987, A&A, **181**, L9

Cernicharo, J., Marcelino, N., Roueff, E., Gerin, M., Jiménez-Escobar, A. & Muñoz Caro, G. M., 2012, ApJ, **759**, L43

Cesaroni, R., Olmi, L., Walmsley, C. M., Churchwell, E. & Hofner, P., 1994, ApJ, **435**, L137

Chang, Q., Cuppen, H. M. & Herbst, E., 2007, A&A, **469**, 973

Charnley, S. B., 1995, Ap&SS, **224**, 251

Charnley, S. B., 1997, ApJ, **481**, 396

Charnley, S. B., 2004, *Advances in Space Research*, **33**, 23

Charnley, S. B., Tielens, A. G. G. M. & Millar, T. J., 1992, ApJ, **399**, L71

Churchwell, E., Walmsley, C. M. & Cesaroni, R., 1990, A&AS, **83**, 119

Codella, C., Lorenzani, A., Gallego, A. T., Cesaroni, R. & Moscadelli, L., 2004, A&A, **417**, 615

Codella, C., Viti, S., Williams, D. A. & Bachiller, R., 2006, ApJ, **644**, L41

Cole, C. A., Wehres, N., Yang, Z., Thomsen, D. L., Snow, T. P. & Bierbaum, V. M., 2012, ApJ, **754**, L5

Collings, M. P., Anderson, M. A., Chen, R., Dever, J. W., Viti, S., Williams, D. A. & McCoustra, M. R. S., 2004, MNRAS, **354**, 1133

Collings, M. P., Dever, J. W., Fraser, H. J. & McCoustra, M. R. S., 2003, Ap&SS, **285**, 633

Collings, M. P. & McCoustra, M. R. S., 2005, in D. C. Lis, G. A. Blake & E. Herbst (eds.), *Astrochemistry: Recent Successes and Current Challenges*, volume 231 of *IAU Symposium*, pp. 405–414

Combes, F., Gerin, M., Wootten, A., Wlodarczak, G., Clausset, F. & Encrenaz, P. J., 1987, A&A, **180**, L13

Cordiner, M. A. & Charnley, S. B., 2012, ApJ, **749**, 120

Cordiner, M. A., Charnley, S. B., Buckle, J. V., Walsh, C. & Millar, T. J., 2011, ApJ, **730**, L18

Cox, N. L. J. & Spaans, M., 2006, A&A, **451**, 973

Creighan, S. C., Perry, J. S. A. & Price, S. D., 2006, *The Journal of Chemical Physics*, **124**(11), 114701

Cuppen, H. M., van Dishoeck, E. F., Herbst, E. & Tielens, A. G. G. M., 2009, A&A, **508**, 275

Cvetanovic, R. J., 1987, *Journal of Physical and Chemical Reference Data*, **16**, 261

Dartois, E., Schutte, W., Geballe, T. R., Demyk, K., Ehrenfreund, P. & D'Hendecourt, L., 1999, A&A, **342**, L32

Dickens, J. E., Irvine, W. M., Ohishi, M., Ikeda, M., Ishikawa, S., Nummelin, A. & Hjalmarson, A., 1997, ApJ, **489**, 753

Dickens, J. E., Langer, W. D. & Velusamy, T., 2000, in *American Astronomical Society Meeting Abstracts*, volume 32 of *Bulletin of the American Astronomical Society*, p. 1415

Draine, B. T., 2003, ARA&A, **41**, 241

Duley, W. W. & Williams, D. A., 1984, *Interstellar chemistry*

Duley, W. W. & Williams, D. A., 1993, MNRAS, **260**, 37

Dulieu, F., Amiaud, L., Congiu, E., Fillion, J.-H., Matar, E., Momeni, A., Pirronello, V. & Lemaire, J. L., 2010, A&A, **512**, A30

Dulieu, F., Amiaud, L., Fillion, J.-H. ., Matar, E., Momeni, A., Pirronello, V. & Lemaire, J. L., 2007, in *Molecules in Space and Laboratory*

Eddington, A. S., 1937, *The Observatory*, **60**, 99

Ehrenfreund, P. & Charnley, S. B., 2000, ARA&A, **38**, 427

Ehrenfreund, P., Charnley, S. B. & Wooden, D., 2004, *From interstellar material to comet particles and molecules*, pp. 115–133

Ehrenfreund, P. & Cleaves, H. J., 2003, in M. Fridlund, T. Henning & H. Lacoste (eds.), *Earths: DARWIN/TPF and the Search for Extrasolar Terrestrial Planets*, volume 539 of *ESA Special Publication*, pp. 195–203

Fayolle, E. C., Bertin, M., Romanzin, C., Michaut, X., Öberg, K. I., Linnartz, H. & Fillion, J.-H., 2011, ApJ, **739**, L36

Ferrante, R. F., Moore, M. H., Spiliotis, M. M. & Hudson, R. L., 2008, ApJ, **684**, 1210

Fortney, J. J., 2012, ApJ, **747**, L27

Frerking, M. A., Linke, R. A. & Thaddeus, P., 1979, ApJ, **234**, L143

Fu, B., Han, Y.-C., Bowman, J. M., Angelucci, L., Balucani, N., Leonori, F. & Casavecchia, P., 2012a, *Proceedings of the National Academy of Science*, **109**, 9733

Fu, B., Han, Y.-C., Bowman, J. M., Leonori, F., Balucani, N., Angelucci, L., Occhiogrosso, A., Petrucci, R. & Casavecchia, P., 2012b, *The Journal of Chemical Physics*, **137**, 22A532

Fuchs, G. W., Cuppen, H. M., Ioppolo, S., Romanzin, C., Bisschop, S. E., Andersson, S., van Dishoeck, E. F. & Linnartz, H., 2009, A&A, **505**, 629

Gálvez, O., Ortega, I. K., Maté, B., Moreno, M. A., Martín-Llorente, B., Herrero, V. J., Escribano, R. & Gutiérrez, P. J., 2007, A&A, **472**, 691

García-Hernández, D. A., Iglesias-Groth, S., Acosta-Pulido, J. A., Manchado, A., García-Lario, P., Stanghellini, L., Villaver, E., Shaw, R. A. & Cataldo, F., 2011, ApJ, **737**, L30

Garozzo, M., Fulvio, D., Kanuchova, Z., Palumbo, M. E. & Strazzulla, G., 2010, A&A, **509**, A67

Garozzo, M., La Rosa, L., Kanuchova, Z., Ioppolo, S., Baratta, G. A., Palumbo, M. E. & Strazzulla, G., 2011, A&A, **528**, A118

Garrod, R. T., 2008b, A&A, **491**, 239

Garrod, R. T. & Herbst, E., 2006a, A&A, **457**, 927

Garrod, R. T., Wakelam, V. & Herbst, E., 2007, A&A, **467**, 1103

Garrod, R. T., Weaver, S. L. W. & Herbst, E., 2008a, ApJ, **682**, 283

Garrod, R. T., Williams, D. A. & Rawlings, J. M. C., 2006b, MNRAS, **373**, 577

Gerakines, P. A., Moore, M. H. & Hudson, R. L., 2000, A&A, **357**, 793

Gerakines, P. A., Schutte, W. A. & Ehrenfreund, P., 1996, A&A, **312**, 289

Gibb, E. L., Whittet, D. C. B., Boogert, A. C. A. & Tielens, A. G. G. M., 2004, ApJS, **151**, 35

Gibb, E. L., Whittet, D. C. B., Schutte, W. A., Boogert, A. C. A., Chiar, J. E., Ehrenfreund, P., Gerakines, P. A., Keane, J. V., Tielens, A. G. G. M., van Dishoeck, E. F. & Kerkhof, O., 2000, ApJ, **536**, 347

Gillett, F. C. & Forrest, W. J., 1973, ApJ, **179**, 483

Gosavi, R. K., Safarik, I. & Strausz, O. P., 1985, *Canadian Journal of Chemistry*, **63**(7), 1689

Gottlieb, C. A. & Ball, J. A., 1973, ApJ, **184**, L59

Gottlieb, C. A., Ball, J. A., Gottlieb, E. W., Lada, C. J. & Penfield, H., 1975, ApJ, **200**, L147

Guélin, M., Brouillet, N., Cernicharo, J., Combes, F. & Wootten, A., 2008, Ap&SS, **313**, 45

Gupta, H. D., 2009, *Negative molecular ions in the laboratory and in space*, Ph.D. thesis, PhD Thesis, 2009

Halfen, D. T., Ziurys, L. M., Brünken, S., Gottlieb, C. A., McCarthy, M. C. & Thaddeus, P., 2009, ApJ, **702**, L124

Hasegawa, T. I. & Herbst, E., 1993, MNRAS, **263**, 589

Hasegawa, T. I., Herbst, E. & Leung, C. M., 1992, ApJS, **82**, 167

Hassel, G. E., Herbst, E. & Garrod, R. T., 2008, ApJ, **681**, 1385

Hatchell, J., Thompson, M. A., Millar, T. J. & MacDonald, G. H., 1998, A&A, **338**, 713

Hatchell, J. & Viti, S., 2002, A&A, **381**, L33

Herbst, E., 1985, ApJ, **291**, 226

Herbst, E., 1995, *Annual Review of Physical Chemistry*, **46**(1), 27

Herbst, E., 2005, in A. Wilson (ed.), *ESA Special Publication*, volume 577 of *ESA Special Publication*, pp. 205–210

Herbst, E. & Klemperer, W., 1973, ApJ, **185**, 505

Herbst, E. & Leung, C. M., 1986, ApJ, **310**, 378

Herbst, E. & Leung, C. M., 1989, ApJS, **69**, 271

Herbst, E. & Millar, T. J., 2008, *The Chemistry of Cold Interstellar Cores* (Imperial College Press), pp. 1–54

Herbst, E. & van Dishoeck, E. F., 2009, ARA&A, **47**, 427

Herpin, F., Marseille, M., Wakelam, V., Bontemps, S. & Lis, D. C., 2009, A&A, **504**, 853

Hirano, N., Kamazaki, T., Mikami, H., Ohashi, N. & Umemoto, T., 1999, *Discovery of two extreme young protostars in Barnard 1.*

Hiraoka, K., Takayama, T., Euchi, A., Handa, H. & Sato, T., 2000, ApJ, **532**, 1029

Hollenbach, D. J. & Salpeter, E. E., 1970, *J. Chem. Phys.*, **53**, 79

Hollenbach, D. J. & Tielens, A. G. G. M., 1997, ARA&A, **35**, 179

Hollis, J. M. & Churchwell, E., 2001, ApJ, **551**, 803

Hollis, J. M., Jewell, P. R., Lovas, F. J., Remijan, A. & Møllendal, H., 2004, ApJ, **610**, L21

Horn, A., Møllendal, H., Sekiguchi, O., Uggerud, E., Roberts, H., Herbst, E., Viggiano, A. A. & Fridgen, T. D., 2004, ApJ, **611**, 605

Hornekær, L., Baurichter, A., Petrunin, V. V., Field, D. & Luntz, A. C., 2003, *Science*, **302**, 1943

Huang, L. C. L., Asvany, O., Chang, A. H. H., Balucani, N., Lin, S. H., Lee, Y. T., Kaiser, R. I. & Osamura, Y., 2000, J. Chem. Phys., **113**, 8656

Hudson, R. L. & Moore, M. H., 1999, Icarus, **140**, 451

Hudson, R. L. & Moore, M. H., 2003, ApJ, **586**, L107

Ikeda, M., Ohishi, M., Nummelin, A., Dickens, J. E., Bergman, P., Hjalmarson, Å. & Irvine, W. M., 2001, ApJ, **560**, 792

Ioppolo, S., 2010, *Surface formation routes of interstellar molecules*, Ph.D. thesis, University of Leiden

Ioppolo, S., Palumbo, M. E., Baratta, G. A. & Mennella, V., 2009, A&A, **493**, 1017

Irvine, W. M., Goldsmith, P. F. & Hjalmarson, A., 1987, in D. J. Hollenbach & H. A. Thronson, Jr. (eds.), *Interstellar Processes*, volume 134 of *Astrophysics and Space Science Library*, pp. 561–609

Islam, F., Latimer, E. R. & Price, S. D., 2007, J. Chem. Phys., **127**(6), 064701

Jefferts, K. B., Penzias, A. A., Wilson, R. W. & Solomon, P. M., 1971, ApJ, **168**, L111

Jenkins, E. B., 2009, ApJ, **700**, 1299

Jenniskens, P. & Blake, D. F., 1994, *Science*, **265**, 753

Jensen, A. G., Rachford, B. L. & Snow, T. P., 2005, ApJ, **619**, 891

Jiménez-Escobar, A. & Muñoz Caro, G. M., 2011, A&A, **536**, A91

Kaifu, N., Suzuki, H., Ohishi, M., Miyaji, T., Ishikawa, S.-I., Kasuga, T., Morimoto, M. & Saito, S., 1987, ApJ, **317**, L111

Kaiser, R., 2003, *Chemical Physics Letters*, **382**, 112

Kaiser, R. I., 2002, *Chemical Reviews*, **102**(5), 1309

Kaiser, R. I. & Roessler, K., 1998, ApJ, **503**, 959

Katz, N., Furman, I., Biham, O., Pirronello, V. & Vidali, G., 1999, ApJ, **522**, 305

Kim, Y. S. & Kaiser, R. I., 2012, ApJ, **758**, 37

Kimura, Y., Saito, M., Sakon, I. & Kaito, C., 2007, in *Lunar and Planetary Institute Science Conference Abstracts*, volume 38 of *Lunar and Planetary Institute Science Conference Abstracts*, p. 1511

Klinger, J., 1983, *The Journal of Physical Chemistry*, **87**(21), 4209

Kouchi, A., Yamamoto, T., Kozasa, T., Kuroda, T. & Greenberg, J. M., 1994, A&A, **290**, 1009

Krasnopolsky, V. A., 2008, Icarus, **197**, 377

Kuiper, T. B. H., Kakar, R. K., Rodriguez Kuiper, E. N. & Zuckerman, B., 1975, ApJ, **200**, L151

Laas, J. C., Garrod, R. T., Herbst, E. & Widicus Weaver, S. L., 2011, ApJ, **728**, 71

Latimer, E. R., Islam, F. & Price, S. D., 2008, *Chemical Physics Letters*, **455**(4-6), 174

Leitch-Devlin, M. A. & Williams, D. A., 1985, MNRAS, **213**, 295

Leonori, F., Hickson, K. M., Le Picard, S. D., Wang, X., Petrucci, R., Foggi, P., Balucani, N. & Casavecchia, P., 2010, *Molecular Physics*, **108**, 1097

Leonori, F., Occhiogrosso, A., Balucani, N., Bucci, A., Petrucci, R. & Casavecchia, P., 2012, *The Journal of Physical Chemistry Letters*, **3**(1), 75

Leonori, F., Petrucci, R., Hickson, K. M., Segoloni, E., Balucani, N., Le Picard, S. D., Foggi, P. & Casavecchia, P., 2008, Planet. Space Sci., **56**, 1658

Leonori, F., Skouteris, D., Petrucci, R., Casavecchia, P., Rosi, M. & Balucani, N., 2013, *The Journal of Chemical Physics*, **138**(2), 024311

Lerate, M. R., Yates, J., Viti, S., Barlow, M. J., Swinyard, B. M., White, G. J., Cernicharo, J. & Goicoechea, J. R., 2008, MNRAS, **387**, 1660

Linke, R. A., Frerking, M. A. & Thaddeus, P., 1979, ApJ, **234**, L139

Liszt, H., 2009, in *American Astronomical Society Meeting Abstracts 214*, volume 214 of *American Astronomical Society Meeting Abstracts*, p. 221.03

Loison, J.-C., Halvick, P., Bergeat, A., Hickson, K. M. & Wakelam, V., 2012, MNRAS, **421**, 1476

Maret, S., Ceccarelli, C., Caux, E., Tielens, A. G. G. M., Jørgensen, J. K., van Dishoeck, E., Bacmann, A., Castets, A., Lefloch, B., Loinard, L., Parise, B. & Schöier, F. L., 2004, A&A, **416**, 577

Mathis, J. S., 1990, ARA&A, **28**, 37

Mattera, L., Salvo, C., Terreni, S. & Tommasini, F., 1980, *Surface Science*, **97**(1), 158

Mautner, M. N., Abdelsayed, V., El-Shall, M. S., Thrower, J. D., Green, S. D., Collings, M. P. & McCoustra, M. R. S., 2006, *Faraday Discussions*, **133**, 103

McElroy, D., Walsh, C., Markwick, A. J., Cordiner, M. A., Smith, K. & Millar, T. J., 2013, A&A, **550**, A36

Mennella, V., Baratta, G. A., Esposito, A., Ferini, G. & Pendleton, Y. J., 2003, ApJ, **587**, 727

Menten, K. M., Wyrowski, F., Belloche, A., Güsten, R., Dedes, L. & Müller, H. S. P., 2011, A&A, **525**, A77

Meyer, D. M., 1997, in E. F. van Dishoeck (ed.), *IAU Symposium*, volume 178 of *IAU Symposium*, pp. 407–419

Millar, T. J., Bennett, A., Rawlings, J. M. C., Brown, P. D. & Charnley, S. B., 1991, A&AS, **87**, 585

Millar, T. J., Farquhar, P. R. A. & Willacy, K., 1997, A&AS, **121**, 139

Millar, T. J., Farquhar, P. R. A. & Willacy, K., 2000a, *VizieR Online Data Catalog*, **412**, 10139

Millar, T. J., Herbst, E. & Bettens, R. P. A., 2000b, MNRAS, **316**, 195

Millar, T. J., Leung, C. M. & Herbst, E., 1987, A&A, **183**, 109

Millar, T. J. & Nejad, L. A. M., 1985, MNRAS, **217**, 507

Millar, T. J., Walsh, C., Cordiner, M. A., Ní Chuimín, R. & Herbst, E., 2007, ApJ, **662**, L87

Millar, T. J. & Williams, D. A., 1993, *Dust and chemistry in astronomy*

Miller, J. S. & Singer, R. B., 1993, in *Lunar and Planetary Institute Science Conference Abstracts*, volume 24 of *Lunar and Planetary Institute Science Conference Abstracts*, pp. 989–990

Minh, Y. C., Irvine, W. M., McGonagle, D. & Ziurys, L. M., 1990, ApJ, **360**, 136

Miyauchi, N., Hidaka, H., Chigai, T., Nagaoka, A., Watanabe, N. & Kouchi, A., 2008, *Chemical Physics Letters*, **456**, 27

Modica, P. & Palumbo, M. E., 2010, A&A, **519**, A22

Molinari, S., Brand, J., Cesaroni, R. & Palla, F., 2000, A&A, **355**, 617

Molinari, S., Testi, L., Rodríguez, L. F. & Zhang, Q., 2002, ApJ, **570**, 758

Moore, M. H., Hudson, R. L. & Carlson, R. W., 2007, Icarus, **189**, 409

Morris, M., Gilmore, W., Palmer, P., Turner, B. E. & Zuckerman, B., 1975, ApJ, **199**, L47

Neufeld, D. A., Falgarone, E., Gerin, M., Godard, B., Herbst, E., Pineau des Forêts, G., Vasyunin, A. I., Güsten, R., Wiesemeyer, H. & Ricken, O., 2012, A&A, **542**, L6

Nummelin, A., Bergman, P., Hjalmarson, A., Friberg, P., Irvine, W. M., Millar, T. J., Ohishi, M. & Saito, S., 1999, *VizieR Online Data Catalog*, **211**, 70427

Nummelin, A., Dickens, J. E., Bergman, P., Hjalmarson, A., Irvine, W. M., Ikeda, M. & Ohishi, M., 1998, A&A, **337**, 275

Öberg, K. I., Bottinelli, S., Jørgensen, J. K. & van Dishoeck, E. F., 2010, ApJ, **716**, 825

Öberg, K. I., Fuchs, G. W., Awad, Z., Fraser, H. J., Schlemmer, S., van Dishoeck, E. F. & Linnartz, H., 2007, ApJ, **662**, L23

Öberg, K. I., Garrod, R. T., van Dishoeck, E. F. & Linnartz, H., 2009, A&A, **504**, 891

Öberg, K. I., Garrod, R. T., van Dishoeck, E. F. & Linnartz, H., 2011, in *2010 NASA Laboratory Astrophysics Workshop*, p. C44

Occhiogrosso, A., 2010, *Studio sperimentale della dinamica di reazione di atomi di ossigeno con etilene*, Master's thesis, University of Perugia

Occhiogrosso, A., Viti, S. & Balucani, N., 2013, MNRAS, **432**, 3423

Occhiogrosso, A., Viti, S., Modica, P. & Palumbo, M. E., 2011, MNRAS, **418**, 1923

Occhiogrosso, A., Viti, S., Ward, M. D. & Price, S. D., 2012, MNRAS, **427**, 2450

Ohishi, M. & Kaifu, N., 1998, *Faraday Discussions*, **109**, 205

Palumbo, M. E., Castorina, A. C. & Strazzulla, G., 1999, A&A, **342**, 551

Palumbo, M. E., Ferini, G. & Baratta, G. A., 2004, *Advances in Space Research*, **33**, 49

Palumbo, M. E., Geballe, T. R. & Tielens, A. G. G. M., 1997, ApJ, **479**, 839

Palumbo, M. E., Tielens, A. G. G. M. & Tokunaga, A. T., 1995, ApJ, **449**, 674

Pan, J., Albert, S., Sastry, K. V. L. N., Herbst, E. & De Lucia, F. C., 1998, ApJ, **499**, 517

Pendleton, Y. J., 2004, in A. N. Witt, G. C. Clayton & B. T. Draine (eds.), *Astrophysics of Dust*, volume 309 of *Astronomical Society of the Pacific Conference Series*, p. 573

Penzias, A. A., Solomon, P. M., Wilson, R. W. & Jefferts, K. B., 1971, ApJ, **168**, L53

Pickles, J. B. & Williams, D. A., 1977, Ap&SS, **52**, 443

Piper, J., Morrison, J. & Peters, C., 1984, *Molecular Physics*, **53**(6), 1463

Pirronello, V., 1991, in E. Bussoletti, G. Strazzulla & P. Papali (eds.), *Solid-State Astrophysics*, p. 381

Pirronello, V., Liu, C., Shen, L. & Vidali, G., 1997, ApJ, **475**, L69

Prasad, S. S. & Huntress, Jr., W. T., 1980, ApJS, **43**, 1

Quan, D. & Herbst, E., 2007, A&A, **474**, 521

Rawlings, J. M. C., Hartquist, T. W., Menten, K. M. & Williams, D. A., 1992, MNRAS, **255**, 471

Remijan, A., Snyder, L. E., Friedel, D. N., Liu, S.-Y. & Shah, R. Y., 2003, ApJ, **590**, 314

Ridgway, S. T., Hall, D. N. B., Wojslaw, R. S., Kleinmann, S. G. & Weinberger, D. A., 1976, Nature, **264**, 345

Roberts, H. & Millar, T. J., 2000, A&A, **361**, 388

Roberts, J. F., Rawlings, J. M. C., Viti, S. & Williams, D. A., 2007, MNRAS, **382**, 733

Ruffle, D. P., Hartquist, T. W., Caselli, P. & Williams, D. A., 1999, MNRAS, **306**, 691

Saito, S., Kawaguchi, K., Yamamoto, S., Ohishi, M., Suzuki, H. & Kaifu, N., 1987, ApJ, **317**, L115

Sakai, N., Sakai, T., Osamura, Y. & Yamamoto, S., 2007, ApJ, **667**, L65

Salama, F., 2008, in S. Kwok & S. Sanford (eds.), *IAU Symposium*, volume 251 of *IAU Symposium*, pp. 357–366

Sandford, S. A. & Allamandola, L. J., 1990, Icarus, **87**, 188

Sandford, S. A. & Allamandola, L. J., 1993, ApJ, **417**, 815

Savage, B. D. & Mathis, J. S., 1979, ARA&A, **17**, 73

Scappini, F., Cecchi-Pestellini, C., Smith, H., Klemperer, W. & Dalgarno, A., 2003, MNRAS, **341**, 657

Schöier, F. L., Jørgensen, J. K., van Dishoeck, E. F. & Blake, G. A., 2002, A&A, **390**, 1001

Semenov, D., Hersant, F., Wakelam, V., Dutrey, A., Chapillon, E., Guilloteau, S., Henning, T., Launhardt, R., Piétu, V. & Schreyer, K., 2010, A&A, **522**, A42

Sinclair, M. W., Fourikis, N., Ribes, J. C., Robinson, B. J., Brown, R. D. & Godfrey, P. D., 1973, *Australian Journal of Physics*, **26**, 85

Smith, R. S., Huang, C., Wong, E. K. L. & Kay, B. D., 1997, *Phys. Rev. Lett.*, **79**, 909

Smoluchowski, R., 1978, *Science*, **201**, 809

Smoluchowski, R., 1983, *Science*, **222**, 161

Snyder, L. E., Hollis, J. M., Ulich, B. L., Lovas, F. J., Johnson, D. R. & Buhl, D., 1975, ApJ, **198**, L81

Snyder, L. E., Lovas, F. J., Mehringer, D. M., Miao, N. Y., Kuan, Y.-J., Hollis, J. M. & Jewell, P. R., 2002, ApJ, **578**, 245

Sofia, U. J. & Meyer, D. M., 2001, ApJ, **554**, L221

Stantcheva, T., Shematovich, V. I. & Herbst, E., 2002, A&A, **391**, 1069

Strazzulla, G. & Palumbo, M. E., 1998, Planet. Space Sci., **46**, 1339

Sutton, E. C., Peng, R., Danchi, W. C., Jaminet, P. A., Sandell, G. & Russell, A. P. G., 1995, ApJS, **97**, 455

Tafalla, M., 2005, in D. C. Lis, G. A. Blake & E. Herbst (eds.), *Astrochemistry: Recent Successes and Current Challenges*, volume 231 of *IAU Symposium*, pp. 17–26

Taquet, V., Ceccarelli, C. & Kahane, C., 2012, A&A, **538**, A42

Tarafdar, S. P., Prasad, S. S., Huntress, Jr., W. T., Villere, K. R. & Black, D. C., 1985, ApJ, **289**, 220

Thaddeus, P., Guelin, M. & Linke, R. A., 1981, ApJ, **246**, L41

Thaddeus, P., Kutner, M. L., Penzias, A. A., Wilson, R. W. & Jefferts, K. B., 1972, ApJ, **176**, L73

Thrower, J. D., Burke, D. J., Collings, M. P., Dawes, A., Holtom, P. D., Jamme, F., Kendall, P., Brown, W. A., Clark, I. P., Fraser, H. J., McCoustra, M. R. S., Mason, N. J. & Parker, A. W., 2008, ApJ, **673**, 1233

Thrower, J. D., Collings, M. P., Rutten, F. J. M. & McCoustra, M. R. S., 2009, J. Chem. Phys., **131**(24), 244711

Thrower, J. D., Jørgensen, B., Friis, E. E., Baouche, S., Mennella, V., Luntz, A. C., Andersen, M., Hammer, B. & Hornekær, L., 2012, ApJ, **752**, 3

Tielens, A. G. G. M., 2005, *The Physics and Chemistry of the Interstellar Medium* (Cambridge University Press, UK)

Tielens, A. G. G. M. & Hagen, W., 1982, A&A, **114**, 245

Tielens, A. G. G. M. & Hagen, W., 2013, *Reviews of Modern Physics*, **85**, 1021

Tsuji, T., 1973, A&A, **23**, 411

Turner, B. E. & Apponi, A. J., 2001, ApJ, **561**, L207

Turner, B. E., Chan, K.-W., Green, S. & Lubowich, D. A., 1992, ApJ, **399**, 114

Turner, B. E. & Sears, T. J., 1989, ApJ, **340**, 900

van Dishoeck, E. F., 2000, PASP, **112**, 286

van Dishoeck, E. F. & Helmich, F. P., 1996, A&A, **315**, L177

van Dishoeck, E. F., Helmich, F. P., Schutte, W. A., Ehrenfreund, P., Lahuis, F., Boogert, A. C. A., Tielens, A. G. G. M., de Graauw, T., Gerakines, P. A. & Whittet, D. C. B., 1998, in J. Yun & L. Liseau (eds.), *Star Formation with the Infrared Space Observatory*, volume 132 of *Astronomical Society of the Pacific Conference Series*, p. 54

Vasyunin, A. I. & Herbst, E., 2013, ApJ, **769**, 34

Vasyunin, A. I., Semenov, D. A., Wiebe, D. S. & Henning, T., 2009, ApJ, **691**, 1459

Verstraete, L., 2011, in C. Joblin & A. G. G. M. Tielens (eds.), *EAS Publications Series*, volume 46 of *EAS Publications Series*, pp. 415–426

Vidali, G., Roser, J., Manicó, G., Pirronello, V., Perets, H. B. & Biham, O., 2005, *Journal of Physics Conference Series*, **6**, 36

Viti, S., Caselli, P., Hartquist, T. W. & Williams, D. A., 2001, A&A, **370**, 1017

Viti, S., Collings, M. P., Dever, J. W., McCoustra, M. R. S. & Williams, D. A., 2004, MNRAS, **354**, 1141

Viti, S., Jimenez-Serra, I., Yates, J. A., Codella, C., Vasta, M., Caselli, P., Lefloch, B. & Ceccarelli, C., 2011, ApJ, **740**, L3

Viti, S. & Williams, D. A., 1999, MNRAS, **305**, 755

Wakelam, V., Caselli, P., Ceccarelli, C., Herbst, E. & Castets, A., 2004, A&A, **422**, 159

Wakelam, V. & Herbst, E., 2008, ApJ, **680**, 371

Wakelam, V., Herbst, E., Loison, J.-C., Smith, I. W. M., Chandrasekaran, V., Pavone, B., Adams, N. G., Bacchus-Montabonel, M.-C., Bergeat, A., Béroff, K., Bierbaum, V. M., Chabot, M., Dalgarno, A., van Dishoeck, E. F., Faure, A., Geppert, W. D., Gerlich, D., Galli, D., Hébrard, E., Hersant, F., Hickson, K. M., Honvault, P., Klippenstein, S. J., Le Picard, S., Nyman, G., Pernot, P., Schlemmer, S., Selsis, F., Sims, I. R., Talbi, D., Tennyson, J., Troe, J., Wester, R. & Wiesenfeld, L., 2012, ApJS, **199**, 21

Wakelam, V., Herbst, E. & Selsis, F., 2006, A&A, **451**, 551

Wakelam, V., Hersant, F. & Herpin, F., 2011, A&A, **529**, A112

Wang, Z., 1998, *Chemical Physics Letters*, **291**, 381

Ward, M. D., Hogg, I. A. & Price, S. D., 2012, MNRAS, **425**, 1264

Ward, M. D. & Price, S. D., 2011, ApJ, **741**, 121

Watanabe, N., Mouri, O., Nagaoka, A., Chigai, T., Kouchi, A. & Pirronello, V., 2007, ApJ, **668**, 1001

Watanabe, N., Nagaoka, A., Hidaka, H. & Kouchi, A., 2005, in *Protostars and Planets V*, p. 8244

Weingartner, J. C. & Draine, B. T., 2001, ApJ, **548**, 296

Whittet, D. C. B. & Bowey, J. E., 2003, *The Observatory*, **123**, 320

Williams, D. A., 2005, *Journal of Physics Conference Series*, **6**, 1

Williams, D. A. & Herbst, E., 2002, *Surface Science*, **500**(1)

Williams, D. A. & Taylor, S. D., 1996, QJRAS, **37**, 565

Wilner, D. J., Wright, M. C. H. & Plambeck, R. L., 1994, ApJ, **422**, 642

Woodall, J., Agúndez, M., Markwick-Kemper, A. J. & Millar, T. J., 2007, A&A, **466**, 1197

Wooden, D. H., Charnley, S. B. & Ehrenfreund, P., 2004, *Composition and evolution of interstellar clouds* (Kronk, G. W.), pp. 33–66

Woods, P. M., Walsh, C., Cordiner, M. A. & Kemper, F., 2012, MNRAS, **426**, 2689

Yamamoto, S., Saito, S., Kawaguchi, K., Kaifu, N. & Suzuki, H., 1987, ApJ, **317**, L119

Zhang, F., Maksyutenko, P. & Kaiser, R. I., 2012, *Phys. Chem. Chem. Phys.*, **14**, 529

"E caddi come corpo morto cade."

Dante, Divina Commedia, Inferno, V, 142